X-RAY ABSORPTION SPECTROSCOPY STUDY OF OXIDATION OF IRON NANOPARTICLES IN AIR

A Thesis

Presented to the Faculty of Graduate School

of Cornell University

In Partial Fulfillment of the Requirements for the Degree of

Master of Science

By

Anuj Bhargava

August 2016

ABSTRACT

Iron and iron-oxide nanoparticles (NPs) are one of the most explored materials due to its vast range of applications in fields such as ferro-fluids[1], magnetic imaging resonance[2] and energy storage.[3,4] However, the as synthesized Fe NPs have high affinity for oxygen, and oxidize partially to form a core-shell type structure[5,6], or oxidized completely to form structures with hollow core[7,8] due to coalescence of vacancies. High temperature growth of oxide shell is well understood based on extensive theoretical as well as experimental work.[9] However, less is known about the local structure of the iron oxide shell. The oxide shell is considered to be composed of maghemite ($\gamma-Fe_2O_3$) and magnetite (Fe_3O_4). Both these phases form inverse spinel structure, and because of lack of long-range order, it is difficult to characterize these particles using conventional techniques such as x-ray diffraction (XRD). In this study, we report the synthesis of Fe NPs which are oxidized in air at elevated temperatures. Detailed structural characterization of these particles was carried out using Fe K-edge x-ray absorption spectroscopy (XAS). Our results show that Fe NPs, when exposed to air, oxidize partially to form a thin layer of oxide. As the particles are oxidized at high temperature, the Fe atoms diffuse out from the core, whereas vacancies coalescence to form a hollow core. On further oxidation, no there is no structural change, however, interconversion of different phases takes place. Oxidation study at different temperatures of 200 °C and 250 °C show that although it does not lead to any changes in phase contribution, there is a significant increase in crystallinity of the particles at higher temperatures. This work provides a basis for controlled oxidation of Fe NPs by varying the vacancies at octahedral sites which can be useful for tailoring the electrical and magnetic properties of the particles. We have further showed how XAS can be explored to study the short range order of nanoparticles which complement the other characterization techniques such as XRD and TEM.

BIOGRAPHICAL SKETCH

Anuj Bhargava was born on the 26th of March, 1990 in Kanpur, India. He did his undergraduate work at Indian Institute of Technology Kanpur (IITK), majoring in Materials Science and Engineering and graduated in May 2013. While at IITK, he began his research career in the field of nanomaterials and energy storage devices. After graduation, he worked briefly at Reliance Industries where he took the position of an Inspection engineer, and in 2014 joined Cornell University as a graduate student. Working in the Robinson group, he focused his research on synthesis and characterization of nanomaterials for high performance batteries and authored a publication on supercapacitors. After completing his Masters, he will be continuing in the same research group at Cornell University as a PhD student, where he plans to continue on the path of exploration of novel materials for energy applications.

This work is dedicated to my family for supporting me

all the way and making me who I am

ACKNOWLEDGEMENTS

First and foremost, I would like to acknowledge my adviser Prof. Richard Robinson for giving me the opportunity to work on this project and for making me the researcher I am today. His intelligence, hard work and vision never cease to amaze me, and his optimism and encouragement has always acted as a constant source of motivation for me.

I would also like to acknowledge my thesis committee member, Prof. Jin Suntivich for the helpful discussions and guidance. His lectures on electrochemistry and diffusion have been of great assistance for conducting my research.

Thanks to Andrew Nelson for mentoring me in the lab and for all the help with the synthesis and TEM. Your help in every aspect of my research was imperative to completion of this work. I would also like to acknowledge Don for running the CHESS experiments; Curtis and Doug for help with the diffraction analysis; and Sanjaya for guiding me on the supercapacitors project.

This work made use of the Cornell Center for Materials Research (CCMR) Shared Facilities, which are supported through the NSF MRSEC program (DMR-1120296); and the Cornell High Energy Synchrotron Source (CHESS) facility, supported by the NSF & NIH/NIGMS via NSF award DMR-0936384.

TABLE OF CONTENTS

LIST OF FIGURES

Figure 5.7. Coordination number of paths (a) [α-Fe] Fe11, (b) [Fe_3O_4] Fe-oct and (c) [γ-Fe_2O_3] Fe-oct estimated from fitting of R-plots. Solid and dotted lines represent Fe NPs oxidized at 200 °C and 250 °C respectively.

Figure 5.s1 Plot shows the variation of edge energies of Fe NPs with time when oxidized at 200 °C and 250 °C. Dashed lines represent the edge energies of bulk standards.

Figure 6.1. **(**a) Schematic diagram showing the synthesis of Co-Mn nanoparticles and the preparation of carbon and additive free electrodes using the EPD technique. (b) SEM image of a $Co_{3-x}Mn_xO_4$ (x=1.49) electrode assembled through EPD. Inset image shows clusters of nanoparticles. (c) TEM image of nanoparticles in the $Co_{3-x}Mn_xO_4$ (x=1.49) sample.

Figure 6.2. HAADF STEM imaging and EELS elemental mapping of nanoparticles in the $Co_{3-x}Mn_xO_4$ for x=1.49 (**a-f**), x=0.76 (**g**,**h**), and x=1.89 (**i**,**j**) samples. HAADF STEM images of (**a**) a particle oriented along the [211] direction of a spinel structure, diagramed in (**b**); (**c**) a nanoparticle with clear core-shell structure, showing a [100] rocksalt shell and a slightly off-axis [100] spinel core; and (**d**) a nanoparticle viewed in the [110] spinel direction (core) and rocksalt [110] (shell). (**e**) HAADF STEM image of a nanoparticle oriented along the [471] direction of a spinel structure and (**f**) the corresponding EELS elemental map, which shows a Co-rich shell and a Mn-rich core. (**g-j**) HAADF-STEM image of a nanoparticle of a spinel structure and the corresponding EELS elemental map that shows a Co-rich shell and a Mn-rich core for samples x=0.76 (**g**,**h**) and x=1.89 (**i**,**j**). Spinel structure referenced in Liu et al.[93]

Figure 6.3. X-ray diffraction (XRD) patterns of the $Co_{3-x}Mn_xO_4$ films. The bar patterns show the reference XRD pattern for Co_3O_4 (JCPDS: 01-071-4921) and $CoMn_2O_4$ (JCPDS: 01-077-0471). At higher Mn contents the intense (311) XRD peak (~37°) shifts towards lower angles, which is an indication of the presence of Mn in the Co_3O_4 lattice. The 29.2° and 32.9° peaks of $CoMn_2O_4$ (JCPDS: 01-077-0471) reference XRD pattern are aligned with the higher Mn-content samples.

Figure 6.4. (**a**) Cyclic voltammograms of Co_3O_4 and $Co_{3-x}Mn_xO_4$ electrodes for the six stoichiometries tested (x=0 to x=2.54) (acquired at a sweep rate of 25 mV/s). (**b**) Cyclic voltammograms of $Co_{3-x}Mn_xO_4$ (x=1.49) acquired in -1.0 to 0.4 V voltage window at 10, 25, and 50 mV/s sweep potentials. (**c**) Current density (at -0.3 V) as a function of sweep rate for different $Co_{3-x}Mn_xO_4$ compositions. Solid lines and dashed lines are linear fits to the anodic and cathodic contributions, respectively. The $Co_{3-x}Mn_xO_4$ (x=1.49) shows the highest current output at sweep rates from 5 to 50 mV/s. (**d**) Discharge profiles recorded at a constant current density of 1 A/g for $Co_{3-x}Mn_xO_4$ compositions. (**e**) Discharge profile for the $Co_{3-x}Mn_xO_4$ (x=1.49) electrode for different constant current densities. (**f**) Calculated specific capacitance at different constant discharge current densities for $Co_{3-x}Mn_xO_4$ (x=1.49) electrode.

Figure 6.5. Calculated values of (**a**) energy density, (**b**) power density and (**c**) specific capacitance for $Co_{3-x}Mn_xO_4$, x=0, 0.22, 0.76, 1.49, 1.89, and 2.54. To obtain the energy density and specific capacitance, the electrodes were discharged at a constant current density of 0.1 A/g. To obtain the maximum power density the supercapacitors were discharged within ~5s. The x=1.49 composition shows the highest energy density, power density, and specific capacitance.

Figure 6.6. (**a**) Comparison of Nyquist plots of electrodes with $Co_{3-x}Mn_xO_4$ composition x = 0, 1.49, and 2.54. Inset shows the modeled equivalent circuit. (**b**) Illustration of the contributions from the capacitive Q_s (green) and diffusion-controlled Q_d (red) charge to the total charge stored, at different sweep rates, for the x=0 and x=1.49 compositions. (Solid bars are x=1.49 and striped patterns are x=0, Co_3O_4). (**c**) Comparison of Ragone plots for $Co_{3-x}Mn_xO_4$ compositions. (**d**) Retention of capacitance as a function of cycles for the x=0 and x=1.49 electrodes. The cell was dis/charged at 0.25 A/g constant current over 300 cycles.

Figure 6.7. X-ray photoelectron spectroscopy of the x=1.49 $Co_{3-x}Mn_xO_4$ sample: (**a**) Co 2p, (**b**) Mn 2p, and (**c**) O 1s core electrons. These spectra show that both Co and Mn are present in both the 2+ and 3+ oxidation states. The strong peak of O 1s corresponds to oxygen atoms in oxides and the broad peak corresponds to hydroxyl groups of adsorbed water.

Figure 6.s1. (a-e) TEM images of Co-Mn metal nanoparticles prepared through thermal decomposition of $Co_2(CO)_8$ and $Mn_2(CO)_{10}$. The Co:Mn precursor is varied to vary the final composition. The precursor molar ratios of a) 1:0 b) 1:0.25, c) 1:0.5, d) 1:1, e) 1:2 and f) 1:4. TEMs are taken after drop casting sample solutions onto TEM grids (metal NPs) and direct annealing of the same grids in air (metal oxide NPs).

Figure 6.s2. **(a), (b), (c)** HAADF STEM images of $Co_{3-x}Mn_xO_4$ (x=1.49) nanoparticles **(above)** and corresponding direction in the spinel lattice **(below). (d)** HAADF STEM image **(top)** and EELS elemental mapping **(bottom)** of a typical nanoparticle in the $Co_{3-x}Mn_xO_4$ (x=1.49) sample. (**e-f**) Annotated HAADF image of main text Fig. 2c showing intermixing of heavy atoms (Co) in the shell. Some of the brighter atomic columns, representing a higher presence of Co, are marked with arrows (**e**). A line profile (**g**) taken across the surface atoms along a facet (**f**) shows variation in intensity between columns suggesting different amounts of Co present in each atomic column.

Figure 6.s3. **a**) Cyclic voltammograms recorded at different voltage windows to optimize the working potential window. **b**) Dependence of coulombic efficiency with different voltage windows.

Figure 6.s4. Kinetic behavior of $Co_{3-x}Mn_xO_4$ x=1.49 and x=0 (Co_3O_4) NP electrodes in -1.0 to 0.4 V voltage window. The charge/discharge time is between 28 and 280 s, which corresponds to the sweep rates from 5 to 50 mV/s.

Figure 6.s5. Cell voltage vs. charge and discharge time of an electrode having the x=1.49 composition, recorded at 1 A/g constant current density.

Figure 6.s6. Specific capacitance response to voltage for $Co_{3-x}Mn_xO_4$, x=0 and x=1.49 electrodes at a scan rate of 25 mV/s.

Figure 6.s7. The plot of total gravimetric charge against the reciprocal of the square root of potential sweep rate for a) Co_3O_4 b) $Co_{3-x}Mn_xO_4$ (x=1.49) electrodes. Inset equations show the relationship between Q_t and Q_s according to equation 8 and 9 (Eq8 and Eq9).

Figure 6.s8. Cyclic voltammograms recorded in three-electrode experiments using a scan rate of 50 mV/s.

LIST OF TABLES

the active electrode material, which is the total weight of electrode materials in our study since our active materials are additive-free.

Table 6.s5. Calculated values for Q_s and Q_d for Co_3O_4 and $Co_{3-x}Mn_xO_4$ (x=1.49) electrodes for different sweep rates. It is assumed that Q_s behaves linearly with the range of sweep rates.

Table 6.s6. Comparison of specific capacitances of $Co_{3-x}Mn_xO_4$ (x=0.22), $Co_{3-x}Mn_xO_4$ (x=0.76), $Co_{3-x}Mn_xO_4$ (x=1.49), $Co_{3-x}Mn_xO_4$ (x=1.89), and $Co_{3-x}Mn_xO_4$ (x=2.54) from three-electrode measurements. Specific capacitance were normalized to the weight of the active electrode material.

Part I

X-ray absorption spectroscopy study of oxidation of Iron nanoparticles in air

Chapter 1: Introduction

1.1 X-ray absorption fine edge spectroscopy

X-ray absorption fine edge spectroscopy (XAFS) is a powerful characterization technique which provides details based on the photons with energy within the range of core level binding energies of an atom being absorbed by that atom. Analyzing such spectra can provide information sensitive to the species, distance and co-ordination number of the surrounding atoms with respect to the central atom being probed, in addition to the information on chemical oxidation state of the central atoms. Such sensitivity of XAFS spectra can be utilized to explore chemistry and short-range order of the samples, which is not possible with other characterization techniques. For example, in case of amorphous materials, x-ray diffraction cannot be utilized to explore the material because of the absence of long-range order, in which case XAFS can be of great use. Due to such versatility, XAFS is used in a wide range of scientific studies including materials science[10], biology[11,12], catalysis[13,14], and geological studies[15,16].

Over the past few decades, XAFS has made great advances XAFS in achieving the goal of providing useful information. Recent development of new synchrotron sources and advances in theory has further led to the success of XAFS. However, extracting all the information with precision and analyzing the data is often complicated and requires great expertise. The purpose of this thesis is to provide detailed knowledge on XAFS which could be utilized right from the initial step of preparing for the XAFS experiment, to the extraction, fitting and analysis part. To further help with the understanding, the thesis includes experimental data of Fe nanoparticles (NPs) which were oxidized in air at different temperature for different time intervals.

1.2 Nanotechnology and nanoparticles

Nanotechnology can be defined as formation and exploitation of functional materials, systems and devices through control of matter on a nanoscale (1 to 100 nm). Low dimensional nanomaterials, relevant to this study is a term generally used to encompass all zero dimensional building blocks, which could be amorphous or crystalline and are usually smaller than 10 nm. These nanomaterials show unusual physical and chemical properties as compared to bulk materials because of various factors such as (1) high surface to volume ratio which leads to higher reactivity because of high surface energy making it ideal for catalysis[17,18] or sensory applications[19,20]; (2) size dependent optical properties (Q dots[21,22]), mechanical properties (interconnects in chips), and melting point (metal nanoparticles).

1.3 Oxidation of Iron nanoparticles

Iron and iron-oxide nanoparticles are one of the most explored materials due to its vast range of applications in fields such as ferro-fluids[1], magnetic imaging resonance (MRI)[2], catalysts for hydrogenation reactions[23,24]. Additional advantage of iron based materials is its large scale availability in nature and its cost-effectiveness. Besides this, these NPs are relatively less toxic as compared to other nanomaterials, paving its way for further applications in future. However, the as synthesized Fe nanoparticles have high affinity for oxygen, and when exposed to atmospheric conditions, oxidize partially on the surface to form core-shell type structure[5,6] or hollow structures[7,8] in certain cases due to Kirkendall effect. Study of the oxidation process of Fe metal NPs with time and under different conditions could provide insight on underlying mechanisms involved. Since the as-synthesized Fe and oxidized particles have short range order, XAFS was

used as an additional characterization technique to probe the structure and composition of these particles.

Chapter 2. XAFS: Theory and Background

2.1 X-ray absorption spectroscopy

During the x-ray absorption spectroscopy (XAS) experiment, the sample is targeted with x-rays having energy in a fixed domain. If the incident photons have energy greater than the binding energy, the photons are absorbed by the atoms of the sample, leading to excitation of electrons from the core shells (1s or 2p).

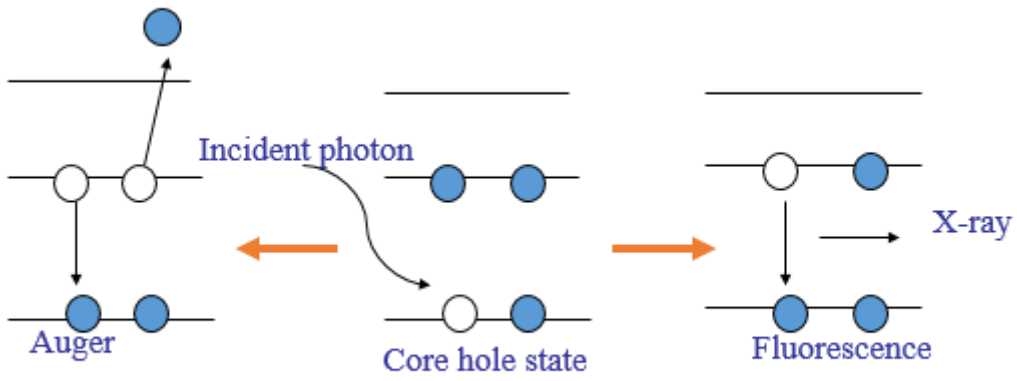

Figure 2.1. *Photoelectric effect in which absorbed photon ejects a core electron (center). The core hole is filled with either Auger electron leading to ejection of another electron (left), or another photon is ejected (right).*

After the removal of core electron from the central atom of the sample, the atom is said to be in excited state. The excited state eventually decays via 2 different processes (shown in **Figure 2.1**):

(1) X-ray fluorescence, in which an electron from higher shell fills the deeper core hole, ejecting a photon of a fixed defined energy. Thus, these energies characteristic of an atom can be used to distinguish or identify central atoms.

(2) The second de-excitation process is the Auger effect in which an electron from a higher shell drops to fill the core hole, with simultaneous ejection of another electron from the higher shell into continuum

Both these methods can be used to measure the absorption coefficient in fluorescence mode, with x-ray fluorescence more likely to happen at energies > 2200 eV.

When discussing about the XAS, the primary factor to be concerned about is the *absorption coefficient*, $\boldsymbol{\mu}$ which defines the probability of the incident photons being absorbed according to the Beer's Law:

$$I = I_0 e^{-\mu t} \tag{2.1}$$

where I_0 is the intensity of the incident x-rays, I is the intensity of the transmitted x-rays, and t is the sample thickness.

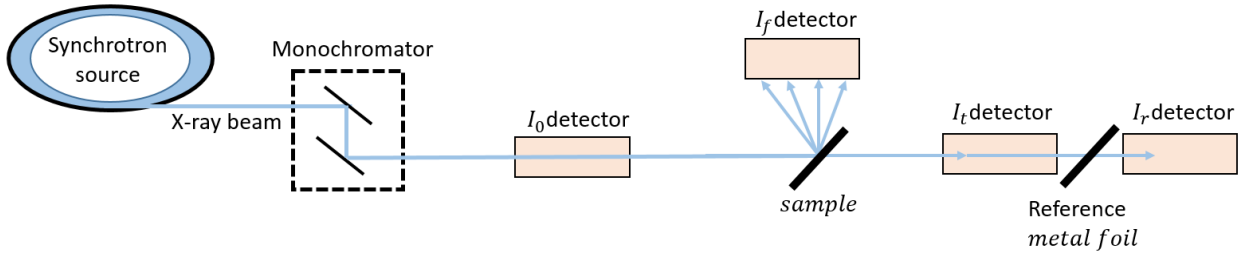

Figure 2.2. *Basic XAS experimental setup. The x-ray beam after exiting the synchrotron source, passes through a Monochromator. The incident intensity is measured in the I_0 detector. After the incident beam hits the sample, the transmitted beam is measured through the I_t detector whereas the intensity of the fluorescent photons are captured by the I_f detector.*

The number of non-absorbed photons are quantified with the help of detectors to measure the intensity of transmitted beam. In certain cases, when transmittance intensity is extremely low or due to other sample constraints, the absorbed x-rays are quantified by the fluorescent photons

ejected during the filling of the vacant core holes or alternatively measuring the auger electrons (electrons ejected during the filling of vacant core hole). For transmittance mode, *absorption coefficient* is defined as

$$\mu(E) = \ln\left(\frac{I_0}{I_t}\right) \tag{2.2}$$

Whereas for fluorescence mode, *absorption coefficient* is defined as

$$\mu(E) \propto \frac{I_f}{I_o} \tag{2.3}$$

Figure 2.3 shows a typical μ versus energy plot for Fe K-edge XAS. The absorption coefficient is normalized so as to negate the effect of thickness of the sample. The theoretical energy required to remove core electron from the K-shell of Fe is 7111 eV. Therefore, for the experiment the energy range is selected such that the absorption edge and the oscillations are in this range.

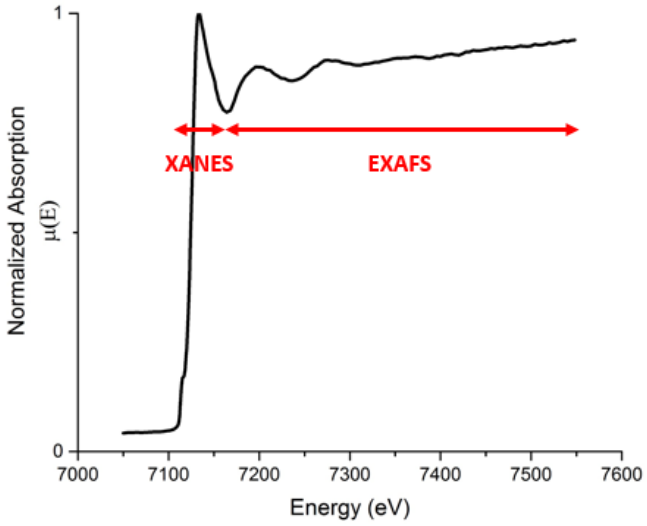

Figure 2.3. *XAS spectrum for Fe K-edge. Y-axis shows the normalized absorption coefficient and the x-axis is the energy of the incident x-rays. Plot also shows the XANES and EXAFS region which have been discussed in sections 2.2 and 2.3.*

2.2 X-ray absorption near-edge structure

When the incident x-rays have enough energy, the photons are absorbed by the sample, leading to a sharp rise of μ. The *edge energy*, $\boldsymbol{E_o}$ is defined somewhere in this region of sharp rise, which has been explained later. Since every element has a different $\boldsymbol{E_o}$ value, a variable x-ray energy synchrotron source is required. The theoretical $\boldsymbol{E_o}$ values for elements are well known and can be used as a basis for selecting the experimental energy range. The x-ray absorption near-edge spectra (XANES) is defined as the region typically within ± 30 eV of the $\boldsymbol{E_o}$ value. The interpretation and analysis of XANES region has been addressed later in chapter 4.

2.3 Extended x-ray absorption fine structure

2.3.1 Interference of photoelectron

After the photoelectron is ejected from the core shell of the atom by the incoming the x-rays, the photoelectron behaves as a wave propagating in all directions with a wavelength λ, given by the formula

$$\lambda = \frac{\mathrm{h}}{\mathrm{p}} \tag{2.4}$$

where $\boldsymbol{p}$ is the momentum of the electron and $\boldsymbol{h}$ is the Planck's constant.

The ejected photoelectrons scatters of the nearby atoms, and is deflected back towards the central absorbing atom. These photoelectron behaving as a wave, interferes with the other photoelectrons, leading to increase or decrease in electron density at the central atom due to constructive or destructive interference respectively, affecting the probability of the absorption of x-rays.

The condition for constructive interference could be defined as

$$2d = n\lambda \tag{2.5}$$

where ***n*** is an integer, and ***d*** is the distance between the central atom and the nearby scattering atom. Assuming the plane wave of photoelectron to be sinusoidal, the probability of absorption of photoelectron is modulated by a factor **χ,** defined as

$$\chi \propto \cos\left(2\pi \frac{2d}{\lambda}\right) \tag{2.6}$$

Wavenumber ***k*** is defined as

$$k = \frac{2\pi}{\lambda} \tag{2.7}$$

Using equation (2.7), equation (2.6) could be written as

$$\chi \propto \cos(2kd) \tag{2.8}$$

In terms of energy, wave number k can be defined as

$$k = \frac{1}{\hbar}\sqrt{2m_e(E - E_0)} \tag{2.9}$$

2.3.2 Scattering probability

Based on proportionality in equation (2.8), the oscillations are spaced regularly based on **k**. Therefore, on scanning the incident photon energy **E**, the value of **k** increases proportionally, leading to increase in the spread of the oscillations with energy, which can be observed in **Figure 2.3**. Another importance of these oscillations in that it is dependent on the distance between the central and the scattering atom ***d***, with smaller the ***d***, the less oscillatory the spectrum as a function of **E**. This could further be helpful in characterization of the samples.

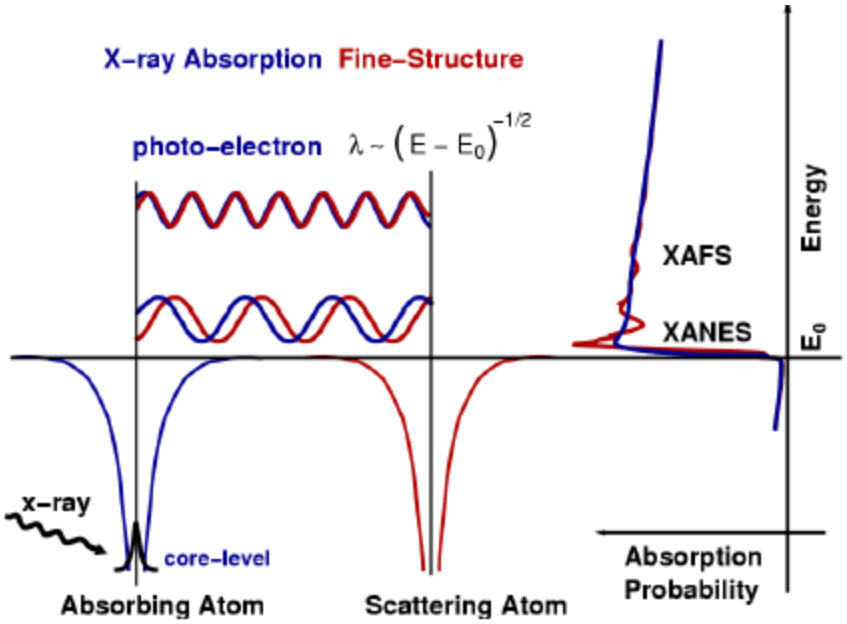

Figure 2.4. *Image showing generation of photoelectrons due to absorption of x-rays. This photoelectron scatters of neighboring atoms (left), leading to modulation of the absorption coefficient μ(E) (right).*[25]

Till now the model was based on the assumption that elastic scattering takes place between the photoelectron and the adjacent scattering atom. However, in case of inelastic scattering, loss of energy takes place leading to change in wavelengths and the interference pattern. In certain cases, the photoelectron can even fail to scatter at all. To consider these factors, a *proportionality constant* ***f(k)*** is defined which considers the probability of the scattering event taking place. Therefore, equation (2.9) can be further defined as

$$\chi = f(k) \cdot \cos(2kd) \tag{2.10}$$

The ***f(k)*** also consider certain geometrical factors such as in case of high atomic number atoms, probability of scattering decreases due to presence of large number of electrons, as compared to smaller atoms.

2.3.3 Multiple neighbor scattering

Another assumption made in the model is that scattering takes place with only one neighboring atom. The photoelectrons can scatter of multiple neighboring atoms which may or may not be of similar species. To consider this factor, each scattering event is considered separately, with total modulation now being defined as the sum of absorption probability of each scattering event. Therefore, equation (2.10) can be further refined as

$$\chi = \sum_i f_i(k) \cdot \cos(2kd_i) \tag{2.11}$$

To make the model more precise, atoms of similar species at equivalent locations relative to the central atom can be considered together. This degeneracy is defined as N_i.

$$\chi = \sum_i N_i f_i(k) \cdot \cos(2kd_i) \tag{2.12}$$

Based on this equation, EXAFS analysis provides details of the species, its degeneracy and the distance of atoms surrounding the central atom.

2.3.4 Multiple scattering paths

Examining further the theory of more than one neighbors, we could also consider the photoelectron scattered off neighboring atom being elastically scattered again off another neighboring atom, and then returning to the central absorbing atom. This event is defined as ***multiple scattering*** as compared to ***single*** or ***direct scattering*** event considered earlier. However, this does not affect the equation (2.12) if we generalize the d_i term. In direct scattering event, d_i is defined as the distance between the central atom to the scattering atom, whereas in case of multiple scattering, the d_i term is now defined as the ***path length*** of the photoelectron, or the half of the total distance travelled by the photoelectron.

2.3.5 Phase shifts and spherical waves

Till now we considered instantaneous change in direction of photoelectron after scattering event. However, in actual, a small phase change $\delta_i(k)$ is observed as the direction of photoelectron wave changes. As the photoelectron leaves the central atom, it crosses the low potential valley adjacent to the atom. Based on conservation of energy, this photoelectron will have a smaller velocity and a lower wavenumber once it exits the low potential well. Since this factor was not considered in the interference earlier, it now leads to phase shift $\delta_i(k)$. Therefore, equation (2.12) can now be written as

$$\chi = \sum_i N_i f_i(k) \cdot \sin(2kd_i + \delta_i(k)) \tag{2.13}$$

We also considered earlier that the photoelectron travels as a plane wave. However, in realty, the wave spreads outwards as the photoelectron moves away from the central atom, behaving as a ***spherical wave***. This leads to scattering probability decreasing proportionally to the square of distance. Therefore, the equation (2.13) now can be written as

$$\chi = \sum_i N_i \frac{f_i(k)}{kd_i^2} \cdot \sin(2kd_i + \delta_i(k)) \tag{2.14}$$

An additional factor of ***k*** has been added in the denominator so as to make the units of $f_i(k)$ consistent. This does not affect the overall equation because $f_i(k)$ is already a function of k.

2.3.6 Amplitude reduction factor

The final state of the central atom is different from the initial state as the absorption of the x-rays and ejection of photoelectron takes place. As the photoelectron leaves the central atom, it leaves a positively charged core hole near the nucleus of the central atom. Due to this, the positively

charged nucleus increase the pull on other electrons, leading to adjustment of the orbitals (shielding effect). This affect can be modeled by adding another constant to the equation. (2.14), defined as the *amplitude reduction factor* $\boldsymbol{S_0^2}$. Since this factor is due to intrinsic effects, it is considered constant for all scattering paths for a given central atom. Therefore, equation (2.14) can now be written as

$$\chi = S_0^2 \sum_i N_i \frac{f_i(k)}{kd_i^2} \cdot \sin(2kd_i + \delta_i(k)) \tag{2.15}$$

2.3.7 Mean free path

Rather than elastic collision, if the photoelectron scatters inelastically of the neighboring atom, leading to phonon scattering or excitation of valence atom of the scattering atom. This leads to change in the energy and interference condition, affecting the overall signals. As the photoelectron moves further form the central atom, probability of inelastic scattering increases further. Simultaneously, the core hole of central atom is filled by Auger electron due to non-availability of the photoelectron. This leads to change in the initial and the final state, removing the EXAFS signal. This effect can be considered by modifying the equation (2.15) to

$$\chi = S_0^2 \sum_i N_i e^{-\frac{2d_i}{\lambda(k)}} \cdot \frac{f_i(k)}{kd_i^2} \cdot \sin(2kd_i + \delta_i(k)) \tag{2.16}$$

where $\boldsymbol{\lambda(k)}$ is defined as the ***mean free path*** of the photoelectron.

2.3.8 Mean squared displacement

Till now, EXAFS was modeled based on a single central atom. However, in reality, when the sample is bombarded with x-rays during the experiment, a large number of photoelectrons are ejected from a large number of central atoms. Therefore, the signals detected by any of the

detectors are an average of all the independent similar events taking place. However, these events may or may not be exactly similar to each other, depending on a lot of factors such as (1) central atoms are present in multiple phases or at different sites within the lattice, (2) presence of defects or lack of crystallinity in the sample (*static disorder*), (3) composition gradient within the sample, and (4) change of environment due to thermal vibrations or vibration of chemical bonds (*thermal disorder*).

Case (1) has already been considered by including degeneracy of each individual path in equation (2.16). For cases (2) and (4), if the static and thermal disorders are considered small, the EXAFS equation can be modified by inclusion of another factor defined as *mean squared displacement* $\boldsymbol{\sigma^2}$

$$\chi(\mathrm{k}) = S_0^2 \sum_i N_i e^{-\frac{2d_i}{\lambda(k)}} \cdot e^{-2k^2\sigma_i^2} \cdot \frac{f_i(k)}{kd_i^2} \cdot \sin(2kd_i + \delta_i(k)) \qquad (2.17)$$

For cases (2), (3) and (4); if the disorders are large, then strategy similar to case (1) can be considered in which each event can be considered independently.

$\boldsymbol{\sigma^2}$ is also defined as the ***Debye-Waller factor*** or ***Mean square relative displacement*** (MSRD). MSRD is defined as the square of standard deviation of half path length:

$$\sigma^2 = \langle (r - \bar{r}^2)^2 \rangle \qquad (2.18)$$

To explain further, this factor considers the individual path lengths which have contributions from scattering paths slightly closer or further apart than the average because of the thermal/static disorders.

2.3.9 Final EXAFS equation

Considering all the factors discussed in sections above, the final EXAFS equation is described in equation (2.17). This EXAFS equation forms the basis of the analysis of sample which has been discussed in later sections.

$$\chi(\mathrm{k}) = S_0^2 \sum_i N_i e^{-\frac{2d_i}{\lambda(k)}} \cdot e^{-2k^2\sigma_i^2} \cdot \frac{f_i(k)}{kd_i^2} \cdot \sin(2kd_i + \delta_i(k))$$

Note: Details about planning the experiment and data collection during the experiment are beyond the scope of this thesis, and can be found in literature[26]. The following sections have been written on the assumption that the user have the raw data in hand with the basic knowledge about the experimental setup, for example, whether the XAFS experiment was done in transmission or fluorescence mode. The raw data should consist of details about the photon count in each detector corresponding to the energy of the incident x-rays, for all the individual scans.

Chapter 3. XAFS data processing

3.1 Description of experimental setup

The XAFS experiment can be carried out in either transmission mode or in fluorescence mode based on the sample and experimental conditions. For this study, the data was collected in both transmission and fluorescence mode simultaneously, using the experimental setup shown in **Figure 2.2**. Since transmitted data plots showed high noise to signal ratio, fluorescence data of sample was used for the analysis. Theoretically, absorption coefficient spectrum (μ(E) vs E) plotted using fluorescence data and transmitted data of sample show similar characteristics. Use of transmitted reference data should not affect the accuracy of the analysis since it is required only for energy calibration and not any actual calculations.

The incident x-ray beam exiting the synchrotron source passes through a monochromator which uses Bragg diffraction to allow photons of certain specific energies to pass through it. This beam then passes through a detector which measures the incident number of photons (I_0) hitting the sample. Some of these incident photons which do not get absorbed by the central atoms of the sample are transmitted through the sample which are detected by the detector (I_t), whereas some of the absorbed x-rays emit photons which are detected by detectors placed perpendicular to the sample (I_f). The transmitted beam passes through a reference metal foil (iron foil in this case), which leads to further attenuation of transmitted beam which has intensity I_r.

These metal foils which have a known E_0, are used for energy calibration for the position of the absorption edges of samples. Based on the shift of experimental E_0 of metal foil, shift in energy can be added or subtracted to the experimental E_0 values of the unknown samples to get its absolute E_0 value. It is also important to note that the range of energy of incident x-rays are chosen carefully

so as to include specific transitions from core shell of central atoms. For example, for the current experiment, the XAFS data was collected for Fe k-edge transitions. Fe, Fe_3O_4 and Fe_2O_3 have edge energies 7111eV, 7121 eV and 7121.5 eV respectively (as the cationic charge on the central atom increases, photons of increasing energies are required to knock the electron off of the k-shell). Therefore, during the experiment, the energy of incident x-rays was scanned from 7050 eV to 7550 eV, well beyond the theoretical E_0 value so as to record the EXAFS region of the spectrum.

3.2 Handling of raw XAFS data

3.2.1 Converting raw data to μ(E)

First step for understanding the raw data is to differentiate between the various intensity columns for a particular scan so that the absorption coefficient spectrum can be plotted. **Figure 3.1** shows the plot of counts of incident photons on all detectors as a function of energy. During the experiment, energy of incident x-rays were changed when the count of photons passing through the I_0 detector was equal to 500,000. Therefore I_0 detector counts remain constant with change in energy (**Figure 3.1a**). The count of photons passing though the sample as a function of energy is shown in **Figure 3.1b**. As the energy of incident photon increases, more number of photons can pass easily through the sample without being completely attenuated, leading to a constant increase. A sharp drop is observed at a certain specific energy ranges because the photons have energy required for ionization of 1s electrons, getting absorbed in the process. Equivalent plot is observed for reference detector count in **Figure 3.1c** because it is similar to the previous case with the only difference being I_t is the number of photons incident on the reference foil and I_f being the number of photons transmitted through the reference. It is important to note that $I_0 > I_t > I_f$ because not

all photons get transmitted through the sample or the reference foil. **Figure 3.1d** shows the count of photons detected by the detector as a function of energy. Since I_0 is constant, from equation (2.3), implying $\mu(E) \propto I_0$, therefore the plot characteristics are similar to the absorption coefficient spectrum. For this experiment, I_f is sum of several signals from a multi-element detector (vortex 1 + vortex 2 + vortex 3 + vortex 4) so as to prevent saturation of individual detector.

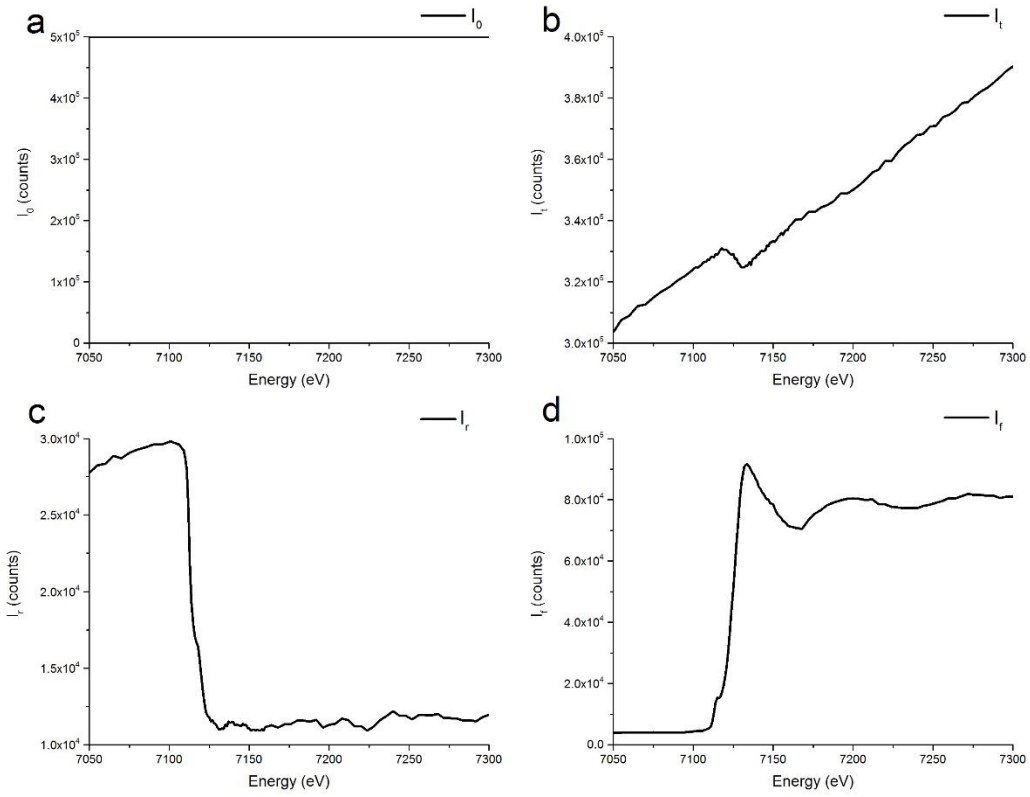

Figure 3.1. *Characteristic plot shows the count of the photons detected by the detectors (a) I_o, (b) I_t, (c) I_r and the fluorescence detector (d) I_f*

For transmission data, μ(E) is defined using equation (2.2) as $\mu(E) = \ln\left(\frac{I_0}{I_t}\right)$ for the sample and $\mu(E) = \ln\left(\frac{I_t}{I_r}\right)$ for the reference foil. For fluorescence data, from equation (2.3), $(E) \propto \frac{I_f}{I_o}$. Using these formulae, the absorption spectrum can be plotted for all individual scans.

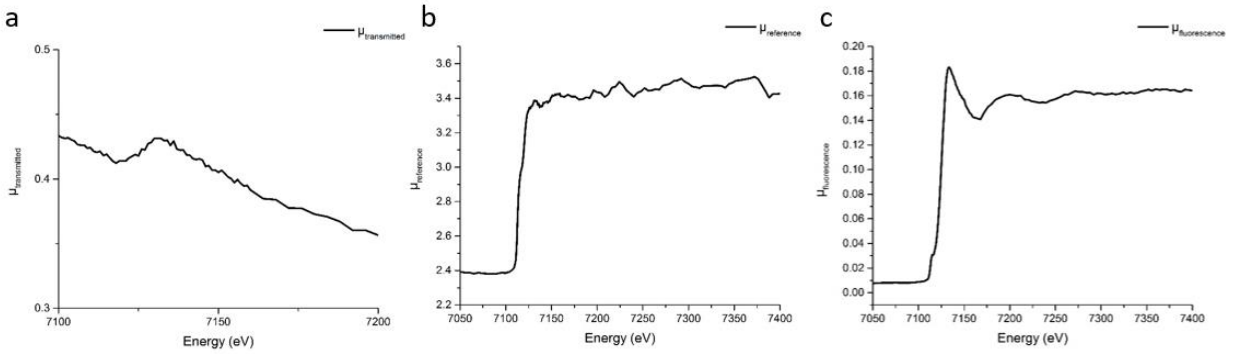

Figure 3.2. *Plot shows raw absorption spectrum for (a) transmitted, (b) reference and (c) fluorescence spectra. Fluorescence spectrum rather than transmitted spectrum was used for XANES and EXAFS analysis because of low noise to signal ratio. Reference spectrum was used for energy calibration of the data.*

The raw absorption coefficient spectra data obtained at **Cornell High Energy Synchrotron Source** (CHESS) was processed using IFEFFIT, consisting of ***ATHENA***® and ***Artemis***® software, an interactive tool for XAFS analysis. The data processing included edge energy determination, background removal, normalization and Fourier transform. The following sections will give details on handling of data using ATHENA following which the data can be used for XANES and EXAFS analysis.

3.2.2 Importing raw data into ATHENA®

Raw data obtained after the experiment is in the form of a spec file. It contains all of the input parameters for all scans, except for the data obtained from fluorescence detectors (vortex 1, 2, 3 and 4) which is stored separately for each scan. It is important to note than multiple scans are carried out for each sample under exact similar conditions, which are later merged to reduce noise. The raw spec file obtained is broken into several files corresponding to each individual scan. It contains columns for energy and photon count of detectors I_0, I_t and I_r for each energy value. This file is then merged with vortex files corresponding to that scan number. The final file for each scan thus consists of 4 columns from spec file and 4 columns of the 4 vortex detectors. This file is now ready to be imported into ATHENA.

On importing data in ATHENA, it asks which columns corresponds for energy, numerator and denominator, and what mathematical functions are required for the numerator/denominator. For transmitted data, using equation (2.2); $\mu(E)_{transmitted} = \ln\left(\frac{I_0}{I_t}\right)$. Therefore, column corresponding to I_o and I_t are chosen as numerator and denominator respectively, followed by selection of natural log function. However, since fluorescence data was used for analysis, and $\mu(E)_{flourescence} \propto \frac{I_f}{I_o}$; numerator is selected as I_f and denominator as I_o. Since there are 4 vortex detectors, 4 columns are selected for numerator, and ATHENA carries out its sum automatically. In the same window in ATHENA, there is also an option of importing the reference data from the same file. For reference spectra, since $\mu(E)_{reference} = \ln\left(\frac{I_t}{I_r}\right)$, I_t and I_r are selected as numerator and denominator respectively. All the scans for a particular sample can be imported together if the files have same column positions. On importing, ATHENA plots the absorption coefficient spectrum plots for all the scans.

3.2.3 Data deglitching and truncation

After importing all the scans corresponding to a particular sample, each absorption spectra plot is observed visually for any unwanted features. Any sharp drops between two points can be removed by selecting the deglitching option at that point. Deglitching replaces that point by an average value of its adjacent data points. Energy ranges at the ends, not having any useful information are removed by truncating the data. If a particular scan shows vastly different features as compared to other scans for a given sample, it should be discarded.

3.2.4 Alignment of reference scans

Since monochromators do not retain energy calibration with successive scans, alignment is required to move all the absorption spectrums on to an absolute energy grid. The references are aligned with respect to one of the reference by selecting it as a standard. After alignment, the movement of each adjusted spectrum is indicated by the 'energy shift' value. For each scan, since reference data is measured simultaneously with the sample data, the sample absorption spectrum is also shifted by the same value of 'energy shift' as that of the reference data.

3.2.5 Merging of data

Now the individual scans for a particular sample are ready to be merged. On selecting all the scans in the group list and merging the μ(E) data, ATHENA generates a merge spectra file and plots the merged data absorption spectra along with the standard deviations. It also generates a merge spectra of reference channels which can be used for alignment of merged data if required. For merging, each spectra is given an importance factor with a default value of 1, which can be varied

to calculate the weighted average of the spectrum. The individual scan files can be discarded now and the merged file is given the sample name.

3.2.6 Calibration of data to choose E_0

E_0 is defined as the edge energy or the energy required by the photons to ionize electrons from the k-shell of the central atom. From **Figure 3.2c**, it can be observed that the sharp rise of absorption coefficient takes place within an energy range rather than a fixed energy value. This implies, that there is no fixed E_0 value but rather a range of values. Therefore, rather than finding the E_0 value, we choose the E_0 value which is somewhat arbitrary and can be done in a number of ways:

(1) Choosing the first inflection point of the absorption coefficient spectrum which is also the peak of the 1st derivative plot
(2) Local maxima of the absorption spectra plot, also called the white line
(3) Energy at which double derivate of the absorption spectra plot equals 0

Based on observations, the experimental data contains a lot of noise at the peaks of the absorption and the 1st derivate plot. Therefore, option (3) is usually used to reliably choose the correct E_0 value. It should be noted that same procedure should be followed for choosing E_0 value if comparison of data between various samples is required.

3.3 Normalization and Background removal

The raw absorption coefficient depends on a lot of experimental factors such as the thickness of the sample, solid angle covered by the vortex detectors, use of filters, etc. Since XAFS analysis is

highly dependent of comparison of data between different samples, normalization of absorption coefficient is required to remove the effect of these external factors.

3.3.1 Normalization of μ(E)

The '*pre-edge range*' and '*normalization range*' are defined as two regions on the un-normalized absorption spectrum plot before and after the edge respectively. A straight line called the pre-edge is drawn on the data in the pre-edge range, whereas a polynomial function called the post-edge is used to map the spectrum in the normalization range. All the data points within these ranges are used to map the pre-edge and post-edge onto the spectrum, therefore they are not highly dependent on the exact boundary of these ranges. The post-edge can be mapped using a 1st order, 2nd order or a 3rd order polynomial function. **Figure 3.3** shows an un-normalized absorption spectrum with pre-edge and post-edge highlighted. The pre-edge range and post edge range for this plot are defined to be [-78,-30] eV and [150,320] eV respectively, with respect to E_0 (i.e. assuming E_0 = 0 eV). 2nd order polynomial function is used to map the post-edge region.

The relationship between μ(E) and χ(E) is given by

$$\mu(E) = \mu_0(E) \cdot [1 + \chi(E)] \tag{3.1}$$

Therefore,

$$\chi(E) = \frac{\mu(E) - \mu_0(E)}{\mu_0(E)} \tag{3.2}$$

χ(E) is the normalized oscillatory part of absorption coefficient, μ(E) is the measured absorption coefficient, μ_0(E) is the absorption coefficient with no contribution from neighboring atoms. Since

μ_0(E) in the denominator is just a multiplication constant, it is replaced by a constant edge step in order to limit normalized χ(E) within a range of 0 to 1.

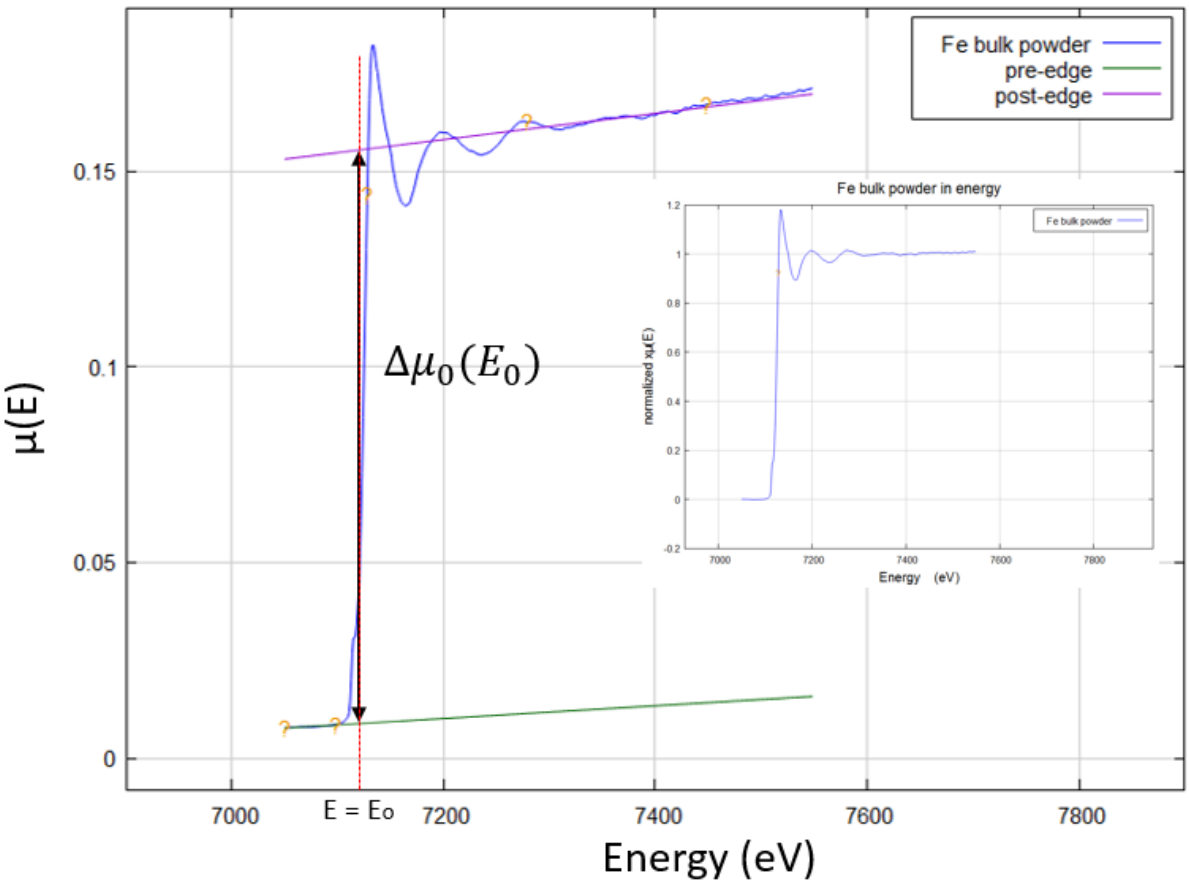

Figure 3.3. *Plot shows un-normalized absorption spectrum along with pre-edge and post-edge. The pre-edge range and post edge range for this plot are defined to be [-78,-30] eV and [150,320] eV respectively, with respect to E_0 (i.e. assuming E_0 = 0 eV). 2nd order polynomial function was used to map the post-edge region. Inset shows the normalized absorption spectrum plot.*

The *edge step*, $\Delta\mu_0(E_0)$, shown in **Figure 3.3**, is calculated by extrapolating the pre-edge and post-edge lines to E_0 value followed by subtraction the value of pre-edge at E_0 from the value of post-edge at E_0. The pre-edge line is now subtracted from the data (i.e. pre-edge is now y = 0 line), and then divided by the edge step to scale the normalized absorption spectrum χ(E), shown in the inset of **Figure 3.3**.

3.3.2 Background removal

Data reduction carried out till now is sufficient to proceed for XANES analysis. However, since EXAFS refers to the oscillatory part of the spectrum, i.e. $\chi(E)$, background subtraction is required to proceed further. Since we do not have the measured value of $\mu_0(E)$, i.e. the absorption coefficient from an isolated atom with no contribution from the surrounding atoms, $\mu_0(E)$ is approximated with a smooth spline. This spline is referred to as the background. In ATHENA, background selection is carried out using the AUTOBK algorithm[27]. However, while using this algorithm, the ends of the spline are not well defined which sometimes results in the end of spline deviating slightly away from the $\mu(E)$ data. To prevent this, ATHENA provides the option of *spline clamps*. The user can limit the freedom of the spline to oscillate by increasing the number of spline knots by selecting one of the six predefined values of spline clamps.

For background removal, another parameter 'k-weight' is defined which is used to emphasize the lower end or the upper end of the $\mu(E)$ data with respect to the background data. For example, for oscillatory $\mu(E)$ which is small but well distinguishable from the noise at the high energy, generates a better $\chi(E)$ spectrum for high k-weights. It is important to note than this k-weight is different from the k-weighting used for plotting Fourier transforms which has been discussed in the next paragraph.

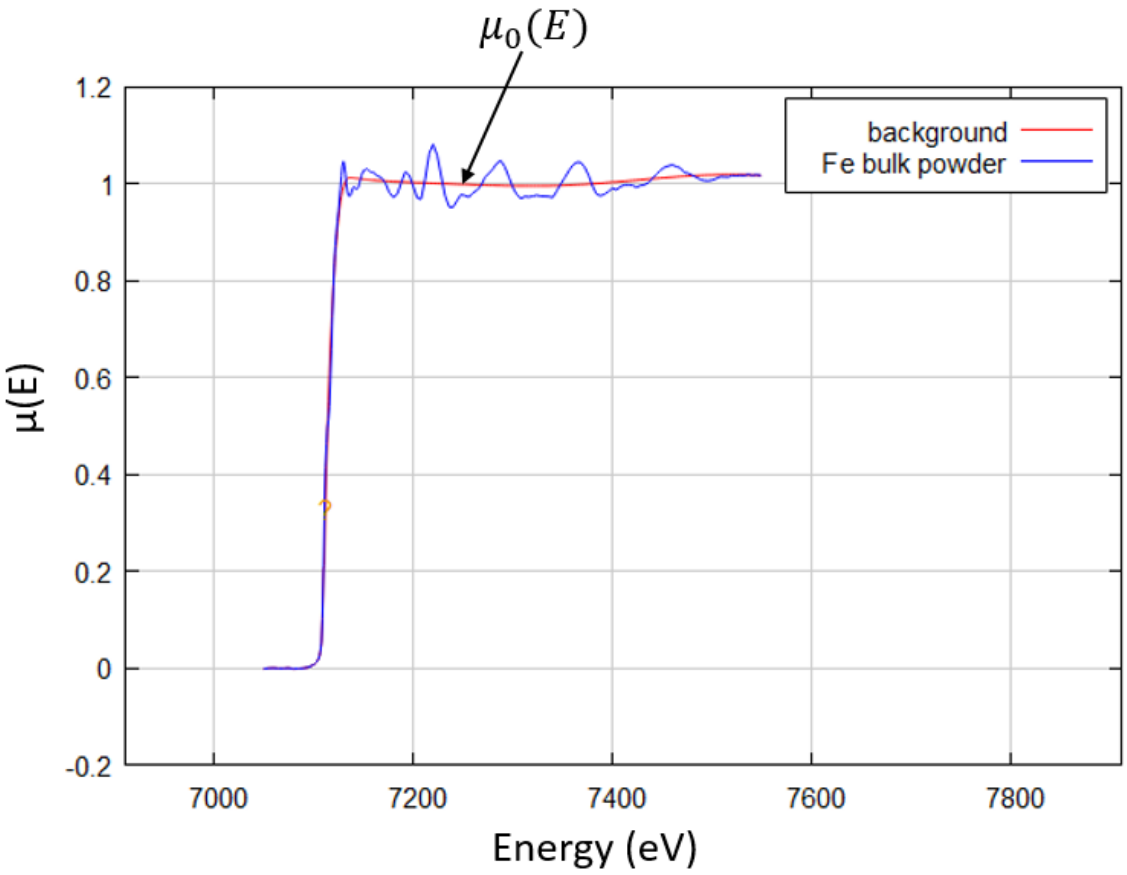

Figure 3.4. *Plot shows the bare-atom background $\mu_0(E)$ estimated using the AUTOBK algorithm*

Subtracting background from μ(E) and normalization provides the χ(E) spectrum, which also can be plotted as a function of wavenumber *k* using the equation (2.9). Based on equation (2.17), χ(k) decreases in amplitude with increase in k because of the factor $e^{-2k^2\sigma_i^2}$. Therefore, χ(k) is often multiplied by a factor of k, k^2 *or* k^3 in order to plot the spectrum with a more uniform amplitude. This is called *k-weighting*, and is different from the w-weight used for background removal. For example, for low z-elements, scattering amplitudes peaks at low wavenumbers and become quite low at high wavenumbers; whereas high z-elements such as transition metals have small scattering amplitudes at low k but continue to increase with increasing k. Therefore, by weighting χ(k), the high and low portions of the spectrum can be emphasized differently in the Fourier transform.

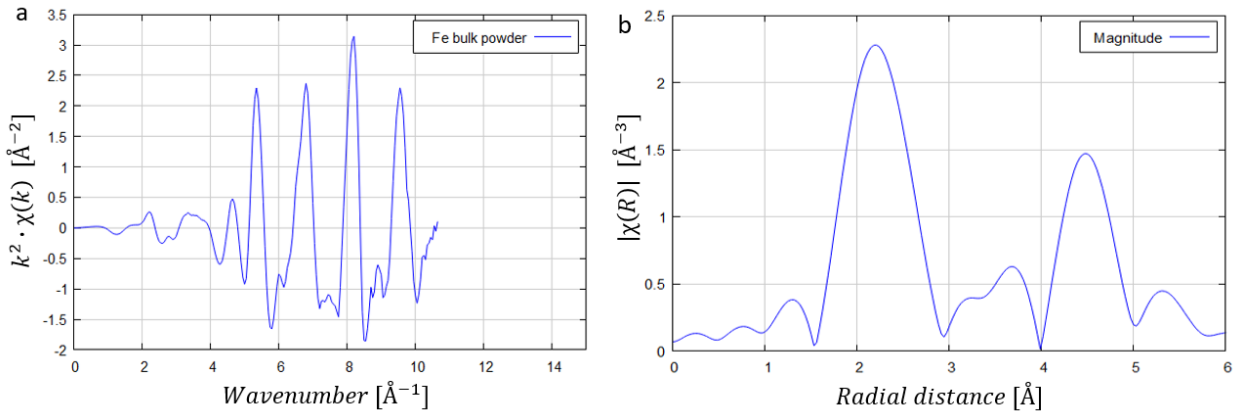

Figure 3.5. *(a) Plot shows k^2 weighted χ(k) for bulk iron powder (b) Fourier transformed χ(R) spectrum plotted with a k-weight of 2.*

3.4 Fourier transformation: χ(k) to χ(R)

χ(k) plotted in **Figure 3.5a** shows a considerable sinusoidal spectrum. The larger peaks are equally spaced, with some smaller peaks visible in-between which do not follow sinusoidal pattern. Since Fe atoms are in nearly-similar environment with minor variations such as defects or thermal vibrations, multiple terms in the EXAFS equation are significant as compared to others. On summation of these individual terms in the EXAFS equation with different amplitudes and phases, it generates a spectrum similar to shown in **Figure 3.5a**. Therefore, to decompose the spectrum into constituent sine waves, Fourier transformation of χ(k) to χ(R) is carried out. The Fourier transformed spectrum shown in **Figure 3.5b** yields multiple peaks corresponding to each neighboring atom at well-defined distances from the central atom. These Fourier transformed plots are referred to as the '***R-space***' plots. It is important to note that R-space plots are not radial-distribution function, i.e. the position of peaks in R-space are not similar to the D_i, the distance between the central and the scatterer atoms. An important parameter used in Athena is the 'Rbkg'

or the R background, the value below which the AUTOBK algorithm removes the Fourier component of the data which is usually associated with the noise. The k-range selected for Fourier transform is usually chosen to be the nodes one or two cycles away from the ends in order to facilitate better fitting of the data for EXAFS analysis.

3.5 Approach to XAFS analysis

After getting the R-space plots, the raw data processing is now complete for both XANES and EXAFS analysis. Besides XANES and EXAFS, additional techniques such as *Fingerprinting* and *Principal Component analysis* could be used for the analysis of XAFS data. The following chapters will discuss how the XANES and EXAFS analysis are carried out before moving on to discuss the results of the XAFS study of iron nanoparticle oxidation under different conditions.

Chapter 4. Analysis of XAFS Spectra

4.1 XANES: Linear Combination fitting

The normalized absorption coefficient spectrum μ(E) can be expressed as a linear combination of the spectra of its constituents. For example, for this study, oxidation of Fe NPs was carried out at 200 ^{0}C and 250 ^{0}C for up to 3 hours. The oxidized nanoparticles constituted of mixed phases including Fe, Fe_2O_3 and Fe_3O_4, implying that the Fe atoms in oxidized nanoparticles are present in 3 different environments. Therefore, the normalized XAFS spectrum of oxidized nanoparticles can be expressed as a sum of the weighted normalized spectrum of its constituents, i.e. Fe, Fe_2O_3 and Fe_3O_4, with their ratios varying with the extent of oxidation. This technique is referred to as the *Linear Combination fitting* (LCF) and is used for the analysis of the XANES spectra.

For further explanation, if we assume the oxidized NPs to be consisting of just 2 layers; Fe_2O_3 at the surface and Fe_3O_4 as the back layer, then according to the Beer Lamberts law, the intensity of the x-rays after passing through the top layer of sample i.e. Fe_2O_3 is given by:

$$I_{Fe_2O_3} = I_0 e^{-\mu_{Fe_2O_3} t_{Fe_2O_3}} \quad (4.1)$$

This beam after crossing Fe_2O_3 passes through the layer of Fe_3O_4, and gets attenuated again with its intensity given by:

$$I_{Fe_3O_4} = I_{Fe_2O_3} \cdot e^{-\mu_{Fe_3O_4} t_{Fe_3O_4}} = I_0 e^{-(\mu_{Fe_2O_3} t_{Fe_2O_3} + \mu_{Fe_3O_4} t_{Fe_3O_4})} \quad (4.2)$$

Therefore, the absorption of sample is just the sum of its constituent layers, which can be exploited for the XANES analysis. It is important to note that the absorption from a given phase is proportional to the number of absorbing atoms present in that phase, which gives us neither the molar ratio or the ratio of mass of the constituents but rather just the ratio of central atoms present

in each phase. Therefore, it is important to change these results in more familiar units when comparing the results of XAFS with other characterization techniques.

Consider the Fe K-edge spectrum of iron nanoparticles oxidized in air at 200 ^{0}C for 60 mins, shown in **Figure 4.1**. The fit of the spectrum of sample was carried out using the spectrum of bulk powders of Fe, Fe_2O_3 and Fe_3O_4, from now on referred to as the standards. The fit is fairly accurate with the residual values less than 5%. Inset table shows the ratio of constituents present in the sample as 0:0.62:0.38 for Fe, Fe_2O_3 and Fe_3O_4 respectively.

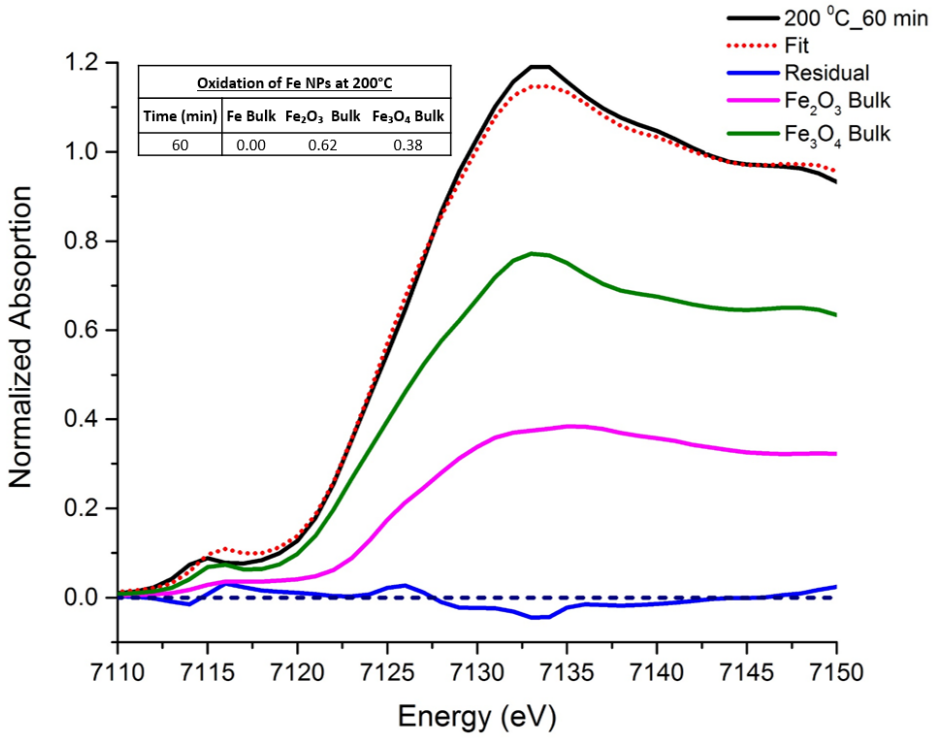

Figure 4.1. *Plot shows fitting of normalized Fe K-edge spectrum of Fe NPs oxidized at 200 ^{0}C for 60 mins. Bulk standards Fe, Fe_2O_3 and Fe_3O_4 were used for the linear combination fitting. Dotted red line shows the fit of the spectra and dashed line represents the residual (difference between spectrum and fit). Inset table shows ratio of bulk standards present in the sample evaluated using the fit.*

During fit, the E_o values of the standards are allowed to float so as to increase the quality of the fit. This is because of the inconsistent energy calibration during the experiment and data processing. It is worth mentioning that if the shift in E_o value is fairly big, then there might be some inconsistencies in the fit such as missing of a standard from the fit. To quantity the mismatch between the spectrum of sample and the fit, a term '*R-factor'* is used which is defined as the sum of difference between data points squared, normalized by the sum of data points squared. Therefore, R-factor is given by the equation:

$$R = \sqrt{\frac{\sum_{i=1}^{N}(data_i - fit_i)^2}{\sum_{i=1}^{N}(data_i)^2}} \tag{4.3}$$

For the fit shown in **Figure 4.1**, the R-factor was computed to be 1.628×10^{-3}.

4.2 EXAFS data analysis

One of the most important technique used for the XAFS analysis is the fitting of the χ spectrum in k-space or R-space to obtain various parameters of the unknown sample using the equation (4.4) to (4.6). In EXAFS analysis, a model structure or simply referred to as the standards are used to obtain a spectrum in order to facilitate the fitting of the sample spectrum. The process involves implementing various modifications to the final structure as well to increase the quality of the fit. Equations (4.4) to (4.6) shown below highlights the various unknown parameters of the sample. Variables highlighted in red shows the parameters calculated theoretically whereas parameters shown in blue are determined from the fitting of the χ spectrum, also shown in **Table 4.1**.

$$\chi(\mathrm{k}) = S_0^2 \sum_i N_i e^{-\frac{2d_i}{\lambda(k)}} \cdot e^{-2k^2\sigma_i^2} \cdot \frac{f_i(k)}{kd_i^2} \cdot \sin(2kd_i + \delta_i(k)) \qquad (4.4)$$

where $$R_i = \frac{d_i}{2} = R_0 + \Delta R \qquad (4.5)$$

and $$k^2 = \frac{2m_e(E-E_0)}{\hbar} \qquad (4.6)$$

Theoretically calculated values	Parameters determined from fitting of data
$f_i(k)$ effective scattering amplitude	N_i path degeneracy (co-ordination #)
$\delta_i(k)$ effective scattering phase shift	S_0^2 amplitude reduction factor
$\lambda(k)$ mean free path	σ_i^2 mean square displacement
R_o initial path length	E_o energy shift
	ΔR change in path-length

Table 4.1. *Table shows the various parameters present in the equation (4.4). Parameters in the left column shown in red, are calculated theoretically and the parameters in the right column highlighted in blue are determined from fitting the χ spectrum.*

The theoretical calculation and the fitting of the parameters was carried out with the help of the IFFEFIT[28] package using the ARTEMIS software. ARTEMIS is an interactive tool which uses the theoretical standards computed by the FEFF[29,30] and ATOMS[31] program.

4.2.1 ATOMS and FEFF

ATOMS program is an application that provides the crystallographic details and the structural data of a molecule which is useful for the EXAFS analysis. The crystallographic data such as the space group, lattice constants and angles are the input data required to run ATOMS. It also requires the

central atoms and the cluster size which is the radial distance to which FEFF takes into consideration the effect of neighboring atoms. After running ATOMS, the output file generated consists of the x, y and z co-ordinates of the neighboring atoms up to the earlier defined cluster size. It also assigns a potential number referring to the crystallographic site and a tag to each unique element with respect to the central atom. For example, in case of Fe element, which has a body centered cubic (BCC) structure, the central Fe atom with co-ordinates (0, 0, 0) is give a potential of 0 and a tag of Fe1. The nearest neighbors of central Fe atom are present in identical crystallographic sites, therefore they are given the same potential of 1 and a tag of Fe11, with the only difference being in their co-ordinates. The second nearest neighbors are also present at the crystallographic sites similar to the nearest neighboring atoms, therefore they are again given the same potential of 1 but a tag Fe12 with 2 referring to the second nearest neighbors for a given crystallographic site.

The output file of ATOMS referred to as the .inp or a CIF file is then used by the FEFF to calculate theoretical XAFS spectrum of a molecule. ARTEMIS provides the platform for importing the .inp file and carrying out the FEFF analysis. After running FEFF, the program compiles the neighboring atoms with the same tags into a single path with its degeneracy (N) being the number of such identical atoms or the number of identical routes traversed by the photoelectron. It also computes the radial distance for that path, i.e. the distance between the central atom and the scattering neighboring atom.

Table 4.2 shows 1st 6 scattering paths for Fe element generated using FEFF. Column 3 shows the R_{eff} or R_0 value i.e. the distance between the central atom and the scattering atom for the case of single scattering; or half of the distance travelled by the photoelectron in case of multiple scattering event. Column 4 shows the various scattering paths, implying the path traversed by the

photoelectron. For example, Fe_12 scattering path means the photoelectron ejected from the central atom, got scattered from the second nearest neighboring atom and got absorbed again by the central atom, also referred to as *single* or *direct scattering path*. Fe_11 Fe_12 path means the ejected photoelectron travels away from the central atom, get scatters by nearest neighbor Fe11, then get scatters by second nearest neighbor Fe12 before being absorbed back again by the central atom, referred to as *double* or *multiple scattering path*. **Figure 4.2** shows a typical single and multiple scattering path of the photoelectron.

#	Degeneracy (theoretical)	R_{eff} (Å)	Scattering Path	Scattering Type
1	8	2.485	Fe_11	single
2	6	2.870	Fe_12	single
3	24	3.920	Fe_11 Fe_11	other double
4	48	3.920	Fe_11 Fe_12	other double
5	12	4.059	Fe_13	single
6	48	4.151	Fe_11 Fe_13	other double

Table 4.2. *Table shows the path file for Fe element generated using FEFF in ARTEMIS*

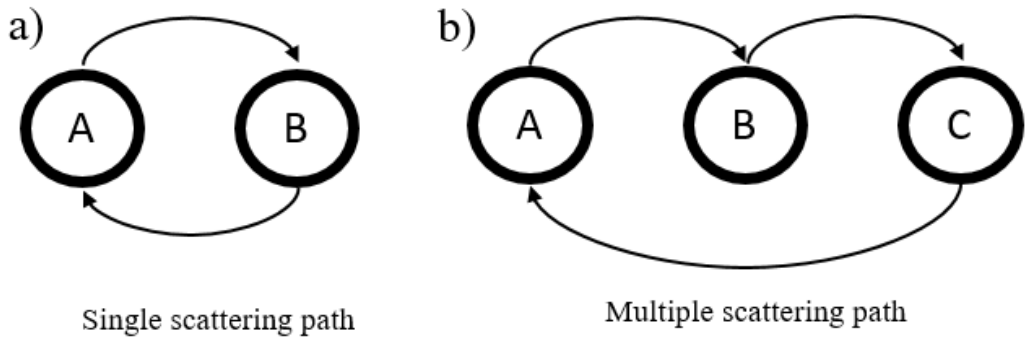

Figure 4.2. *Diagram shows a typical (a) single scattering path and (b) multiple scattering path traversed by the photoelectron. Atom A refers to the central atom, B and C refers to the neighboring scattering atoms.*

4.2.2 Fitting parameters

It is important to understand the concepts behind the fitting parameters before computing their values by fitting the spectrum. The following section will discuss the physical meaning of each fitting parameter, their reasonable values, its effect on χ(k) and how they correlate with each other. These 5 parameters namely, the degeneracy N, the mean squared relative displacement (MSRD) σ^2, the amplitude reduction factor S_0^2, the path length $R_i$and the edge energy E_0 are allowed to float so as to compute their values.

a) The ***degeneracy N***, also referred to as the co-ordination number, is the number of identical atoms surrounding the central atom. It is the number of distinct ways the photoelectron can travel such that it follows the same path. In case of nanomaterials, a drop in degeneracy is usually observed due to the presence of larger ratio of atoms on the surface of the particle. In case of 2 phase system, for example, iron atoms present as Fe and Fe_2O_3, photoelectron follows different paths for scattering with nearest Fe atoms. Therefore, the degeneracy drops proportionally to the ratio of the phase present in the system. Typically, values of N can vary vastly depending on the path.

   In case of bulk materials, the values of N are considered to be ideal due to the presence of long range order, therefore fitting of N is not required for bulk materials. This helps reduce the number of fitting variables which is advantageous because of the constraints on how many variables can be fitted. The number of independent fitting parameters N_{ifp} are calculated using the Nyquist criterion and is given by the equation:

$$N_{ifp} = \frac{2\Delta k \Delta R}{\pi} \tag{4.7}$$

It is important to note that degeneracy value co-relate strongly with amplitude reduction factor S_0^2. Due to this strong correlation, values of S_0^2 are estimated using bulk systems where degeneracy values are already known, and then assumed constant for a given phase while carrying out the fit of unknown samples so as to reduce the number of floating parameters in the fit.

b) The ***mean squared relative displacement*** $\boldsymbol{\sigma^2}$, is known as the Debye-Waller factor and its origin has been discussed in **above**. It is the variance of the path length given by the equation

$$\sigma^2 = \langle (r - \bar{r}^2)^2 \rangle \tag{4.8}$$

It is a measure of the disorder in the system and is used as a measure of deviation between the experimental and the theoretical structure. The typical values of σ^2should be less than 0.03 Å^2 and values greater than that signify that the theoretical model is incorrect or some of the paths are missing from the fit. Usually constraints are required to get reasonable values of σ^2 because the quality of fit increases for negative values of σ^2, which is not physically possible. Since there is a constraint on number of independent parameters that can be fitted, it is an interplay between the quality of the fit versus assuming some values of parameters to be constant in order to fit more number of variables. Therefore, in certain cases, it is reasonable to assume that similar paths have same value of σ^2 with minor deviations which may not affect the fit quality.

c) The ***amplitude reduction factor*** $\boldsymbol{S_0^2}$, has been discussed in detail in **above**. Based on the EXAFS equation, value of S_0^2 is independent of wavenumber and the path length. Since it

is outside the summation in equation (2.17), it is independent of paths used for the fitting, hence it is assumed to be constant for every scattering path for a given central atom in a fixed environment. The values of S_0^2 are considered reasonable[32] in the range of 0.65 to 1, and values outside this range suggest improper fit or incorrect selection of theoretical model. Also, as discussed earlier, since S_0^2 is highly dependent on degeneracy, its value cannot be extracted independently without knowing the value of N. Therefore, it is necessary to run bulk standards XAFS experiment before proceeding to the analysis of EXAFS data.

d) The ***path length*** $\boldsymbol{R_i}$, as defined in the previous section, is half of the average distance traversed by the photoelectron after being ejected from the central atom, getting scattered by one or more surrounding atoms and being absorbed back again at the similar central atom. It is usually specified as an average in order to consider thermal disorder as well as changing environments surrounding the central atoms due to concentration gradients or presence of defects such as grain boundaries, vacancies, etc. Deviation of less than 0.1 Å ($= |R_i - R_0|$) is usually considered reasonable otherwise some of the paths might be missing from the fit leading to high deviation.

e) The ***edge energy*** $\boldsymbol{E_0}$, is the energy required to excite core shell electrons of the central atom. However, it is not a fixed value and needs to be chosen carefully as discussed in **above**. The value of E_0 should always be in the sharp rising region of the μ(E) irrespective of the method selected to choose E_0. During fitting, shift in E_0 value from theoretical model is calculated which gives an estimate of the quality of the fit. A shift of up to 10 eV in

either direction is deemed acceptable. Value of E_0 is usually assumed to be constant for an edge. However, in certain cases where more than one phases are present, different E_0 value for each chemical oxidation state of the central atom can be used for fitting.

4.2.3 Fitting of EXAFS spectrum

After generating of the paths using theoretical FEFF models and having detailed knowledge of the fitting parameters, we are not ready to carry out the fitting of the EXAFS spectrum. After importing the FEFF calculation file of the theoretical model, the actual data set i.e. the output file of ATHENA containing the Fourier transformed χ spectrum is imported into ARTEMIS. Fitting of χ spectrum can be carried out in both k-space or the R-space. Each dataset has one or more paths associated with it with each path having 5 floating parameters: (a) S_0^2 also referred to as the amplitude, (b) degeneracy N, (c) shift in edge energy ΔE_0, (d) shift in path length ΔR, and (e) the mean squared displacement σ^2. Each of these parameters are assigned an initial value using the GDS window in ARTEMIS and are then fitted using the Levenberg-Marquardt algorithm. However, since each path requires 5 fitting parameters each, due to constraints on number of parameters that can be fitted, use of constraints and various strategies are required.

However, the first step of fitting is to choose the paths required to fit the χ spectrum. For this, fitting space and the fitting range needs to be defined. It is advantageous to fit in the R-space i.e. the χ(R) spectrum because of various factors discussed below. Firstly, each theoretical path shows a peak at a specific radial distance in the R-space. If this peak position coincides with the peak position of χ(R) spectrum of the sample, it is a good basis to assume that the particular path should be included in the fitting of the χ(R) spectrum of the sample. Secondly, plotting in R-space gives an indication of what the fitting range should be. For example, for the case of Fe bulk powder,

Figure 4.3 shows the χ spectrum plotted in R-space. The peaks are well defined in the range of 1.92 Å to 5.38 Å, therefore this was chosen as the range for the fitting of the spectrum. It should be noted that minimum value of the range should not be less than the Rbkg value defined earlier because the spectrum before Rbkg is not Fourier transformed and any peaks visible are associated with the noise of the data. Once the R-range is defined, the paths with peaks in that range are plotted along with the χ(R) spectrum of the data, as shown in **Figure 4.3**. Not all paths are shown in the figure for better visualization.

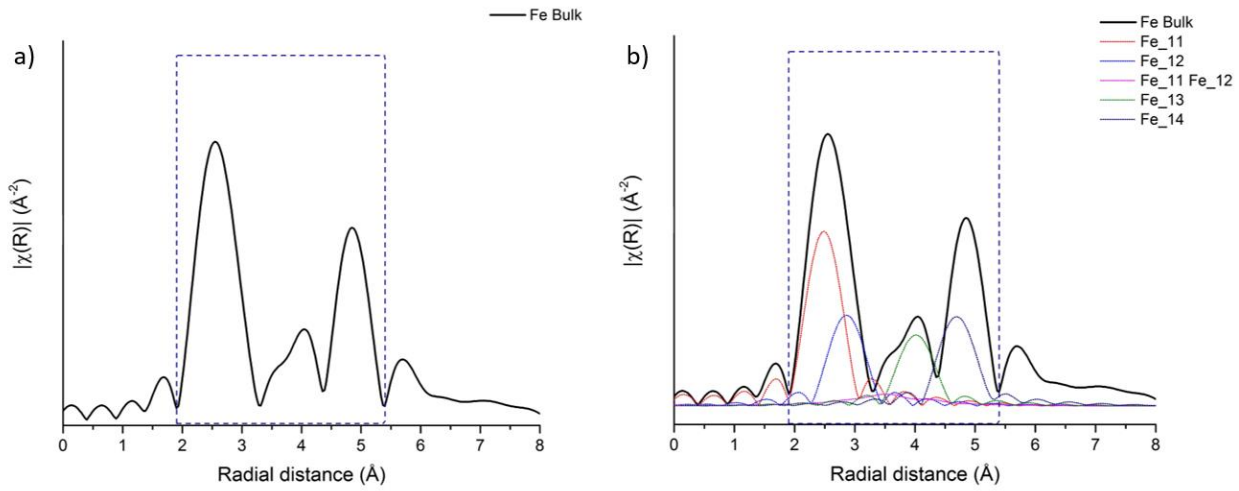

Figure 4.3. *(a) Plot shows the χ(R) spectrum of Fe bulk plotted in R-space plotted with a k-weight of 1. Fitting range is highlighted using blue dashed line. (b) Colored dotted lines shows the various theoretical paths generated using FEFF. Paths with peak positions coinciding with the χ(R) spectrum of sample are generally used for fitting.*

However, including all the paths with matching peak position with χ(R) spectrum does not necessarily increase the fit of the spectrum. Similarly, including paths without matching peak position may increase the quality of the fit. A bottom up strategy can be a good way to start with the fitting. This can be done by starting with the fitting on the 1st peak also referred to as the 1st shell using the nearest neighbor path, i.e. Fe_11 in the case of Fe bulk powder. After getting a good

fit of the first shell, the fitting R-range in increased to include the 2nd shell and fitting is carried out again. It is important to note that the fitting parameters of path used for fitting of the 1st shell should be allowed to float while carrying out the fit of the 2nd shell, and only in certain cases can be allowed to be fixed in order to bypass the constraints limit. The quality of the fit is defined using the R-factor as described using equation (4.3). Smaller the R-factor, less is the mismatch between the fitted model and the data. There is no fixed value of R-factor which defines a good fit, it is just used as a reference between different fits for comparison. There might always remain some mismatch of fit due to the noise present in data or due to an error in the model. Therefore, the fitting is an iterative process, where in each step a path is added or removed, its quality assessed and the process repeated again till the user is satisfied with the quality of the fit. However, R-factor is not the only criterion for evaluating the quality of the fit. The estimated values of fitting parameters should also be reasonable and in the vicinity of the values of the theoretical model so as to justify the selection of the theoretical model.

Figure 4.4 shows the fit of Fe bulk plotted in R-space with a k-weight of 1. Five paths were used for fitting of χ(R)in the R-range of 1.92 Å to 5.38 Å. K-range was defined during processing of data in ATHENA. **Table 4.3** shows the various parameters of EXAFS equation for Fe bulk. Values highlighted in red were estimated using fitting. R_{eff} was evaluated using FEFF calculations. Degeneracy in case of bulk standards are assumed to be constant for the concerned path because of the presence of long range structure of atoms. Hence, the value of S_0^2 is only useful information extracted from running bulk standards. This S_0^2 is now used as a fixed value during the fitting of NP sample where degeneracy is allowed to float.

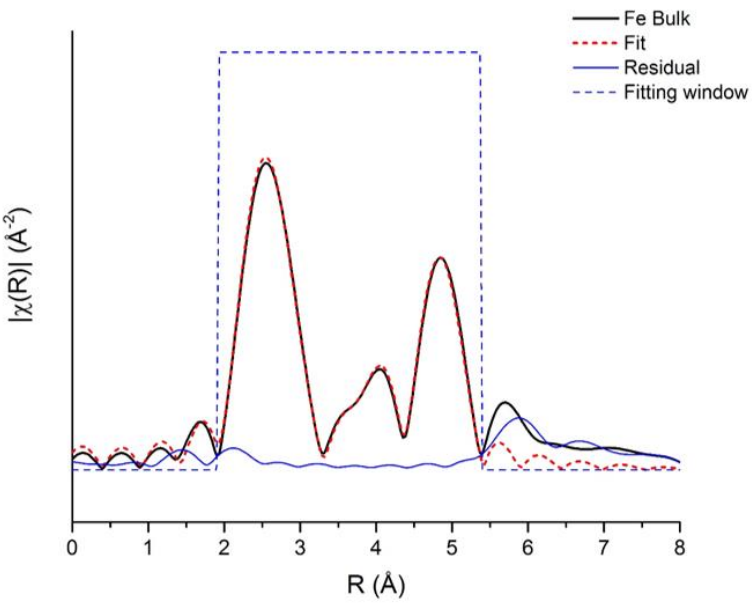

Figure 4.4. *Plot shows the fitting curves of χ(R) for Fe bulk standard.*

Fe Bulk	**EXAFS Parameters**							**Fitting range**	
Path	**N** (theoretical)	S_0^2	σ^2 (Å^2)	ΔE_0 (eV)	ΔR_0 (Å)	R_{eff} (Å)	$R = R_{eff} + \Delta R_0$ (Å)	**k-range** (Å^{-1})	**R-range** (Å)
[Fe] Fe1_1	8	0.588	0.00558	8.534	0.00608	2.4855	2.49158	3.95 to 9.84	1.92 to 5.38
[Fe] Fe1_2	6		0.00776		-0.03381	2.8700	2.83620		
[Fe] Fe1_1 Fe1_2	48		0.00101		0.00808	3.9205	3.92858		
[Fe] Fe1_3	12		0.01168		0.03968	4.0588	4.09847		
[Fe] Fe1_4	24		0.00377		0.02683	4.7594	4.78623		

Table 4.3. *Table shows the parameters of the EXAFS equation. Values highlighted in red were determined by fitting of χ(R).*

For example, suppose oxidized Fe nanoparticle sample contains a mixture of 3 phases: Fe, Fe_2O_3 and Fe_3O_4. Therefore, to begin with, bulk standards of Fe, Fe_2O_3 and Fe_3O_4 are used to extract S_0^2 value of each phase. Now these 3 S_0^2 values are used as constants during the fitting of oxidized NP sample corresponding to the path of the given phase used for fitting.

Typical values of EXAFS parameters are:

(a) ΔR should be less than 0.5 Å

(b) ΔE or E_0 should be less than 10 eV

(c) σ^2 should be less than 0.02 $Å^2$, and

(d) S_0^2 should be in the range 0.6 to 1.

Other techniques that can be included in the model to reduce number of independent parameters of fit include

(1) using symmetric term $\alpha \cdot R_{eff}$ for all paths where only α is varied rather than defining a new ΔR for each path;

(2) use of one E_0 value for all paths or 2 energy shifts, one for 1st shell and other for remaining shells;

(3) σ^2could be grouped for similar paths, having identical bonds, for example, for Fe_11 and Fe_12 paths

(4) using one S_0^2 for all paths for a given phase

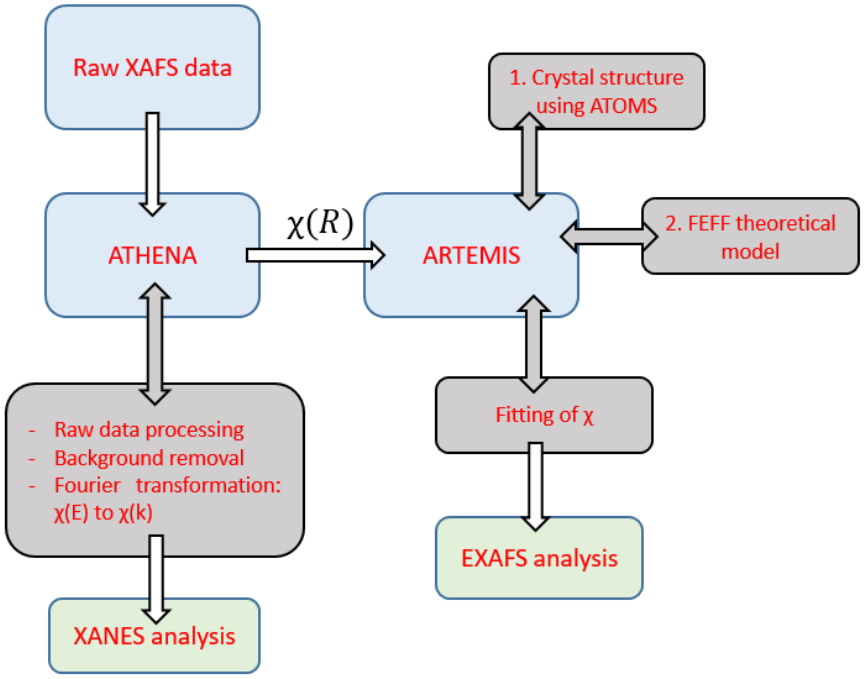

Figure 4.5. *Flowchart summarizes the steps from handling of raw data to getting results using XANES and EXAFS analysis*

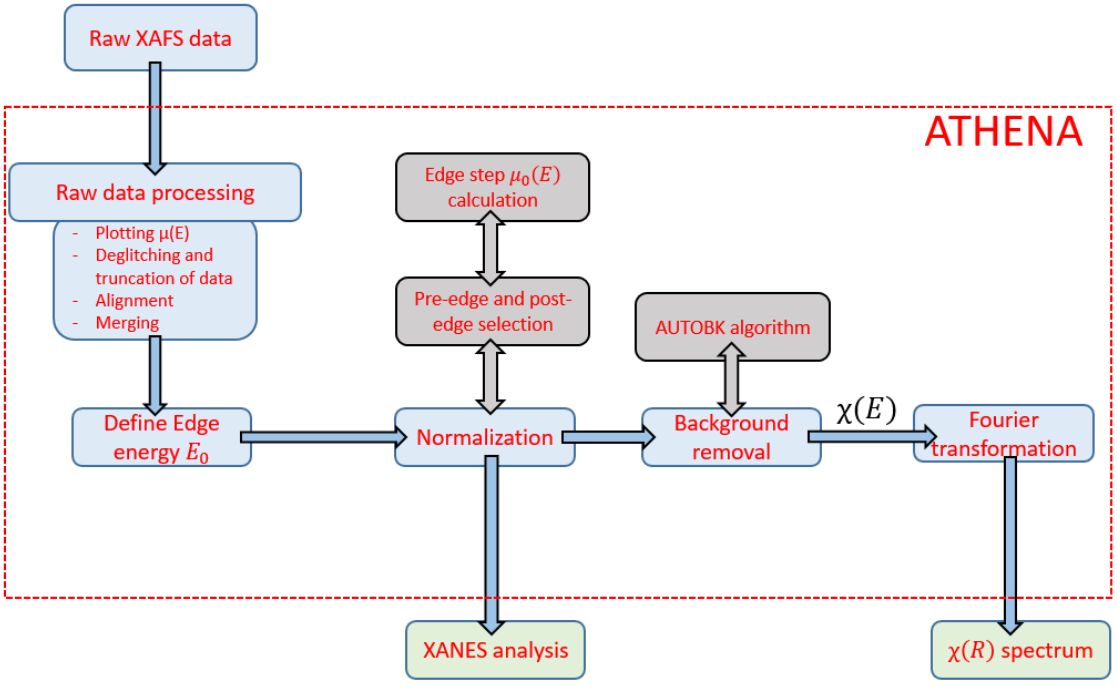

Figure 4.6. *Flowchart summarizes the processing of XAFS data in ATHENA for XANES analysis and for extraction of χ(k) spectrum*

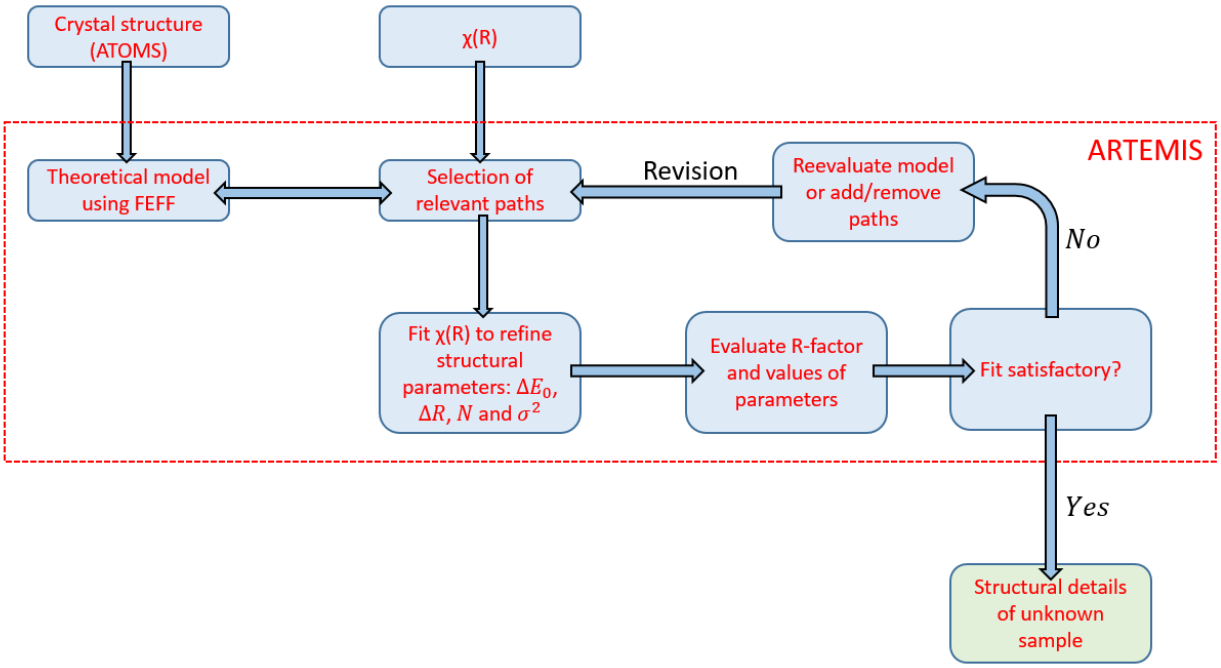

Figure 4.7. *Flowchart summarizes the processing of χ(k) spectrum in ARTEMIS to extract structural parameters of an unknown sample*

The fitting parameters also have a k-dependence. Different k-weights emphasize different regions of the spectrum. For example, fitting with a k-weight of 1 emphasizes low k region of the spectrum whereas k-weight of 3 lays more emphasis on the high k region during evaluation of the parameters. The dependence of fitting parameters on k is as follows:

(a) $\Delta R \propto k$

(b) $\Delta E \propto \frac{1}{k}$

(c) $\sigma^2 \propto k^2$

(d) S_0^2 is independent of k

Therefore, fitting was carried out using multiple k-weights of 1, 2 and 3 simultaneously in order to distribute the sensitivity of fitting parameters over the entire fitting k-range.

4.3 Example of XAFS data analysis

The following section will discuss the step by step data analysis of Fe NPs oxidized in air at 200 ^{0}C for 60 minutes. 10 scans of oxidized Fe NPs were carried out, and the data for Fe K-edge for both fluorescence mode and transmitted mode along with the reference data was collected during the experiment. However, only fluorescence and reference data was used for further analysis. Iron metal foil was used as reference and energy was scanned from 7050 eV to 7548 eV.

4.3.1 ATHENA

The raw files of the 10 scans are imported simultaneously into ATHENA. During import of data, a window opens in which the numerator and denominator columns can be selected both for μ(E) of sample as well as μ(E) of reference. For μ(E) of sample, numerator is selected as the sum of the 4 vortex detectors and denominator as the I_0 column. For μ(E) of reference, numerator is selected as I_t and denominator as I_f along with the natural log function. For similar columns in all 10 raw files, ATHENA by default selects the columns and imports the raw files.

After importing the 10 raw files, ATHENA computed two μ(E) plots for each scan – sample and reference. Now the data is ready for processing. First step is the visual observation of each scan plot. If the plot is too noisy or looks quite different from other scan plots, then it should be discarded or its importance decreased. For this case study, all scans looked good and where given the default importance value of 1. Next, alignment of the reference channels was carried out. For this, reference of 1st scan is selected as the standard and all other reference channels are aligned to it with the fit plotted as smoothed derivative of energy. After alignment, the scans were merged as μ(E) into a single scan file after which individual scan data could be discarded.

Next data deglitching and truncation is carried out. The merged μ(E) plot was observed carefully for any sharp localized spikes and were then removed. Truncation of data was carried out so as to remove the redundant energy ranges. For this case, data beyond the energy range of 7540 eV was truncated. Next, selection of edge energy E_0 also referred to as energy calibration is carried out. The merged μ(E) second derivate was plotted and x-axis corresponding to zero crossing or y = 0 point was selected as the E_0 value. The default value of E_0 calculated by ATHENA changed from 7127 eV to 7126.70 eV after energy calibration.

Next, parameters for normalization and background are selected. ATHENA by default estimates the values of these parameters which may need corrections in certain cases. The Rbkg, pre-edge range and normalization range default values fit well with the μ(E) plot and are not altered. However, the k-weight is changed to 1 and normalization order is changed to 2 for better spline selection. Edge step is calculated automatically by ATHENA. The data processing carried out till now is sufficient for XANES analysis.

Based on knowledge from other characterization techniques, 3 different phases of iron: Fe, Fe_2O_3 and Fe_3O_4 were hypothesized to be present in the oxidized Fe NP sample. Therefore, XAFS data was also collected for these standards. Data of these standards can also be imported from available online libraries. For XANES analysis, μ(E) spectrum of bulk powder standards were imported into ATHENA. The raw data of these standards was processed similarly as discussed above. Linear combination fitting of these standards was carried out to fit the normalized μ(E) spectrum of the sample. The fit range was selected to be -20 eV to 30 eV with respect to the edge energy. The edge energies of the standards were allowed to float during the fitting to compensate for any error of monochromator during the experiment. The fit was fairly accurate with a very low R-factor of 1.68×10^{-3}. The fit results are shown in **Table 4.4** and **Figure 4.1**.

Standard	Weight	ΔE_0 (eV)
Fe bulk	0	0
Fe_2O_3 bulk	0.618 ± 0.115	2.571 ± 0.337
Fe_3O_4 bulk	0.382 ± 0.115	2.652 ± 0.588

Table 4.4. *Table shows the parameters of oxidized Fe NP sample extracted using XANES fitting*

XANES fitting shows that the oxidized Fe NPs sample consists of phases Fe_2O_3 and Fe_3O_4 in the ratio 0.618:0.382 and absence of pure Fe phase. The shift of edge energies of standards to fit the data is ~ 2.5 eV which is considered reasonable. Besides fitting of μ(E) spectra for XANES analysis, ATHENA also provides the option of choosing fitting space as derivative of μ(E) or χ(k).

To carry out EXAFS analysis, χ(k) spectrum needs to be extracted from χ(E). Therefore, Fourier transformation (FT) is carried out next. ATHENA by default selects the parameters for FT. K-range was selected as 2.57 $Å^{-1}$ to 8.14 $Å^{-1}$ based on the technique discussed earlier in **above**. After Fourier transformation, the ATHENA file is saved which be imported directly into ARTEMIS for further analysis.

4.3.2 ARTEMIS

The ATHENA file containing χ(k) spectrum is now imported into ARTEMIS. Based on XANES analysis, the oxidized Fe NPs consists of only 2 phases: Fe_2O_3 and Fe_3O_4. Therefore, path of both these phases were used for fitting. The theoretical structural data of these phases was imported into ARTEMIS in the form of CIF file from *ICSD database*[33] or as .inp file from *The Atoms Archive*[34]. Next FEFF calculations was carried out in ARTEMIS to generate the theoretical model for the 2

oxidized phases of iron. Each FEEF output files consist of the information of paths including its degeneracy N, path length R_{eff} and scattering path type.

The next important step is to select what paths need to be included in the fit. Simultaneously, some of the input parameters need to be optimized. The fitting k-weights are selected as 1, 2 and 3; and the fitting space as R-space. The plotting k-weight of spectrum is selected as 1 for better visualization of fit at lower R values after fitting has been done. The plotting k-weight does not affect the fitting in any way. Rest default values are used for fitting. It is important to note that the plots are plotted with phase correction with one of the paths as reference as it is helpful in selecting the correct fitting R-range. Discussed below is the example for fitting of the 1st shell of the χ(R) spectrum of the oxidized Fe NPs sample, which can be further extrapolated for fitting of the other shells.

To select the paths, initially the R-range is selected to include only the 1st shell of χ(R) spectrum i.e. 1 Å to 2.56 Å. While selecting the fitting R-range, ARTEMIS shows how many independent variables can be fitted, therefore it is important to select only relevant paths since each path has multiple variables that require fitting. Also, to begin with, only direct scattering paths are selected for fitting and later if required, multiple scattering paths can be included. [Fe_2O_3] O_11, [Fe_2O_3] O_12 and [Fe_3O_4] O_11 with R_{eff} as 1.946 Å, 2.116 Å and 1.886 Å respectively, are the only direct paths with R_{eff} in the given R-range. Therefore, these paths are selected and plotted along with the χ(R) spectrum, similar to as shown in **Figure 4.3** but for different sample. The peak position of path [Fe_2O_3] O_12 does not match with the peak of χ(R) spectrum and is therefore not included in the 1st fitting attempt. The variables are now defined for the selected paths in the GDS window. Amplitude reduction factor for Fe_2O_3 and Fe_3O_4 was calculated using bulk standards and therefore are used as constants. Their values were calculated as 0.864 and 0.726 respectively. Energy shift

is constant for all paths, therefore only 1 variable is defined with the name delE. Shift in path length ΔR, N and σ^2 variables were defined independently for both paths. Therefore, in total there are 7 variables: delE, delR1, delR2, n1, n2, ss1 and ss2. Since these paths are from different phases, no correlations can be used between the variables to reduce the number of independent parameters. Fitting is carried out using Levenberg-Marquardt algorithm, which requires an initial value of variables. Therefore, the variables are given an initial value of 0 eV for delE, 0 Å for $delR_i$, respective path degeneracy value for n_i and 0.003 $Å^2$ for ss_i. Path with smallest R_{eff}, i.e. closest to central atom is selected as reference for phase correction, $[Fe_3O_4]$ O_11 in this case.

After multiple fitting attempts, when the fitting of 1st shell looks good with reasonable values of R-factor and other parameters, the fitting R-range is increased to include the 2nd shell of $\chi(R)$ spectrum of the sample. The fitting process requires multiple iterations and is repeated by changing the paths or correlating the variables or tweaking the R-range or the k-range till fitting of desired shells are achieved. For example, on including the 2nd shell in fitting range, the paths corresponding to the 1st shell may require some changes, or even an addition or removal of a path. Fitting is an exhaustive process with no defined target, therefore is carried out till the final model looks similar to the model predicted based on information from other characterization techniques. For example, before starting the fit, X-ray diffraction analysis can be used as a basis of selecting what phases to include for fitting.

200C@60mins	Parameters								Fitting range	
Path	S_0^2	N (theoretical)	N (experimental)	σ^2 (Å^2)	E_0 (eV)	ΔR (Å)	R_{eff} (Å)	R (Å)	k-range (Å^{-1})	R-range (Å)
[Fe2O3] O1_1	0.864	3	5.607	0.01140	-0.945	0.06265	1.9457	2.00834	2.57 to 8.14	1.00 to 4.00
[Fe2O3] Fe1_1	0.864	1	4.234	0.01140	-0.945	0.09338	2.9004	2.99378		
[Fe3O4] O1_1	0.726	4	1.091	0.00129	9.998	-0.01257	1.8861	1.87354		
[Fe3O4] Fe1_1	0.726	4	1.385	0.00129	9.998	-0.02422	3.6355	3.61128		

Table 4.5. *Table shows the parameters of the sample evaluated by fitting of the χ(R) spectra.*

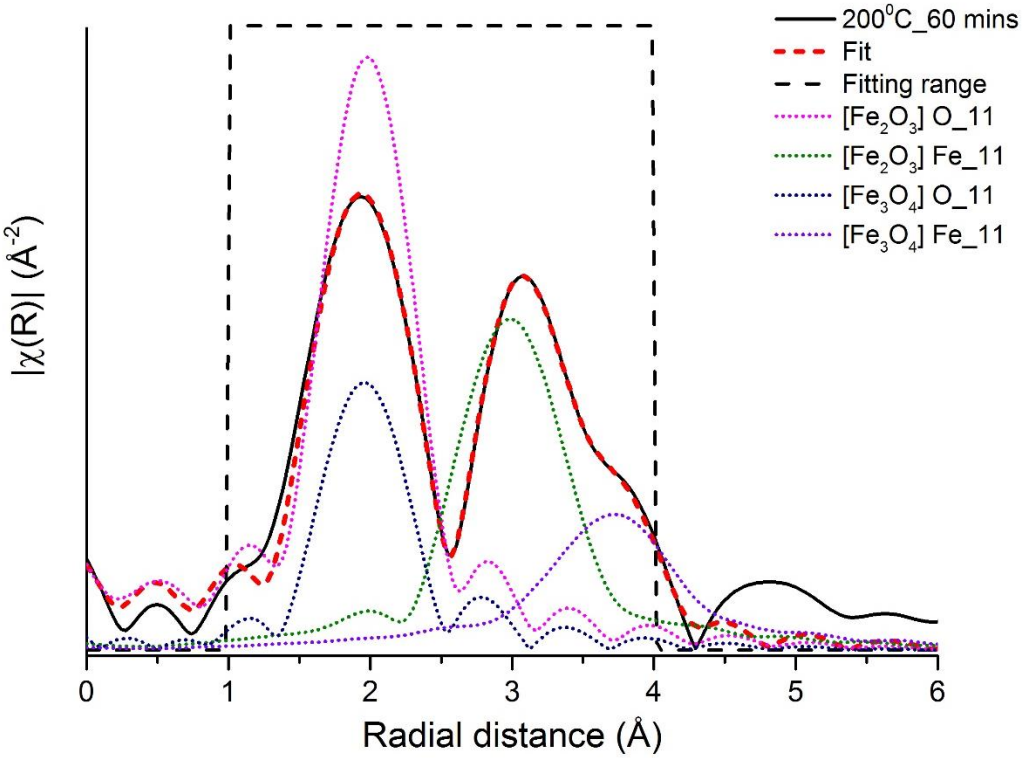

Figure 4.8. *Plot shows the fit of the oxidized Fe NPs sample. Dotted line shows the contribution from each path to the χ(R) spectrum of the sample.*

The fitting results for Fe NPs oxidized in air at 200 ^{0}C for 60 mins are shown in **Table 4.5** and **Figure 4.8**. The final fit consisted of 4 different paths, 2 each from both the phases. The results have been discussed in detail in the next chapter.

Chapter 5. X-ray absorption spectroscopy study of oxidation of Iron nanoparticles in air

5.1 Introduction

A lot of effort has been made recently to control the shape, size and composition of NPs in order to tune their properties. However, it is not all possible to achieve this control through direct synthesis. Chemical transformations, for example through cation or anion exchange or even oxidation provides an alternate route to manipulate the structural phases and properties.[35,36] However, the reactions mechanisms and structural changes taking place during these chemical transformations are not fully understood and getting an insight into the mechanisms involved could be useful to tailor the properties of the nanomaterials. Therefore, for more insight into the underlying mechanisms and reaction kinetics, to begin with, a simple NP system of iron-iron oxide was selected to study the chemical transformations in nanomaterials.

Iron and iron-oxide nanoparticles (NPs) are one of the most explored materials due to its vast range of applications in fields such as ferro-fluids[1], magnetic imaging resonance (MRI)[2], catalysts for hydrogenation reactions.[23,24] Additional advantage of iron based materials is its large scale availability in nature and its cost-effectiveness. Besides this, these NPs are relatively less toxic as compared to other nanomaterials, paving its way for further applications in future. However, the as synthesized Fe nanoparticles have high affinity for oxygen, and when exposed to atmospheric conditions, oxidize completely or partially on the surface to form core-shell type structure[5,6] or hollow structures[7,8] in certain cases due to Kirkendall effect. Formation of hollow core due to coalescence of vacancies at octahedral sites leads to generation of nanomaterials with defects which has generated a lot of interest in energy storage as well.[3,4]

High temperature growth of oxide shell is well understood based on extensive theoretical as well as experimental work.[9] However, less is known about the local structure of the iron oxide shell. The oxide shell is considered to be composed of maghemite ($\gamma - Fe_2O_3$) and magnetite (Fe_3O_4). Both these phases form inverse spinel structure with similar lattice constants and is therefore difficult to differentiate using conventional characterization techniques such as x-ray diffraction due to the absence of long-range order in the nanoparticles. γ-Fe_2O_3 and Fe_3O_4 phases have significantly different properties; for example, due to electron hopping between Fe^{+2} and Fe^{+3} at octahedral sites, the electrical conductivity of Fe_3O_4 is much higher as compared to γ-Fe_2O_3. Therefore, it is important to study the evolution of different oxides of iron with time under different conditions to understand the underlying mechanisms which could be useful in tailoring the electrical and magnetic properties of a material.

The initial oxidation of the as-synthesized Fe NPs when exposed to air can be explained based on the following theory:[37] the oxygen atoms attach onto the surface of the metal NPs and form a thin layer of metal oxide. The electrons then tunnel from the Fe metal towards the outer surface passing through the iron oxide layer. This leads to generation of electric field which drives the outward diffusion of the ionized Fe atom towards the outer surface.[38] However, without external stimuli, at room temperature, 1 nm to 2 nm thick oxide layer is formed instantaneously and further growth is limited over long time period[39,40] because of the limitation of the ion transport and electron tunneling with increasing oxide shell thickness. Therefore, for further oxidation, high temperatures are required for electron transport by thermionic emission which decreases at a slower rate as compared to electron tunneling with increasing oxide shell thickness.[41]s As the NPs are further oxidized at high temperatures, the mechanism can be explained based on the Kirkendall effect.[42] The iron cations diffuse faster than the oxygen anions, consequently leading to formation of voids

at the interface of the metal and oxide layer. For small particle size, complete oxidation of Fe core takes place, and the voids coalescence to form a hollow core with an oxide layer on the outside. Particle size greater than ~8 nm have been reported to have incomplete oxidation with Fe metal left at the core, with the presence of vacancies at the intersection of the metal and oxide layer.[38]

Due to its high sensitivity to short-range order, x-ray absorption spectroscopy (XAS) is an ideal technique for the structural study of the transformation of NPs with oxidation. Therefore, in this study, XAS measurements were carried out at Fe K-edge for as synthesized Fe NPs of sizes ~ 10 nm and particles oxidized at 200 °C and 250 °C for up to 3 hours.

5.2 Experimental

Iron pentacarbonyl (99.9%), octadecene (90%) and tri-octylamine (98%) were purchased from Sigma-Aldrich and were used for the synthesis of the iron nanoparticles. Ethanol (≥ 99%) was purchased from BDH chemicals. All synthesis was carried out using standard Schlenk line setup and glove-box technique, under a nitrogen atmosphere at atmospheric pressure.

The synthesis was carried out by thermal decomposition of iron pentacarbonyl dissolved in organic medium in presence of surfactants.[43] The precursor solution was prepared in glove box by mixing 0.4 ml of iron pentacarbonyl and 2 ml of octadecene (ODE). A mixture of 0.38 mmol tri-octylamine and 10 ml ODE were heated to 60 °C in a 25 ml 3-neck flask and kept under vacuum for 1 hour. While keeping the solution under nitrogen gas, the temperature was increased to 200 °C. The precursor solution was then rapidly injected into the flask under vigorous stirring and allowed to react for 20 mins. To oxidize the Fe NPs, the solution temperature was set to the required temperature (200 °C and 250 °C) and 25 ml/min oxygen mixture in nitrogen was bubbled through the solution for up to 3 hours. The solution was then cooled to room temperature and the

NPs were precipitated by adding ethanol and isolated by centrifugation. The precipitates were then stored in glove box until further characterization.

Scintag Theta-Theta diffractometer (Cu K_α radiation) was used to record the x-ray diffraction (XRD) data.

Transmission electron microscopy (TEM) images were recorded on an FEI Tecnai T12 TEM operating at 120 kV.

Further structural characterization was carried out using x-ray absorption spectroscopy (XAS). The XAS spectra was obtained at F3 beamline of the Cornell High Energy Synchrotron Source (CHESS) at Cornell University. Measurements for Fe K-edge were performed under fluorescence mode for the analysis of the samples. The fluorescent x-ray yield was recorded using a Hitachi 4-element Si vortex detector. The data was also collected under transmission mode using ionized gas chamber to monitor the x-ray intensities. Additional ionization chamber was used with an iron foil standard to assist in alignment of the edge positions. The samples were prepared by spreading and sandwiching the solid NPs between Kapton tapes. The bulk standards maghemite and magnetite, were prepared by dilution with boron nitride followed by pressing the powders to form pellets. All x-ray absorption near edge spectroscopy (XANES) and extended x-ray absorption fine structure (EXAFS) analysis was carried out using the IFEFFIT package.[28] The raw data was processed using ATHENA which involved edge determination, background subtraction using AUTOBK algorithm, alignment and merge of scans, and the normalization of the absorption coefficient plot. Linear combination fitting was carried out to calculate the phase contribution of different phases present in the sample. The spectra were then Fourier transformed to R-space and fitting of the data was carried out in ARTEMIS to extract the structural parameters of the samples.

5.3 Results and Discussion

Fe NPs synthesized by thermal decomposition of iron pentacarbonyl oxidize immediately after synthesis and form a thin iron-oxide shell. The evolution of morphology during oxidation of Fe NPs at 200 °C was characterized by TEM. **Figure 5.1a** shows the as-synthesized particles which are spherical in shape with a core/shell type structure. The average particle size of Fe NPs is 10.42 ± 2.09 nm. On bubbling O_2/N_2 mix through the solution containing Fe NPs, the particles get oxidized immediately, and show a hollow core while maintaining the overall spherical shape of the particles (shown in **Figure 5.1b-f**). It is interesting to note that the NPs get completely oxidized in a time frame of 2 minutes even at a small oxygen flow rate of 25 ml/min. Previous studies[38,43,44] show that for similar sized Fe NPs, it may take considerable amount of time to completely oxidize the Fe core present in as-synthesized particles, and in certain cases, incomplete oxidation taking place with Fe left behind in the core. Further work in progress to understand how the oxidation conditions may affect the extent of oxidation of Fe NPs. After 3 hours of oxidation, the particles maintain its hollow morphology but are larger in size with outer diameter 16.42 ± 2.40 nm.

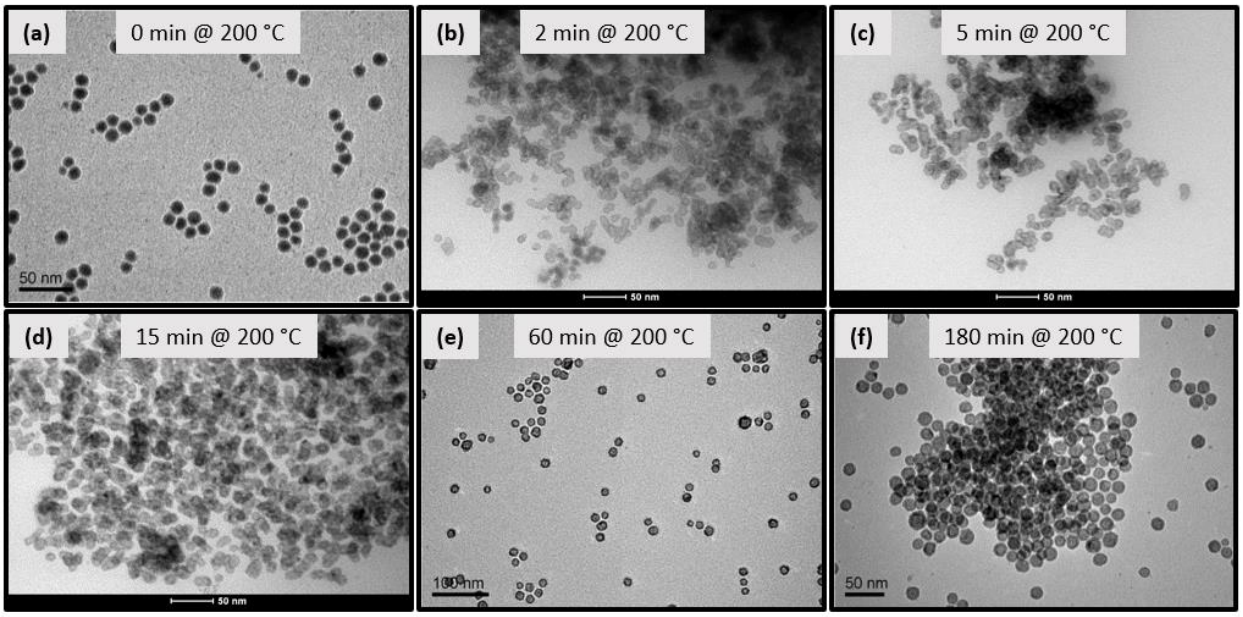

Figure 5.1. *(a) TEM image of as synthesized Fe NPs show a thin shell formation of iron oxide shell. (b-f) oxidized Fe NPs show hollow core/iron oxide shell*

Figure 5.2 shows the x-ray diffraction plot of Fe NPs oxidized in air at 200 °C up to 3 hours. The as-synthesized particles are highly amorphous and show very broad peaks. As the particles get oxidized, sharp peak starts to appear at ~ 35.5° and 62.5° corresponding to Magnetite (PDF#00-019-0629) and Maghemite (PDF#00-039-1346) phase and increases in intensity with time due to increasing crystallinity of the particles. A broad peak centered around bars of magnetite/maghemite at ~ 43° is present throughout even after oxidation for extended period of time. Therefore, it is difficult to exclude the presence of α-Fe and Wustite phase in the oxidized particles. To confirm the phases present, selected area diffraction pattern (SAED) of the samples obtained during TEM was converted to diffraction plots shown in **Figure 5.3**. Peak centered at 43° correspond to magnetite/maghemite phase with Wustite (PDF#01-073-2143) and Fe (PDF#00-006-0696) bars on the left and right respectively. Missing peak at 65° and 82.5° confirm the absence of Fe phase in the oxidized samples. Additionally, to further confirm the presence of only magnetite and maghemite phases in oxidized samples, peak intensity ratio of 2 min sample was

compared to that of standards (plotted separately in **Figure 5.3**b for better visualization). For peaks labeled 1, 2 and 3; peak intensity ratio is 1:0.30:0.49 which are similar to magnetite (1:0.2:0.4) and maghemite (1:0.16:0.34) standards.

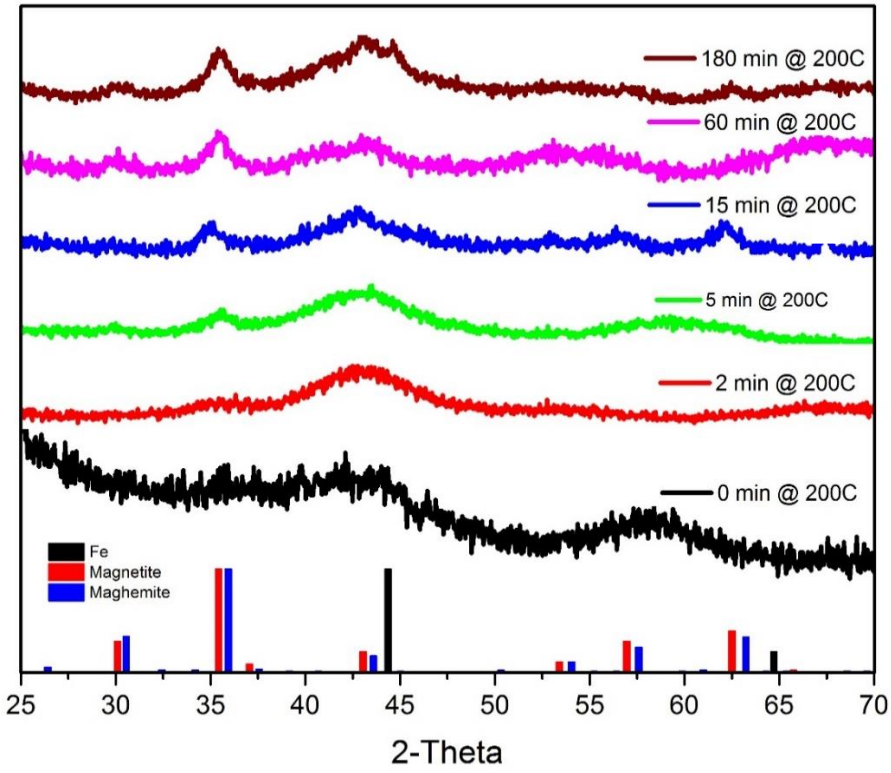

Figure 5.2. *Plot shows x-ray diffraction patterns of Fe NPS oxidized at 200 °C. Bar pattern shows standards used for reference.*

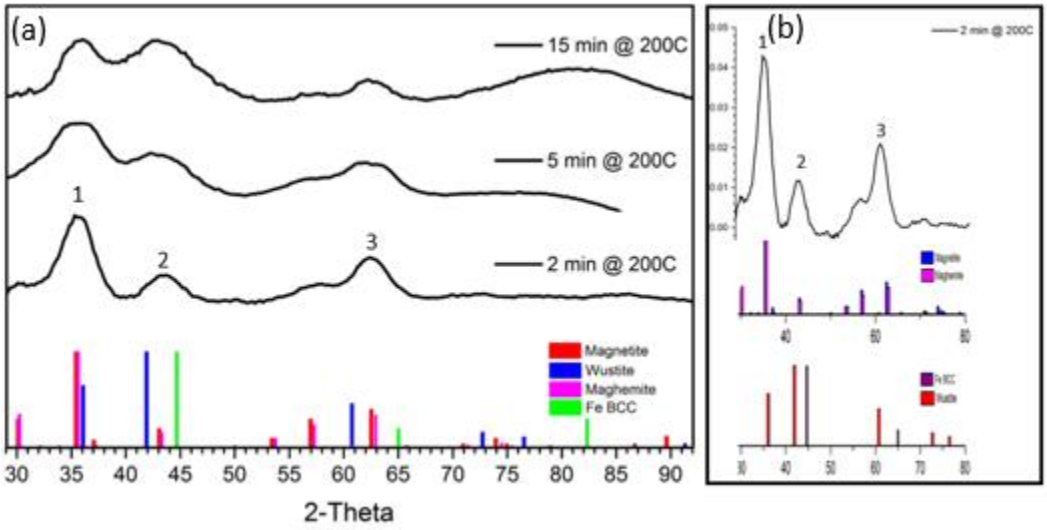

Figure 5.3. *(a) Plot shows XRD pattern obtained from selected area diffraction pattern obtained using TEM. (b) Plot shows zoomed out pattern for 2 min sample. Peaks marked 1, 2 and 3 are in the ratio 1:0.30:0.49 confirming the absence of Fe and wustite phase in oxidized particles.*

Fe K-edge XANES measurement were carried out to study the phase contribution in each sample. **Figure 5.4** shows the normalized absorption spectra of (a) standards Fe, Fe_3O_4 and γ-Fe_2O_3; (b) Fe NPs oxidized at 200 °C; and (c) Fe NPs oxidized at 250 °C. The pre-edge in the samples at ~ 7113 eV correspond to the dipole forbidden 1s to 3d transition of electrons. The edge energies of the samples are in the range of 7124 eV to 7126 eV, greater than the edge energy of Fe(0) metal and Fe_3O_4 but smaller than the edge energy of γ-Fe_2O_3, confirming the presence of mixed phases in all of the samples. However, no particular trend in the value of edge energy is observed as generally seen during change in oxidation state. **Figure 5.s1** shows the trend of edge energies of 200 °C and 250 °C oxidized samples with the bulk standards used as the reference. The oscillatory structure of NPs in absorption spectra is more damped as compared to bulk standards implying lack of long range crystalline order. Similarly, 0 min samples have more damped spectra due to amorphous structure, and as the particles are oxidized, increase in crystallinity is observed. No change in spectra is observed in 2 min onwards samples implying no change in structure taking place.

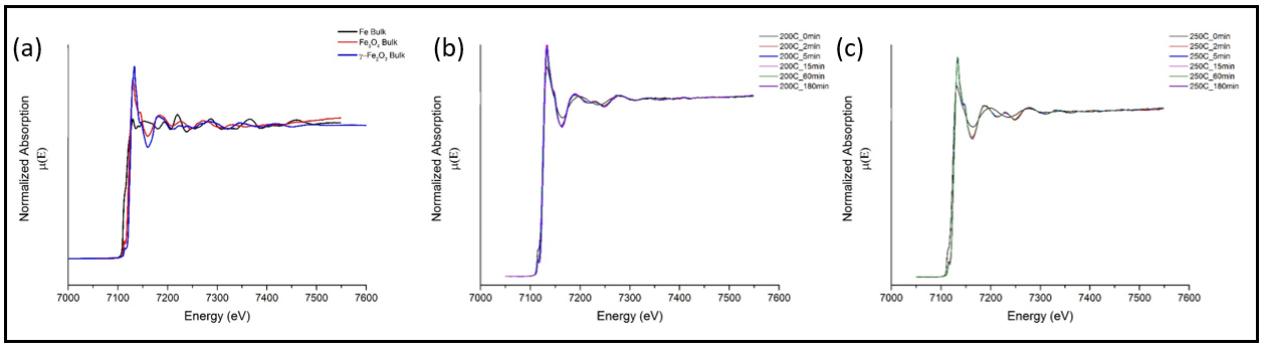

Figure 5.4. *Fe K-edge absorption edge spectra of (a) bulk standards, (b) Fe NPs oxidized at 200 °C, and (c) Fe NPs oxidized at 250 °C.*

Linear combination fitting (LCF) was carried out using the 3 standards. However, due to presence of mixed oxidation state in Fe_3O_4, it was not possible to calculate the individual contribution of Fe(II) and Fe(III) in each sample. The results of LCF are shown in **Figure 5.5**. The 0 min samples consist of all 3 phases with molar fraction of α-Fe phase equal to ~ 0.35 which is present in the core of the particles and the shell consisting of both Fe_3O_4 and γ-Fe_2O_3 in the ratio 0.55:0.10. Therefore, the majority phase present in the shell is Fe_3O_4. As the particles are oxidized, the contribution from α-Fe phase goes to 0, consistent with the TEM images which showed hollow cores. From 0 min to 2 min, there is a sharp increase in both Fe_3O_4 and γ-Fe_2O_3 because of the oxidation of Fe present in the core. However, with further oxidation, there is a small decrease in the contribution of Fe_3O_4 phase because of conversion of Fe_3O_4 to γ-Fe_2O_3 phase which becomes negligible 15 min onwards. The Fe_3O_4 forms an inverse spinel structure, with Fe(II) occupying 8/16 octahedral sites; and Fe(III) occupying 8/8 out tetrahedral sites and the remaining 8/16 octahedral sites. Therefore, Fe_3O_4 can be written as $(Fe^{+3})[Fe^{+2}Fe^{+3}]O_4$, with ( ) representing the tetrahedral sites and [ ] representing the octahedral sites. As oxidation takes place, Fe(II) at octahedral sites convert to Fe(III), leading to formation of vacancy at octahedral sites to compensate for the charge, forming the cation deficient γ-Fe_2O_3 phase which can also be written as $(Fe^{+3})[Fe^{+3}_{5/3}\square^{0}_{1/3}]O_4$, where □ represents the location of the vacancies. Conversion of Fe_3O_4 to γ-Fe_2O_3 phase is higher in case of higher oxidation temperature because of the increased diffusivity of the cations. After oxidation over extended period of times show that the molar ratio of magnetite to maghemite is similar for both the set of samples.

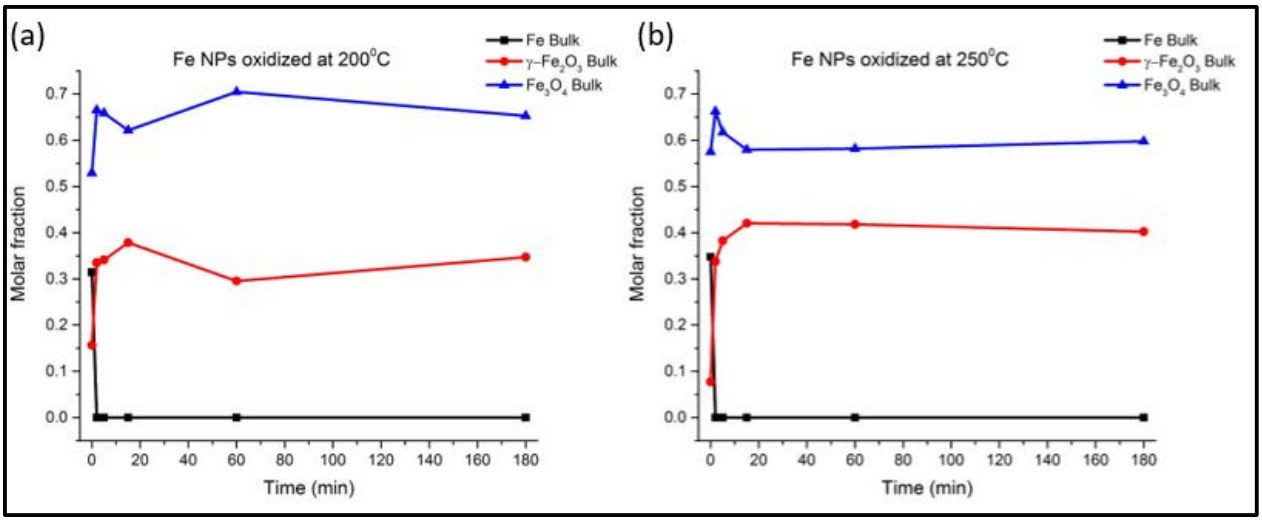

Figure 5.5. *Plot shows molar fraction of phases obtained using Linear combination fitting for samples oxidized at (a) 200 °C and (b) 250 °C.*

Background removal was carried out from the absorption coefficient spectra and the obtained spectra was Fourier transformed and plotted in R-space. **Figure 5.6** shows the Fourier transformed plots for NPs oxidized at 200 °C and 250 °C. The 1st peak for the oxidized particles in the R-plot correspond to Fe-O scattering path, the 2nd peak and the 3rd peak to Fe-Fe[octahedral] and Fe-Fe[tetrahedral] scattering paths respectively. Absence of long range order is due to the lack of crystallinity and small size of the particles. R-plot pattern of 2 min onwards samples look similar to the bulk oxide phases, however it is not possible to distinguish individual phase contributions based on visual observations. The 0 min sample looks remarkably different from other plots with the 1st peak being broader and shifted slightly to the right, and the 2nd peak quite depressed. This confirms that the 0 min samples have different structures from oxidized samples. As the particles get oxidized, no changes in pattern are observed, however slight variations in peak intensity and peak positions are observed due to interconversion between different oxide phases. Due to presence of vacancies at octahedral sites in bulk γ-Fe_2O_3, the 2nd peak corresponding to Fe-Fe[oct] path is slightly depressed as compared to that of bulk Fe_3O_4. However, when comparing R-plots

of samples oxidized at different temperatures, as shown in **Figure 5.6c**, both peaks for 250 °C samples show higher intensity, which might be because of the greater extent of crystallization. Therefore, fitting of the R-plots was carried out to obtain more structural details of the particles and study the effect of oxidation temperatures.

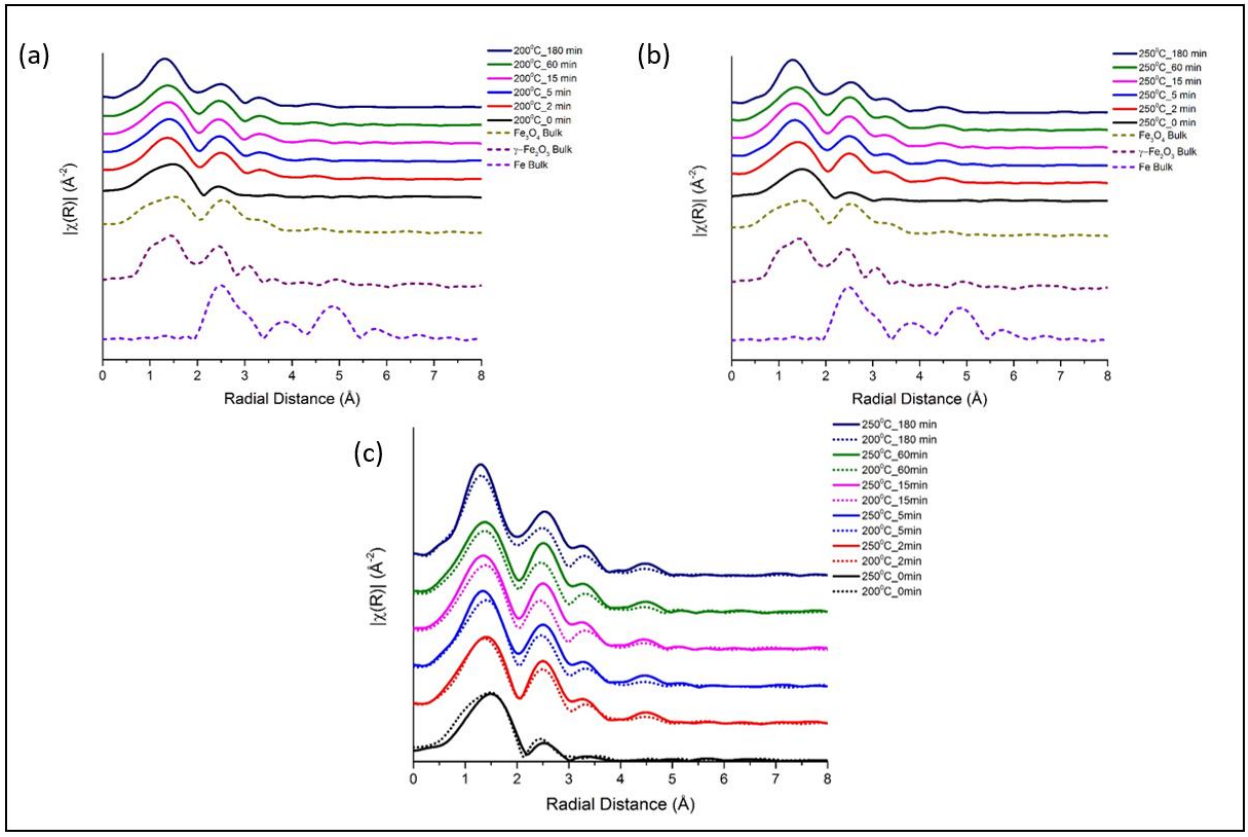

Figure 5.6. *Plot shows the Fourier transformed spectra plotted in R-space for NPs oxidized at (a) 200 °C and (b) 250 °C. Dashed line represents the R-plots of bulk standards used for comparison and calculation of amplitude reduction factors S_0^2. K-weight of 1 was used for all the plots. (c) Plot shows the comparison of peak intensity for particles oxidized at 200 °C (solid line) and 250 °C (dotted line). K-weight of 1 was used for all plots.*

The fitting of the R-plots was carried out in the range of 1.0 Å to 4.0 Å. For Fourier transformation of spectra to obtain R-plots, k-space range was selected as the nearest nodes to $(2.53\ \text{Å}^{-1}, 8.165\ \text{Å}^{-1})$. The fitting was carried out in R-space with simultaneous fitting at k-weights of 1, 2 and 3. Fitting of the 3 bulk standards was carried out to obtain the amplitude reduction factors which were then used as constants to obtain co-ordination number of different

phases. The fitting was carried out using only direct scattering paths with the assumption of negligible contributions from multiple scattering paths. 4 different paths were used for the fitting of spectra of oxidized samples, (1) [Fe_3O_4] O11 and (2) [γ-Fe_2O_3] O11, i.e. scattering between central Fe atom and nearest O atom from Fe_3O_4 and γ-Fe_2O_3 phase respectively; (3) [Fe_3O_4] Fe-oct and (4) [γ-Fe_2O_3] Fe-oct, i.e. scattering between central Fe atom and Fe atoms present at octahedral locations. Since no change takes place at tetrahedral locations, fitting of 3rd peak was excluded from the fittings. An additional path [α-Fe] Fe11 besides the above mentioned paths was used for the fitting of the as-synthesized 0 min sample to take into consideration the presence of α-Fe phase in the core. Since each of the particles consist of multiple phases, relative weight of phases obtained from XANES analysis was taken into consideration to obtain the coordination number (CN), also referred to as the degeneracy of the paths. The theoretical degeneracy of the 5 paths are 8, 4, 6, 12 and 6 respectively.

Figure 5.7 shows the degeneracy of Fe paths obtained from fitting of the R-plots. The solid and dotted lines represent the degeneracy of samples oxidized at 200 °C and 250 °C respectively. In **Figure 5.7a**, degeneracy of α-Fe phase goes to 0 which is consistent with the XANES observation that no α-Fe phase is present in the oxidized samples. The degeneracy values of [α-Fe] Fe11 are ~ 1.2 as compared to the theoretical value of 8 which is consistent if we consider that the molar fraction of Fe in the 0 min sample is 0.35. Further reduction in values is due to the presence of amorphous structure in the un-oxidized particles as observed in the XRD plot. It is important to note that the degeneracy values obtained from fit may be in error by ± 10%, therefore minor

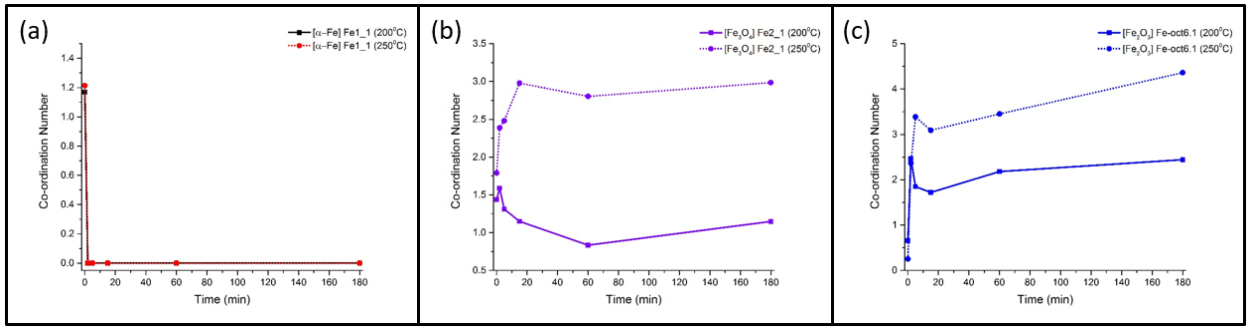

Figure 5.7. *Coordination number of paths (a) [α-Fe] Fe11, (b) [Fe_3O_4] Fe-oct and (c) [γ-Fe_2O_3] Fe-oct estimated from fitting of R-plots. Solid and dotted lines represent Fe NPs oxidized at 200 °C and 250 °C respectively.*

variations in values with time need to be ignored and emphasis should be on the overall trend of the degeneracy plots. For [Fe_3O_4] Fe-oct path, shown in **Figure 5.7b**, there is a sharp increase in degeneracy from 0 min to 2 min due to oxidation of α-Fe phase present in the core of the particles. However, 2 min onwards, as further oxidation takes place, conversion of Fe_3O_4 phase to γ-Fe_2O_3 phase takes place which leads to drop in degeneracy due to vacancy formation at octahedral sites, as observed for 200 °C samples. However, in case of 250 °C samples, a sharp increase is observed during early stages of oxidation due to the increase in crystallinity at higher temperatures, which over-compensates for the drop in CN. Due to these opposing factors, it is difficult to independently study the effect of temperature during oxidation of Fe NPs, and further studies are required with improved experimental conditions where effect of crystallinity is insignificant. **Figure 5.7c** shows the CN of **[**γ-Fe_2O_3] Fe-oct phase in the samples. Similar to the previous case, a sharp increase is observed from 0 min to 2 min due to the oxidation of α-Fe phase. However, after initial increase, a slight decrease in degeneracy is observed for both 200 °C and 250 °C samples which contradicts the hypothesis that immediate conversion of α-Fe phase to Fe_3O_4 phase followed by oxidation to γ-Fe_2O_3 over extended period of oxidation time. The current observation suggests that interconversion between the oxide phase might be taking place or an altogether formation of a

different oxide phase, which however is not observed in other characterization results. 15 min onwards, minor and constant increase in degeneracy values is observed which is due to the combined effect of increase in crystallinity and conversion of Fe(II) to Fe(III) at octahedral sites. Similarly, 250 °C samples show higher CN due to increased crystallinity of the NPs.

5.4 Conclusion

We have demonstrated the study of oxidation of Fe NPs at 200 °C and 250 °C. Phase transformation of NPs occur from α-Fe/oxide core/shell structure to hollow core with iron oxide present in the shell. Through the investigation with TEM, XRD, XANES and EXAFS; we elucidate that the shell is composed of mixed phases of Fe_3O_4 and γ-Fe_2O_3. The as-synthesized Fe NPs have amorphous structure and immediately form a thin layer of Fe_3O_4 and γ-Fe_2O_3 on exposure to air. As the particles are oxidized at high temperatures, the iron from the core diffuse out at a very fast rate and form iron oxide leading to increase in the shell thickness, whereas the vacancies diffuse inside and coalescence to form a hollow core. On further oxidation, the morphology of the particles does not change significantly, however, interconversion of different phases of iron oxide takes place. The Fe(II) atoms present at octahedral sites start to oxidize, leading to generation of vacancies which can be seen though the drop in concentration of Fe_3O_4 phase and increase in concentration of γ-Fe_2O_3 phase. Oxidation over extended period of time does not lead to any further changes, and phases present reach an equilibrium state with Fe_3O_4 and γ-Fe_2O_3 in the ratio 0.6:0.4. Study of oxidation at different temperatures of 200 °C and 250 °C shows that although it does not lead to any changes in phase contribution, there is a significant increase in crystallinity of the particles oxidized at 250 °C which is observed through increased intensity of peaks in R-plots and the higher values of degeneracies.

This work provides a basis for controlled oxidation of Fe NPs by varying the vacancies at octahedral sites which can be useful for tailoring the electrical and magnetic properties of the particles. We have further showed how XAFS can be explored to study the short range order of nanoparticles which complement the other characterization techniques such as XRD and TEM.

5.5 Supporting information

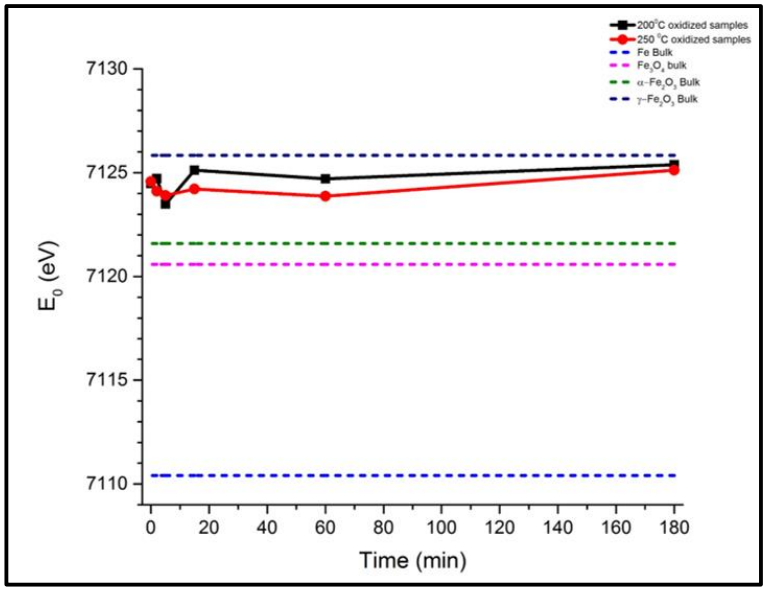

Figure 5.s1 *Plot shows the variation of edge energies of Fe NPs with time when oxidized at 200 °C and 250 °C. Dashed lines represent the edge energies of bulk standards.*

	0 min @ 200 °C						
Path	S02	N	sigma^2	e0	delr	Reff	R
[Fe] Fe1_1	0.701	1.169	0	-2.32	0.05945	2.4855	2.54495
[Fe3O4] O1_1	0.755	0.478	0.01461	-2.32	0.04687	1.8861	1.93297
[Fe3O4] Fe2_1	0.755	1.435	0.01461	-2.32	0.0865	3.4807	3.5672
[Y-Fe2O3] O3.1	0.83	3.603	0.01246	-2.32	-0.13079	2.0825	1.95171
[Y-Fe2O3] Fe-oct6.1	0.83	0.658	0.01246	-2.32	-0.18496	2.9451	2.76014
	2 min @ 200 °C						
Path	S02	N	sigma^2	e0	delr	Reff	R
[Fe3O4] O1_1	0.755	3.208	0.00104	0.598	0.03761	1.8861	1.92371
[Fe3O4] Fe2_1	0.755	1.587	0.00208	0.598	0.06942	3.4807	3.55011
[Y-Fe2O3] O3.1	0.83	1.949	0.00153	0.598	0.04446	2.0825	2.12696
[Y-Fe2O3] Fe-oct6.1	0.83	2.463	0.00306	0.598	0.06288	2.9451	3.00798
	5 min @ 200 °C						
Path	S02	N	sigma^2	e0	delr	Reff	R
[Fe3O4] O1_1	0.755	3.049	0.00025	0.591	0.03932	1.8861	1.92542
[Fe3O4] Fe2_1	0.755	1.309	0.0005	0.591	0.07256	3.4807	3.55326
[Y-Fe2O3] O3.1	0.83	1.672	0	0.591	0.03714	2.0825	2.11964
[Y-Fe2O3] Fe-oct6.1	0.83	1.848	0	0.591	0.05252	2.9451	2.99762
	15 min @ 200 °C						
Path	S02	N	sigma^2	e0	delr	Reff	R
[Fe3O4] O1_1	0.755	3.198	0.00079	-0.986	0.02823	1.8861	1.91433
[Fe3O4] Fe2_1	0.755	1.15	0.00158	-0.986	0.0521	3.4807	3.5328
[Y-Fe2O3] O3.1	0.83	1.78	0	-0.986	0.03315	2.0825	2.11565
[Y-Fe2O3] Fe-oct6.1	0.83	1.72	0	-0.986	0.04689	2.9451	2.99199
	60 min @ 200 °C						
Path	S02	N	sigma^2	e0	delr	Reff	R
[Fe3O4] O1_1	0.755	2.911	0	0.423	0.02999	1.8861	1.91609
[Fe3O4] Fe2_1	0.755	0.834	0	0.423	0.05535	3.4807	3.53605
[Y-Fe2O3] O3.1	0.83	1.907	0.00105	0.423	0.0398	2.0825	2.1223
[Y-Fe2O3] Fe-oct6.1	0.83	2.182	0.00211	0.423	0.05629	2.9451	3.00139
	180 min @ 200 °C						
Path	S02	N	sigma^2	e0	delr	Reff	R
[Fe3O4] O1_1	0.755	3.538	0	-1.213	0.01865	1.8861	1.90475
[Fe3O4] Fe2_1	0.755	1.148	0	-1.213	0.03441	3.4807	3.51511
[Y-Fe2O3] O3.1	0.83	2.2	0.00303	-1.213	0.0367	2.0825	2.1192
[Y-Fe2O3] Fe-oct6.1	0.83	2.443	0.00607	-1.213	0.0519	2.9451	2.997

Table 5.s1. *EXAFS fitting parameters for Fe NPs oxidized at 200 °C*

	0 min @ 250 °C						
Path	S02	N	sigma^2	e0	delr	Reff	R
[Fe] Fe1_1	0.701	1.214	0.00001	-1.251	0.09352	2.4855	2.57902
[Fe3O4] O1_1	0.755	0.596	0.01988	-1.251	0.03615	1.8861	1.92225
[Fe3O4] Fe2_1	0.755	1.789	0.01988	-1.251	0.06671	3.4807	3.54741
[Y-Fe2O3] O3.1	0.83	2.239	0.00324	-1.251	-0.12512	2.0825	1.95738
[Y-Fe2O3] Fe-oct6.1	0.83	0.254	0.00324	-1.251	-0.17694	2.9451	2.76816
	2 min @ 250 °C						
Path	S02	N	sigma^2	e0	delr	Reff	R
[Fe3O4] O1_1	0.755	3.164	0.00101	0.79	0.03682	1.8861	1.92291
[Fe3O4] Fe2_1	0.755	2.387	0.00202	0.79	0.06794	3.4807	3.54864
[Y-Fe2O3] O3.1	0.83	2.013	0.00013	0.79	0.03742	2.0825	2.11992
[Y-Fe2O3] Fe-oct6.1	0.83	2.364	0.00025	0.79	0.05292	2.9451	2.99802
	5 min @ 250 °C						
Path	S02	N	sigma^2	e0	delr	Reff	R
[Fe3O4] O1_1	0.755	3.366	0.00084	0.483	0.02813	1.8861	1.91423
[Fe3O4] Fe2_1	0.755	2.48	0.00168	0.483	0.05191	3.4807	3.53261
[Y-Fe2O3] O3.1	0.83	2.373	0.00308	0.483	0.03378	2.0825	2.11628
[Y-Fe2O3] Fe-oct6.1	0.83	3.386	0.00616	0.483	0.04778	2.9451	2.99288
	15 min @ 250 °C						
Path	S02	N	sigma^2	e0	delr	Reff	R
[Fe3O4] O1_1	0.755	3.536	0.00146	0.243	0.02723	1.8861	1.91333
[Fe3O4] Fe2_1	0.755	2.978	0.00292	0.243	0.05024	3.4807	3.53094
[Y-Fe2O3] O3.1	0.83	2.395	0.00193	0.243	0.03406	2.0825	2.11656
[Y-Fe2O3] Fe-oct6.1	0.83	3.09	0.00385	0.243	0.04817	2.9451	2.99327
	60 min @ 250 °C						
Path	S02	N	sigma^2	e0	delr	Reff	R
[Fe3O4] O1_1	0.755	3.219	0.00092	1.241	0.03149	1.8861	1.91759
[Fe3O4] Fe2_1	0.755	2.803	0.00184	1.241	0.05811	3.4807	3.53881
[Y-Fe2O3] O3.1	0.83	2.523	0.00208	1.241	0.03802	2.0825	2.12052
[Y-Fe2O3] Fe-oct6.1	0.83	3.453	0.00416	1.241	0.05377	2.9451	2.99887
	180 min @ 250 °C						
Path	S02	N	sigma^2	e0	delr	Reff	R
[Fe3O4] O1_1	0.755	3.689	0	-0.803	0.02195	1.8861	1.90805
[Fe3O4] Fe2_1	0.755	2.985	0	-0.803	0.04051	3.4807	3.52121
[Y-Fe2O3] O3.1	0.83	2.711	0.00545	-0.803	0.03357	2.0825	2.11607
[Y-Fe2O3] Fe-oct6.1	0.83	4.36	0.01091	-0.803	0.04747	2.9451	2.99257

Table 5.s2. *EXAFS fitting parameters for Fe NPs oxidized at 250 °C*

Part II

Enhanced supercapacitor performance for equal Co-Mn stoichiometry in colloidal $Co_{3-x}Mn_xO_4$ nanoparticles, in additive-free electrodes

Sanjaya D. Perera[†], Xiaoyue Ding[‡], Anuj Bhargava[†], Robert Hovden[‡], Andrew Nelson[†], Lena F. Kourkoutis[‡,*], Richard D. Robinson[†]

[†] Department of Materials Science and Engineering, Cornell University, 214 Bard Hall, Ithaca, New York 14853, United States

[‡] School of Applied and Engineering Physics, Cornell University, 271 Clark Hall, Ithaca, New York 14853, United States

* Kavli Institute at Cornell for Nanoscale Science, 420 Physical Sciences Building, Ithaca, New York 14853, United States

Chem. Mater., 2015, 27 (23), pp 7861–7873
DOI: 10.1021/acs.chemmater.5b02106

Chapter 6. Enhanced supercapacitor performance for equal Co-Mn stoichiometry in colloidal $Co_{3-x}Mn_xO_4$ nanoparticles, in additive-free electrodes

6.1 Abstract

Driven by the search for faster and more efficient energy storage systems, research efforts towards electrochemical capacitors, also known as supercapacitors, have dramatically increased in recent years. Transition metal oxides have been shown to exhibit both high specific capacitance because of faradaic redox activity and long cyclic life due to their robust crystal structure. Cationic substitutions in ternary oxides have shown dramatic improvements over binary analogues, but the peak stoichiometry is often arrived at by trial and error. Transition metal oxides are also hampered by low electronic conductivity, requiring the use of conducting additives such as carbon black. In this work we study the effect of cationic substitutions in $Co_{3-x}Mn_xO_4$ nanoparticles on electrochemical Li-ion energy storage in electrodes assembled without polymeric or conducting additives. We use a hot injection synthesis to produce colloidal Co-Mn nanoparticles with various ratios of Co:Mn. Through electrophoretic deposition (EPD), we assemble the metal nanoparticles onto current collectors, then oxidize them, forming electrochemical capacitors without carbon additives or polymeric binders ("additive-free" nanoparticle electrodes). We find that the highest-performing Co-Mn mixture has a 1:1 ratio of Co to Mn, and shows an energy density of 26.6 Wh/kg with a specific capacitance of 173.6 F/g. This nanoparticle electrode composition delivers a high power density of 3.8 kW/kg at a 5 A/g constant current discharge. The energy density and power density delivered by the optimal mixture is ~6× and ~3× higher, respectively, than that of

pure Co_3O_4 electrodes. The specific capacitance for the Co-Mn mixture is also ~4× better than the pure Co_3O_4 nanoparticle supercapacitor. This 1:1 composition exceeds the performance of the Mn-rich composition in energy density (~16×), power density (~12×), and specific capacitance (~20×). The optimum composition shows excellent stability with greater than 80% capacitance retention over 300 cycles. We attribute this peak-performance in the 1:1 equal mixture Co:Mn sample to an increased electronic conductivity for this stoichiometry, and also find that this stoichiometry has both a high Co^{3+}/Co^{2+} ratio and a high Mn^{3+}/Mn^{2+} ratio, compared to other samples. This work could lead to advanced tailoring of electrochemical storage based on design principles of the interrelationship between oxidation state, stoichiometry, and redox charge storage.

6.2 Introduction

While the current demand for electrical energy storage systems has been centered on Li-ion batteries, for applications that require higher power beyond Li-ion batteries there is a new-found research focus on electrochemical capacitors, also known as supercapacitors.[45,46,47] Electrochemical capacitors are divided into two main categories: electrochemical double-layer capacitors (EDLCs) and faradaic supercapacitors. In EDLCs, capacitors are formed at the electrode-electrolyte interface, and the capacitance mainly depends on the adsorbed ions on the electrode surface that create a charged double layer. In faradaic supercapacitors, redox reactions at the surface layer of the electrode also contribute to the charge generation and storage.[45] When a material undergoing faradaic reactions exhibits steady capacitance values throughout the charge-discharge processes, it can be characterized as a pseudocapacitive material.[48] Faradaic supercapacitors exhibit higher charge densities but slower charge transfer kinetics compared to EDLCs, since EDLCs have charges stored at the interface which is readily accessible.[49]

Nanoscale materials have received extensive attention in electrochemical capacitor research due to their high surface-to-volume ratio and reduced ion diffusion length.[45–47,50,51] For electrodes the main groups of materials are carbon, conducting polymers and transition metal oxides. Carbon has the advantages of high electronic conductivity and low cost,[52] but pure carbon lacks the ability to undergo faradaic reactions under reasonable conditions, and therefore has a lower gravimetric capacitance and lower energy density compared to faradaic materials.[53] Conducting polymers are inexpensive and possess high faradic capacity and high electronic conductivity when doped, but suffer greatly from cycling stability due to swelling and contraction during redox activity.[53–59] Transition metal oxides have both higher capacity than carbon and longer chemical stability than polymer materials, and are therefore being explored as alternative electrode materials.

The champion metal oxide is RuO_2, which exhibits excellent faradaic capacitive performance with high redox activity, long stability, and high proton/electron conductivity,[60,61] but the high cost and environmental harmfulness of Ru make it commercially unfavorable. Other metal oxides, such as Mn_xO_y,[62–65] Co_3O_4,[66,67] $Co(OH)_2$,[68,69] $NiO/Ni(OH)_2$,[70,71] V_2O_5,[49,72,73] SnO_2,[74] Fe_2O_3 and Fe_3O_4[75] have all been reported for their supercapacitance performance. Among these candidates, Co_3O_4 has remarkably high specific capacitance, with a theoretical value up to 3560 F/g, as well as high conductivity, but is limited by its electrochemical stability and thus cycle life.[76–81] Recent leading works on Co_3O_4 report steps toward reaching this high performance using thin-film Co_3O_4 coatings and other oxide morphologies, though the capacitance values are still modest compared to theoretical values. For instance, by chemically coating Co_3O_4 thin films on copper substrates, a specific capacitance of 118 F/g was achieved in aqueous KOH electrolyte solution,[82] and Co_3O_4 nanorods synthesized using a hydrothermal method showed a specific capacitance of 280 F/g using 2M KOH electrolyte, but the capacity retention is only ~30% after 800 cycles.[83] A close cousin of

the cobalt oxides are the manganese oxides, Mn_xO_y, also considered as promising candidates for supercapacitor electrode materials.[84] MnO_2 has high redox capacity with theoretical specific capacitance of 1370 F/g and long cycle stability, which have been achieved in a three-electrode system with mass loading of 5 μg in 0.1M Na_2SO_4 electrolyte solution.[64,85,86] In another example, amorphous hydrated manganese dioxide $\alpha - MnO_2 \cdot nH_2O$ anodically deposited on graphite showed a specific capacitance of 265-320 F/g in 3M KOH solution, as measured by cyclic voltammetry in a three-electrode system, with almost no decrease in specific capacitance during repeated charge-discharge tests.[87] It should be noted the specific capacitance of this electrode in that work was calculated based on the metal oxide loading mass only, neglecting the mass of the carbon additives.[87]

To achieve a synergy between cobalt oxide's high specific capacitance and manganese oxide's long cycle life we are targeting, in this work, composite metal Co-Mn oxides. Previous work on $CoMnO_2$/VGCF (vapor grown carbon nanofiber) electrodes prepared by thermal decomposition exhibited high specific capacitance of 630 F/g at 5 mV/s in 1M KOH and capacitance retention of 95% after 10,000 cycles.[88] Co/Mn mixed oxides, prepared by anodic electrodeposition of Mn^{2+} and Co^{2+}, achieved a specific capacitance of 170 F/g at a very slow scan rate of 2 mV/s in 0.5M Na_2SO_4 electrolyte.[89] Cobalt doped MnO_2 nanowires synthesized by a hydrothermal technique and mixed with acetylene carbon black and polyvinylidene fluoride (PVDF) showed an active-material-specific capacitance of 415 F/g at 0.2 A/g in 1M Na_2SO_4 aqueous electrolyte.[90] Porous $MnCo_2O_4$ and $CoMn_2O_4$ nanowires and mesoporous flake-like $MnCo_2O_4$, both mixed with acetylene carbon black and PVDF, showed peak active-material capacitance of 2108 F/g and 1487 F/g, respectively, both at 1 A/g in 2M KOH aqueous solution, although these results are based on weights of active materials only and do not take into account the total mass of the electrode.[91,92]

While there have been notable achievements with synthesis methods such as hydrothermal and vapor growth, solution phase colloidal nanoparticle synthesis is seen as an ideal method to integrate nano-engineered materials into industry because of the ability of organic-phase colloidal techniques to finely control size dispersion and to easily produce a large amount of nanocrystals with tailored size, shape, and composition under moderate temperatures at ambient pressures through scalable solution processing.[93–95]

The conventional methods to construct electrochemical storage electrodes from nanoparticles involves additives such as polymeric binders to create strong interparticle attachments and attachments between the particles and current collector, and conductive carbon to increase electronic conductivity. However, the addition of binders and conductive carbon increases the weight by ~10% to 40% and reduces the porosity of the electrode, which hinders the motion of ions in the electrolyte through the network.[96] To improve gravimetric capacitance (capacity/weight), binder-free and carbon-free electrodes have been pursued.[96,97] Our group has previously implemented electrophoretic deposition (EPD) to assemble high-density nanoparticle films with exceptional performance as battery electrodes,[96] nano-electronic films,[97] and catalysts.[98] The unique advantage of this technique is the ability to completely eliminate the use of additives, such as carbon and binders. Other methods to assemble nanoparticles—such as the conventional solvent evaporation methods—create incoherent nanoparticle films that have cracks and voids, poor mechanical strength, and poor inter-particle connection, resulting in slow charge transfer kinetics and low-quality supercapacitor electrodes.[99] EPD, by contrast, can form smooth and mostly defect-free large area nanoparticle films.[96,98,100,101] We have shown that these binder-free and carbon-free nanoparticle Li-ion battery electrodes assembled using EPD exhibit high gravimetric capacity compared to conventional assembly methods, as well as long cycle stability.[96]

Aside from our groups' work on additive-free battery electrodes, there has been only limited reports for creation of binder-free and carbon-free electrochemical storage electrodes from colloidal nanoparticles,[102] and, to our knowledge, there are no reports of creating supercapacitor electrodes from colloidal Co-Mn oxides nanoparticles with additive-free methods.

In this study, we demonstrate high-performing supercapacitor electrodes formed from mixed metal cobalt and manganese oxide spinels that have been assembled through EPD, without additives. We report a method to synthesize mixed metal Co-Mn oxide nanoparticles with different Co:Mn molar ratios using a colloidal hot-injection reaction. The advantage of this synthesis is that we can control the Co:Mn ratio of $Co_{3-x}Mn_xO_4$, and therefore can study the electrochemical characteristics of our electrodes as the Co and Mn composition is varied. We find that the peak-performing Co-Mn composition has a Co:Mn ratio of nearly unity, with x=1.49 in $Co_{3-x}Mn_xO_4$. These $Co_{3-x}Mn_xO_4$ (x=1.49) nanoparticle electrodes show an energy density of 26.6 Wh/Kg, specific capacitance of 173.6 F/g, and power density of 3.8 kW/Kg at a 5 A/g constant current discharge. Compared to the other compositions, the x=1.49 composition shows an anomalous increase in performance: the energy density and power density delivered by the x=1.49 NP electrode is ~6 times and ~3 times greater than that of pure Co_3O_4 electrodes and ~16 times and ~12 times greater than that of the Mn-rich phase (x=2.54). We attribute this peak performance to an increased electronic conductivity for this stoichiometry, and also find that this stoichiometry has both a high Co^{3+}/Co^{2+} ratio and a high Mn^{3+}/Mn^{2+} ratio compared to other samples.

6.3 Experimental

6.3.1 Materials and characterization

Diphenyl ether (≥ 99%), dicobalt octacarbonyl (moistened with hexane (1-10%), ≥ 90% (Co)), dimanganese decacarbonyl (98%), trioctylphosphine oxide (technical grade, 90%), lithium bis(trifluoromethane)sulfonimide (≥ 99%), 1,3-dioxolane (99.8%), 1,2-dimethoxyethane (99.5%), and copper foils were purchased from Sigma-Aldrich. Oleic acid (≥ 90%) was purchased from Alfar Aesar, acetone (≥ 99%) and hexane (≥ 98.5%) were purchased from BDH Chemicals, and ethanol (≥ 99%) was purchased from Koptec. Standard Schlenk line techniques were employed during experiments under a nitrogen atmosphere at a pressure of ~1 atm. Transmission electron microscopy (TEM) images were recorded on an FEI Tecnai T12 TEM operating at 120 kV; high-resolution TEM (HRTEM) images were collected on an FEI Tecnai F20 TEM operating at 200 kV. High-angle annular dark-field (HAADF) and electron energy loss spectroscopic (EELS) data were acquired on a 5^{th}-order aberration-corrected scanning transmission electron microscope (Nion UltraSTEM) operated at 100 kV with a probe forming semi-angle of roughly 30 mrad and a collection semi-angle around 80-240 mrad and 0-60 mrad for HAADF and EELS, respectively. Resolution just below ~1 Angstrom is roughly the information transfer limit for this microscope optimally operating under these conditions. The EELS signal was obtained by integration over the $L_{2,3}$ core loss edges for Co and Mn and the K edge for O; all of which was done after background subtraction. The background EELS spectrum was modeled using a linear combination of power laws and a conservative local background average ranging from 2 to 4 pixels FWHM (smaller than the background variation). This provided a marginal improvement over traditional power law background modeling. These techniques were implemented using the open-source Cornell Spectrum Imager software and are described in more detail by P. Cueva et al.[103] A Scintag

Theta-Theta X-ray diffractometer (Cu K_α radiation) was employed to record X-ray diffraction data. X-ray photoelectron spectroscopy (XPS) analysis was performed using a Surface Science Instruments SSX-100 with operating pressure ~$2x10^{-9}$ Torr. Monochromatic Al K_α x-rays (1486.6 eV) were used with beam diameter of 1 mm. Photoelectrons were collected at a 55° emission angle. A hemispherical analyzer determined electron kinetic energy, using a pass energy of 150V for wide/survey scans, and 50V for high resolution scans. A flood gun was used for charge neutralization of non-conductive samples. Cyclic voltammograms (CV) and galvanostatic charge/discharge curves were obtained using an Arbin supercapacitor testing station (BT2000), and electrochemical impedance spectroscopy analysis was performed using a Bio-Logic VMP3 potentiostat.

6.3.2 Synthesis of $Co_{3-x}Mn_xO_4$ nanoparticles

A mixture of 0.1 g tri-*n*-octylphosphine oxide (TOPO) and 6 g diphenyl ether (DPE) was kept under nitrogen environment at 1 atm and heated up to 250 °C. Different molar ratios of dicobalt octacarbonyl and dimanganese decacarbonyl were dissolved in 4 g DPE, heated at 80 °C and stirred for 1 h. The Co-Mn molar ratios are: 1:0.25, 1:0.5, 1:1, 1:2, 1:4.

The precursors are then injected into the TOPO-DPE mixture at 250 °C to begin the reaction. After the injection of the yellow-brown mixture of $Co_2(CO)_8$ and $Mn_2(CO)_{10}$ carbonyl precursor solution, the color rapidly changes to dark brown. If only the cobalt precursor is used, the color changes from yellow-brown to dark black after the injection. To control the Co to Mn ratio in the nanoparticles (NPs), the molar ratio of the cobalt and manganese precursors was varied. Heating the reaction vessel at 250 °C for 30 mins allows nucleation and growth of Co-Mn nanoparticles.[104] The products are then precipitated by adding ethanol and isolated by centrifugation. Precipitates

were then readily dissolved in 6 mL of hexane for electrophoretic deposition and further characterization. In order to oxidize the samples, the precipitates were dried and then annealed in air at 200 ℃ for 90 min.

6.3.3 Synthesis of Co_3O_4 nanoparticles

Co_3O_4 nanoparticles were synthesized using exactly the same method described above but with only the precursor of 0.5mmol dicobalt octacarbonyl dissolved in 4g DPE, heated at 80℃ and stirred for 1h.

6.3.4 Electrophoretic deposition of nanoparticles

The solutions of nanoparticles in hexane obtained from the syntheses described above were further diluted for electrophoretic deposition (EPD). EPD methods follow our previous work.[96–98] In typical EPD process, 200 μL of original concentrated solution was added into 10 mL hexane. Copper plates with known weight were used as electrode substrates. Two stainless steel conductors were connected to the positive and negative output of a DC voltage source. One copper plate each was attached to conductors using small strips of double-sided tape, with care being taken to make sure that each plate was contacting the conductor. The separation between two conductors was 1 cm. The conductors were then dipped into diluted nanoparticle solution until the copper plates were completely submerged. The DC voltage source was set to 600V. EPD processes were carried for ~3min to 1h, based on the time needed to obtain clear solutions. The final mass of electrode materials is 0.10 ± 0.02 mg for all samples tested. The EPD speed strongly depends on the molar ratios of Co:Mn in the nanoparticle sample. Typically, the greater the Co percentage, the faster the

EPD process. After the EPD process, all electrodes were annealed in air at 200 °C for 90 min. The mass of the electrodes was measured after annealing to calculate the mass of active materials.

6.3.5 Fabrication of Supercapacitors

Electrodes with $Co_{3-x}Mn_xO_4$ were made into coin-cell type asymmetric supercapacitors, in which the $Co_{3-x}Mn_xO_4$ material acted as the anode. Carbon fiber was used as the cathode. The electrolyte used in the supercapacitors was 1 M lithium bis-trifluoromethanesulfonimide (LiTFSI) dissolved in a 1:1 ratio of 1,3-dioxolane (DOL) and 1,2 dimethoxyethane (DME) solution. In our study LiTFSI in organic solvent was used as the electrolyte. Compared to aqueous electrolytes, organic electrolytes have larger potential windows. During the charge and discharge process, Li^+ ions from the electrolyte shuttle between the cathode and anode electrodes.

6.4 Results and Discussion

Co-Mn nanoparticles were prepared according to the scheme shown in **Figure 6.1a**. The metal precursors $Co_2(CO)_8$ and $Mn_2(CO)_{10}$ were first dissolved in diphenyl ether (DPE) at 80 ^oC, and then quickly injected into a mixture of TOPO and oleic acid in DPE in an N_2 atmosphere at 250 ^oC. Both metal and metal oxide NPs are approximately spherical, as characterized by transmission electron microscopy (TEM) (**Figure 6.s1, a-f**). In general, for identical synthesis conditions, the pure Co nanoparticles are larger (the average diameter is 5.66 ± 2.21 nm) than the mixed Co-Mn metal NPs (average size is 3~4 nm, see **Table 6.s1**). After EPD of the Co-Mn metal NPs onto the current collectors, the metal NPs are heated in air at 200 ^oC for 90 minutes, forming $Co_{3-x}Mn_xO_4$ NPs. The same synthesis using $Mn_2(CO)_{10}$ alone was also performed; however, no nanoparticle

product was obtained, indicating that pure Mn nanoparticles cannot be synthesized by following this protocol. Inductively coupled plasma mass spectrometry (ICP-MS) of the oxide products show that the Co/Mn ratio in the NP products roughly follows the precursor ratio (**Table 6.1**). (From here on, the samples will be indexed by their "*x*" value in $Co_{3-x}Mn_xO_4$. **Table 6.1** lists the six compositions studied.) The initial Co metal NPs enlarge and hollow from the oxidation (**Figure 6.s1a**), attributed to the nanoscale Kirkendall effect, which has been previously observed during the oxidation of cobalt nanoparticles.[96,105] Other metal NPs also enlarged during oxidation (**Figure 6.s1 b-f**), but without an observable Kirkendall hollowing. For instance, the as-synthesized Co-Mn (precursor ratio 1:1) metal NPs that are oxidized into the $Co_{3-x}Mn_xO_4$ (x=1.49) NPs have an average diameter of (3.87 ± 0.80) and (4.78 ± 0.81) nm for the metal NPs and oxide NPs, respectively (**Figure 6.s1d** and **Figure 6.1c**). SEM images of the $Co_{3-x}Mn_xO_4$ EPD thin films show that the NPs tend to form small clusters upon heating, which consists of 4-5 NPs (**Figure 6.1b**). While heating, EPD films tend to densify, increasing the packing of the NPs, as shown in our previous work on cobalt oxides.[96] Our previous work has also shown that EPD films are porous, but have higher packing density than do either spin cast or drop cast films.[97,98] Therefore, EPD-assembled films show a closely packed dense network of $Co_{3-x}Mn_xO_4$ NPs while retaining the porosity of the electrodes (see **Figure 6.1b**), which is essential for fast ion diffusion and charge transfer in supercapacitors.

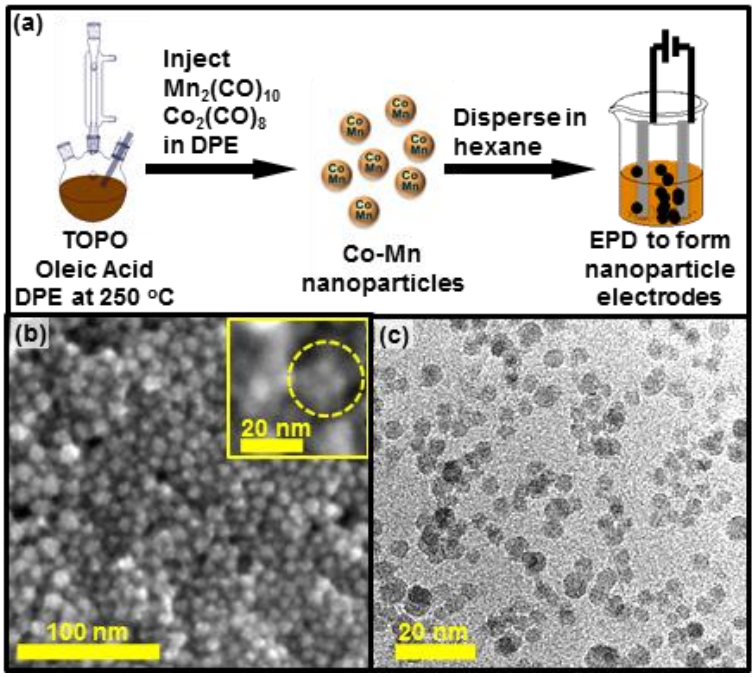

Figure 6.1. *(a) Schematic diagram showing the synthesis of Co-Mn nanoparticles and the preparation of carbon and additive free electrodes using the EPD technique. (b) SEM image of a* $Co_{3-x}Mn_xO_4$ *(x=1.49) electrode assembled through EPD. Inset image shows clusters of nanoparticles. (c) TEM image of nanoparticles in the* $Co_{3-x}Mn_xO_4$ *(x=1.49) sample.*

Precursor ratio (Co:Mn)	$Co_{3-x}Mn_xO_4$ content determined by ICP-MS	Mean size and std. dev. of oxidized NP (nm)
1:0	x=0 (Co_3O_4)	7.14 ± 2.03
1:0.25	x=0.22	3.16 ± 0.57
1:0.5	x=0.76	4.39 ± 0.69
1:1	x=1.49	4.78 ± 0.81
1:2	x=1.89	3.07 ± 0.51
1:4	x=2.54	3.35 ± 0.41

Table 6.1. *Precursor ratio of the metals, stoichiometry of the metal oxides as determined by ICP-MS, and corresponding particle size analysis after annealing metal nanoparticles in air. All samples have increased size compared to as-synthesized nanoparticles (**Table 6.s1**).*

The atomic scale structure and composition of the $Co_{3-x}Mn_xO_4$ (x=1.49) sample are mapped using aberration-corrected STEM in combination with Electron Energy Loss Spectroscopy (EELS) (**Figure 6.2 a-f**). High-angle annular dark field (HAADF) STEM images of a series of NPs, oriented along different crystallographic axes, primarily show the spinel structure (**Figure 6.2 a,c,d,e** and **Figure 6.s2 a,b,c**). While most particles appear fully crystalline in the HAADF-STEM projection images, core-shell lattice distinctions are observed in some HAADF-STEM images. **Figure 6.2c**, for example, shows a slightly off axis [100] spinel core and a shell down the [100] direction of a rock-salt crystal structure. Elemental mapping with EELS (**Figure 6.2f** and **Figure 6.s2d**) reveals that a majority of the nanoparticles have a Mn-rich center and a Co-rich shell, while O-atoms are distributed homogenously throughout the nanoparticles. Clear variations of the HAADF intensity amongst atomic columns of same or similar thickness, particularly in the shell further evidence Co/Mn intermixing (for example, intermixing of heavy atoms from **Figure 6.2c** are shown in **Figure 6.s2 e-g**). The intermixing is often inhomogeneous—**Figure 6.s2 b,d** shows inhomogeneous HAADF variation. Furthermore, shells are not always uniform in thickness or complete (as seen in **Figure 6.s2b**). We also studied the x=0.76 and x=1.89 samples for homogeneity (**Figure 6.2 g-j**). STEM HAADF imaging and EELS mapping of these samples are consistent with x=1.49 phase, showing large crystalline spinel Co-Mn-O nanoparticles consisting of a Mn-rich core and a Co-rich shell, with both cations present in both core and shell. A minority of amorphous Co-O material is present in the x=0.76 phase. While these characterization results provide important information, further work is needed to quantify the contributions of the different phases and amorphous materials.

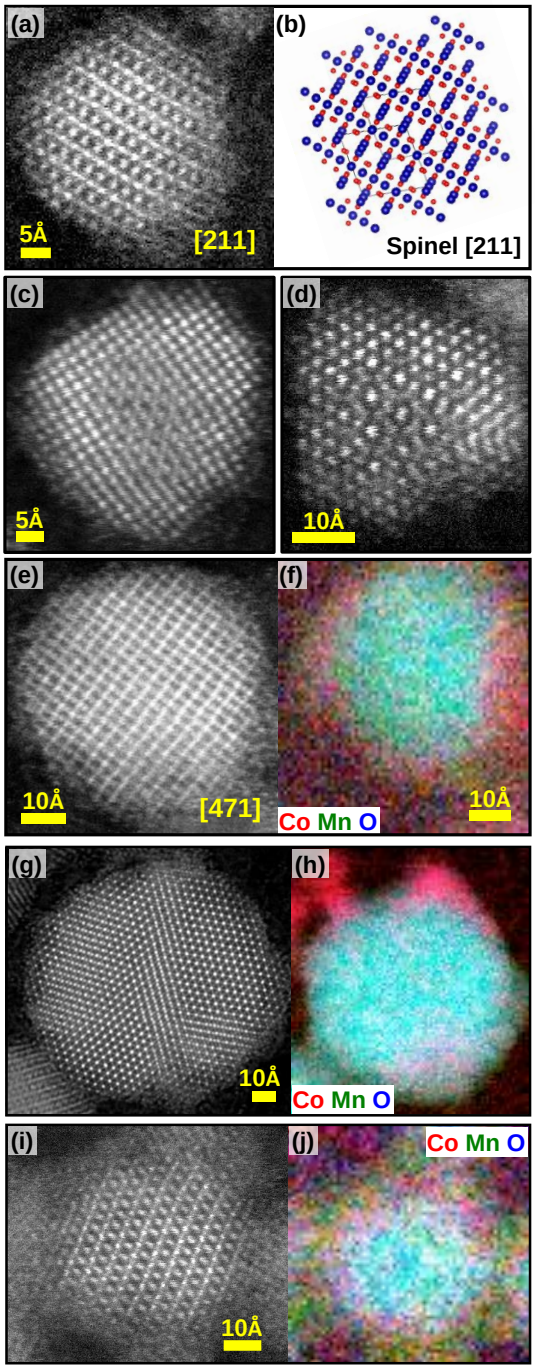

Figure 6.2. *HAADF STEM imaging and EELS elemental mapping of nanoparticles in the* $Co_{3-x}Mn_xO_4$ *for x=1.49 (**a-f**), x=0.76 (**g**,**h**), and x=1.89 (**i**,**j**) samples. HAADF STEM images of (**a**) a particle oriented along the [211] direction of a spinel structure, diagramed in (**b**); (**c**) a nanoparticle with clear core-shell structure, showing a [100] rocksalt shell and a slightly off-axis [100] spinel core; and (**d**) a nanoparticle viewed in the [110] spinel direction (core) and rocksalt [110] (shell). (**e**) HAADF STEM image of a nanoparticle oriented along the [471] direction of a spinel structure and (**f**) the corresponding EELS elemental map, which shows a Co-rich shell and a Mn-rich core. (**g-j**) HAADF-STEM image of a nanoparticle of a spinel structure and the*

*corresponding EELS elemental map that shows a Co-rich shell and a Mn-rich core for samples x=0.76 (**g**,**h**) and x=1.89 (**i**,**j**). Spinel structure referenced in Liu et al.*[106]

X-ray diffraction (XRD) patterns of $Co_{3-x}Mn_xO_4$ NPs (**Figure 6.3**) coupled with ICP-MS data indicates that the Mn ion becomes incorporated into the Co_3O_4 spinel lattice. As the Mn content is increased, the strong Co_3O_4 XRD peaks around ~37° (311) and ~45° (400) both shift to smaller 2θ angles starting with the x=1.49 sample and eventually align with the $CoMn_2O_4$ phase for the two highest Mn-content materials (x=1.89 and 2.54). These peak shifts suggest the incorporation of Mn into the Co_3O_4 structure. Note that it has been previously shown that the Mn and Co ions are interchangeable in the crystal.[92] Additionally, two peaks associated with (202) and (113) planes of $CoMn_2O_4$ at 29.2° and 32.9°, respectively, appear in the two highest Mn-content samples (x=1.89 and 2.54), while the Co_3O_4 ~37° peak disappears. The 29.2° and 32.9° peaks are closely matched with the XRD of $CoMn_2O_4$ (JCPDS: 01-077-0471). Among all the samples, the x=2.54 sample shows a pronounced peak shift in 2θ of ~0.94° for the most intense peak at ~37° (311). In addition to the peak shifts the ~37° peak becomes asymmetric for the higher Mn-content samples, (x=1.89 and 2.54), suggesting the reaction mixture tends to form separate phases. We note due to the breadth of the XRD peaks, more detailed structural information may be hidden. Additionally, while it is unclear if this phase segregation occurs during the synthesis, oxidation, or EPD, we note that in our previous work on cobalt oxide there was no difference in phases or oxidation states between films oxidized after EPD and oxidized nanoparticle powders.[96] Based on ICP-MS, the Co:Mn ratio of the $Co_{3-x}Mn_xO_4$ (x=1.49) sample has a molar ratio of 1:1.008 (see **Table 6.s2**). It is interesting to note that XRD characterization shows only a single phase at equal Co:Mn stoichiometry $Co_{3-x}Mn_xO_4$ (x=1.49), suggesting homogeneous particles. The high spatial

resolution structural and elemental information obtained by aberration corrected STEM-EELS, however, reveals an inhomogeneous composition with Co-rich shell and Mn-rich core.

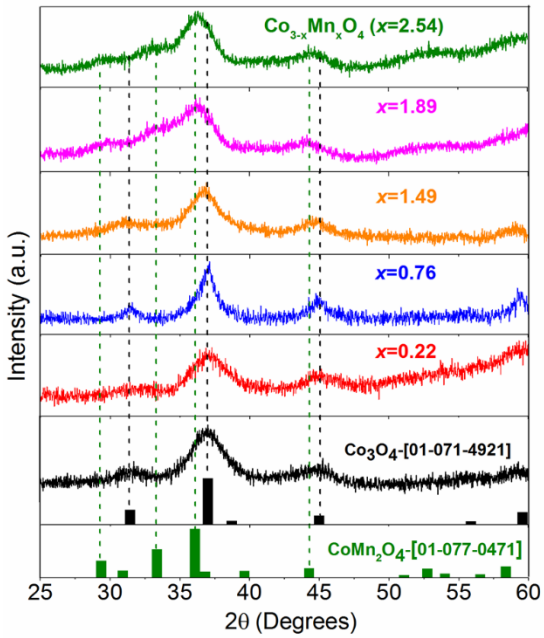

Figure 6.3. *X-ray diffraction (XRD) patterns of the $Co_{3-x}Mn_xO_4$ films. The bar patterns show the reference XRD pattern for Co_3O_4 (JCPDS: 01-071-4921) and $CoMn_2O_4$ (JCPDS: 01-077-0471). At higher Mn contents the intense (311) XRD peak (~37°) shifts towards lower angles, which is an indication of the presence of Mn in the Co_3O_4 lattice. The 29.2° and 32.9° peaks of $CoMn_2O_4$ (JCPDS: 01-077-0471) reference XRD pattern are aligned with the higher Mn-content samples.*

The electrochemical performance of the $Co_{3-x}Mn_xO_4$ nanoparticle electrodes was evaluated using coin cell type (two electrode system) supercapacitors. For a full conversion reaction, the proposed electrochemical reaction of the Co_3O_4 NP electrode with Li^+ is shown in equation (6.1) (discharge), equation (6.2) (charge), and equation (6.3) (charge):[67]

$$Co_3O_4 + 8Li^+ + 8e^- \rightarrow Li_xCo_3O_4 + (8-x)Li^+ + (8-x)e^- \rightarrow 3Co + 4Li_2O \quad (6.1)$$

$$3Co + 3Li_2O \leftrightarrow 3CoO + 6Li^+ + 6e^- \quad (6.2)$$

$$3Co + 4Li_2O \leftrightarrow Co_3O_4 + 8Li^+ + 8e^- \quad (6.3)$$

In Co-Mn oxides, the common lithiation-delithiation conversion reaction is (equation (6.4)):[107]

$$Co_xMn_{(3-x)}O_4 + 8Li^+ + 8e^- \leftrightarrow (3-x)Mn + xCo + 4Li_2O \quad (6.4)$$

It has been previously shown that during the conversion reaction in Li-ion batteries, thermodynamically stable Li_2O is produced and forms Mn. In the Co-Mn oxides the cations of Mn^{3+}, Mn^{2+} and Co^{3+}, Co^{2+} can be reduced to metallic Mn and Co.[108]

However, for supercapacitor reactions, which charge-discharge much faster than Li-ion batteries, it is likely that in non-aqueous electrolytes the Li-ions are used to store charge via a redox reaction involving a change in oxidation state of the transition metal. The lithium ion is accommodated in the oxide following a reduction reaction from Co^{3+}/Mn^{3+} to Co^{2+}/Mn^{2+}, without full conversion to the Co/Mn metal. For instance, in MnO_2 this reaction can be expressed as $Mn^{IV}O_2 + xe^- + xLi^+ \rightleftarrows Li_xMn_x^{III}Mn_{1-x}^{IV}O_2$.[109,110] This cation-electron reduction reaction with the transition metal is the likely mechanism of charge storage in our cobalt-manganese oxide supercapacitors.

Cyclic voltammetry (CV) was used to study the charge storage capacity and mechanism in the $Co_{3-x}Mn_xO_4$ NP electrodes. In order to select the optimum voltage window, cyclic voltammograms were acquired at different potential windows (**Figure 6.s3a**). At higher voltage windows the shape of CV curves distorts from the quasi-rectangular shape due to peaks from redox reactions (>1.4V in **Figure 6.s3a**). Compared to higher potential windows, the CV recorded at the 1.4 V potential window from -1.0 to 0.4 V shows the least deviation from a rectangular shape, which is the ideal shape for a capacitor. **Figure 6.s3b** shows the calculated coulombic efficiencies for different voltage windows (see **6.6 Supporting Information**). The potential window of 1.4 V operates at a coulombic efficiency of ~95%. At higher voltage windows the coulombic efficiency gradually

drops, which may be due to irreversible reactions induced by over-charging,[111] and faradaic peaks begin to appear. It is important to use the maximum possible voltage to achieve the highest energy density and capacity while maintaining a nearly rectangular CV. Therefore, 1.4 V was selected as the fixed potential window for all electrochemical analysis. The corresponding CV curves acquired at a scan rate of 25 mV/s in the voltage range of -1.0 to 0.4 V are shown in **Figure 6.4a**.

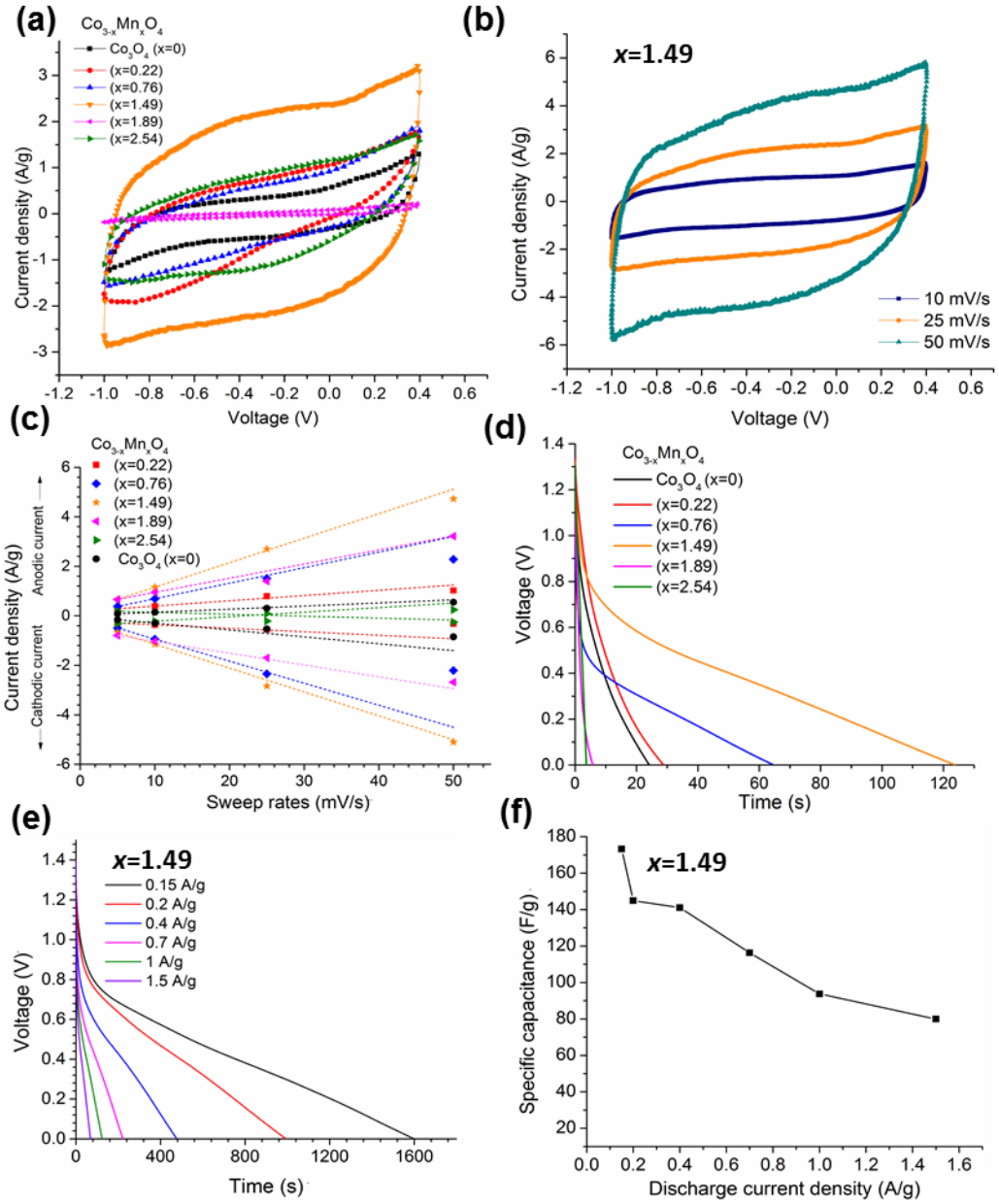

Figure 6.4. *(**a**) Cyclic voltammograms of Co_3O_4 and $Co_{3-x}Mn_xO_4$ electrodes for the six stoichiometries tested (x=0 to x=2.54) (acquired at a sweep rate of 25 mV/s). (**b**) Cyclic voltammograms of $Co_{3-x}Mn_xO_4$ (x=1.49) acquired in -1.0 to 0.4 V voltage window at 10, 25, and 50 mV/s sweep potentials. (**c**) Current density (at -0.3 V) as a function of sweep rate for different $Co_{3-x}Mn_xO_4$ compositions. Solid lines and dashed lines are linear fits to the anodic and cathodic contributions, respectively. The $Co_{3-x}Mn_xO_4$ (x=1.49) shows the highest current output at sweep rates from 5 to 50 mV/s. (**d**) Discharge profiles recorded at a constant current density of 1 A/g for $Co_{3-x}Mn_xO_4$ compositions. (**e**) Discharge profile for the $Co_{3-x}Mn_xO_4$ (x=1.49) electrode for different constant current densities. (**f**) Calculated specific capacitance at different constant discharge current densities for $Co_{3-x}Mn_xO_4$ (x=1.49) electrode.*

The CV curves for the different Co:Mn compositions show a quasi-rectangular shape, indicating the combination of an electric double layer and redox activity of the metal oxides (**Figure 6.4a**).[112,113] The small size of these nanoparticles helps facilitate the formation of a high-capacity electrical double layer due to the high surface area of the electrodes. The CV of the x=1.49 electrode shows the highest output current density and integrated total charge of all the Co:Mn samples. These CV curves indicate that as the Co:Mn content increases from x=0 (Co_3O_4) to x=1.49, the current density and integrated charge increases, and then reaches a maximum at the x=1.49 composition. After this point, the addition of Mn in the precursor significantly decreases the performance of the material as measured by CV (the maximum current density decreases; see **Table 6.s3** in supporting materials). Based on our electrochemical analysis (details to follow), the x=1.49 sample corresponds to the optimum composition for electrochemical capacitive charge storage.

We will now examine the results of our two-electrode devices in more detail. It is interesting to note that the x=2.54 sample, which consists of the highest amount of Mn, displays a much lower current density compared to pure Co_3O_4. It is known that the Mn-based metal oxides have poor electrical conductivity compared to cobalt oxides,[90,92,114] therefore, the Mn-rich samples could be exhibiting poor performance due to the inherently poor electrical conductivity of the Mn-oxides.

It has been previously shown that high capacities can be achieved from a combination of two or more transition metal oxides because the composite can possess the advantages of all compositions during the charge-discharge process.[115,116] It is known that cobalt oxides have a higher oxidation potential than manganese oxides, while manganese oxides can have multiple oxidation states that can undergo redox during charge and discharge, enabling cobalt manganese oxides to deliver higher capacity.[117] Previous work has reported maximum electronic conductivity in $Co_{3-x}Mn_xO_4$ dense ceramics when $x \approx 1.25$.[114]

To analyze the retention of capacitive properties of the top-performing x=1.49 NP electrode, CV curves were recorded at different voltage scan rates (10, 25, and 50 mV/s; **Figure 6.4b**). A key indicator of performance is the ability to retain the capacitive properties of a supercapacitor at higher scan rates. The x=1.49 NP electrode shows a quasi-rectangular shape at 50 mV/s, delivering an output current density of 4 A/g. **Figure 6.s4** compares the stored charge of x=1.49 and x=0 (Co_3O_4) NP electrodes at sweep rates from 5 to 50 mV/s with a voltage window of 1.4 V, which corresponds to charge/discharge time between 28 to 280 s. Compared to the Co_3O_4 electrode, the $Co_{3-x}Mn_xO_4$ (x=1.49) electrode can store ~5 times more charge. The anodic and cathodic current densities were further analyzed as a function of sweep rate to understand the linearity of the average current density with different sweep rates (**Figure 6.4c** and **Table 6.s3**). For the compositions tested, the behavior of the current density with different sweep rate has two distinguishing features: First, the x=1.49 sample exhibits the highest current output at a 50 mV/s sweep rate; and second, only the Co_3O_4 and the x=1.49 samples have an output current that varies linearly with the range of the sweep rate.

Electrochemical analysis of the $Co_{3-x}Mn_xO_4$ electrodes was conducted using galvanostatic charge-discharge at a constant current density for the $Co_{3-x}Mn_xO_4$ compositions (**Figure 6.4d**)[118–120]. The

x=1.49 ratio sample displays the longest time to discharge, which is an indication of the highest redox activity among the samples (assuming the surface capacitive charge is equal between samples; see **Figure 6.s5** for charge/discharge curves at a constant current density). The discharge profiles for different compositions (**Figure 6.4d**) appear to have two distinct regions of behavior: 1) A steep voltage drop (0 to ~20 sec) at higher voltages suggests an initial high charge transfer resistance.[121] This behavior is associated with the electronic conductivity and the ability of the ions to access the redox materials. This could also be due to internal resistance in our system since there are no carbon conductor additives between nanoparticles; and 2) A near-linear decrease in voltage at lower voltages, with no voltage plateaus, suggests the balanced effect of both double layer and redox activity during the discharge process, leading to capacitive behavior.[122]

To analyze the discharge profile of the top-performing *x*=1.49 NP electrode, we evaluated the electrochemical characteristics using galvanostatic discharge from 1.4 to 0 V with different current densities (**Figure 6.4e**). Charge and discharge profiles were recorded at a constant current density of 0.25 A/g. The energy density (E), power density (P), and specific capacitance (C_{sp}) of the device were calculated according to the equations (6.5), (6.6) and (6.7):

$$E = \int \frac{V \cdot I \cdot dt}{m} \tag{6.5}$$

$$P = \frac{E}{\Delta t} \tag{6.6}$$

$$C_{sp} = \frac{I \cdot \Delta t}{\Delta V} \cdot \frac{1}{m} \tag{6.7}$$

Where I is the constant discharge current density, Δt is the discharge time, ΔV is the voltage difference measured after the initial (occurring in the first ~0.001 seconds) internal resistance ("IR") voltage drop (voltage difference between the end of charge/discharge and the beginning of next discharge/charge, due to current flowing across the capacitor's internal resistance) and *m* is the total mass of the active material.[45,111] **Figure 6.4f** shows the specific capacitance calculated for the *x*=1.49 electrode at different constant current discharge conditions. The specific capacitance is 173 F/g at current density of 0.15 A/g, 144 F/g at 0.2 A/g, and retains a robust 116 F/g at current density of 0.7 A/g, indicating a stable and high capacitive performance.

Discharge analysis results for electrodes with different compositions are shown in **Figure 6.5** (and tabulated in **Table 6.s4**), which clearly demonstrate the anomalous improvement in performance by the x=1.49 Co:Mn composition compared to the other compositions. The *x*=1.49 NP electrode shows an energy density of 26.6 Wh/kg with 173.6 F/g specific capacitance at a 0.1 A/g constant current discharge. The *x*=1.49 NP electrode delivered the highest power density of ~3,800 W/kg at a 5 A/g constant current discharge. The energy density and power density delivered by the *x*=1.49 NP electrode is ~6 times and ~3 times higher, respectively, than that of the pure Co_3O_4 electrodes (see **Table 6.s4**). The energy density of the *x*=1.49 sample is twice as high as the next highest-performing composition (the *x*=0.76 electrode). The *x*=1.49 electrode delivers higher specific capacitance than all other compositions with nearly 2× the performance of the next-highest performing composition (*x*=0.76) and nearly 5× the performance of Co_3O_4. **Figure 6.s6** shows the cyclic voltammograms of the Co_3O_4 and $Co_{3-x}Mn_xO_4$ (x=1.49) electrodes plotted as specific capacitance (dQ/dV, where Q is charge) vs the cell potential, which confirms the improved capacitive behavior of the *x*=1.49 NP electrode. The higher specific capacitance (**Table 6.s4**) and

higher current density (**Figure 6.4c**)[111] indicate faster charge transfer kinetics observed for the *x*=1.49 electrode.

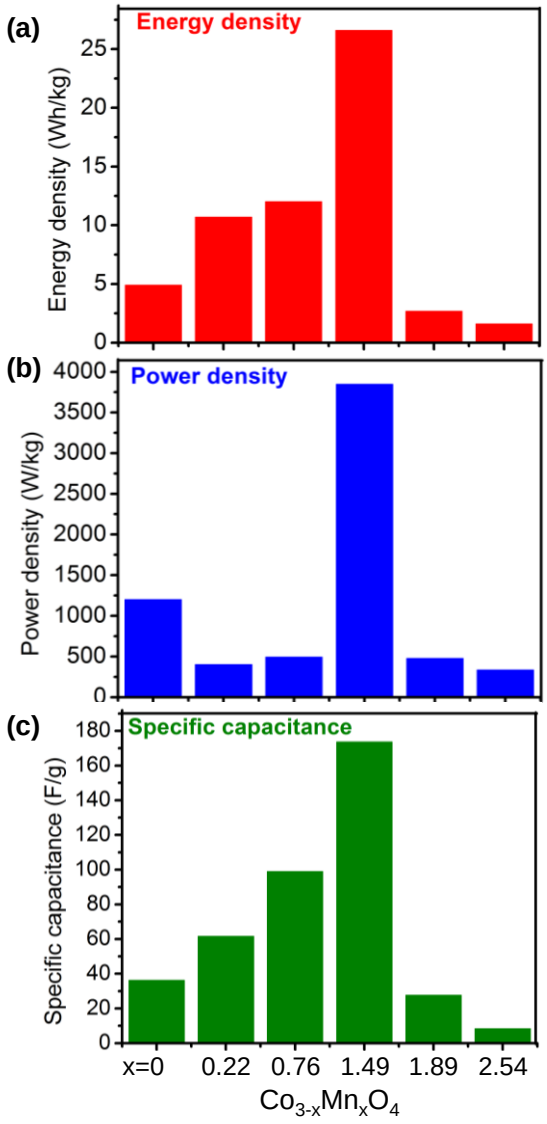

Figure 6.5. *Calculated values of* (***a***) *energy density,* (***b***) *power density and* (***c***) *specific capacitance for* $Co_{3-x}Mn_xO_4$, *x=0, 0.22, 0.76, 1.49, 1.89, and 2.54. To obtain the energy density and specific capacitance, the electrodes were discharged at a constant current density of 0.1 A/g. To obtain the maximum power density the supercapacitors were discharged within ~5s. The x=1.49 composition shows the highest energy density, power density, and specific capacitance.*

To characterize the transport kinetics of charged species, electrochemical impedance spectroscopy (EIS) was employed for the pure Co_3O_4 (x=0), the x=1.49 (equal Co/Mn) and the x=2.54 (Mn-rich) electrodes. The impedance response to frequency is expressed as a Nyquist plot, which shows the real and imaginary part of the impedance, with the real part plotted on the x-axis and the negative of the imaginary part on the y-axis, each point on the plot representing the impedance at a given frequency. The Nyquist plot is plotted over the frequency range of 100 kHz to 100 mHz for the x=0 (Co_3O_4), x=2.54, and x=1.49 supercapacitors (**Figure 6.6a**), with the frequency decreasing moving from left to right (see **6.6 Supporting Information** for details on EIS).

The impedance behaviors of the samples show similar characteristics, consisting of a semicircle associated with charge transfer across the double layer and a straight line in the low frequency region, with the knee frequency point defined as the crossover between these regions. It is apparent from the impedance spectra that the charge transfer resistance R_{ct} (equivalent to the diameter of the semicircle) is much lower for the x=1.49 electrode as compared to the Co_3O_4 and x=2.54 electrodes, and the knee frequency for the x=1.49 electrode is higher. The knee frequency (see **Figure 6.6a**) for the Co_3O_4 electrodes is ~5Hz for x=0, ~7Hz for x=2.54, and ~10Hz for x=1.49, thus indicating that the x=1.49 electrode delivers its stored energy almost two times faster than does the Co_3O_4 electrode. In general, supercapacitors demonstrate resistive behavior at high frequencies and capacitive behavior at low frequencies, with the sharp linear increase in Z" at lower frequencies being characteristic of capacitive behavior.[123] Our impedance results indicate the x=1.49 sample operates in a much more capacitive mode than does the Co_3O_4 sample and the Mn-rich x=2.54 sample.

To model the impedance, suitable values for the corresponding equivalent circuit elements were fitted from the experimentally-observed frequency dependent spectra (inset of **Figure 6.6a**).[124]

The fitted values of the electrolyte resistance (R_e) were of the order of 10 Ohms and roughly the same for all the supercapacitors tested, hence we attribute this resistance value to the electrolyte and the coin cells configuration that was identical for all the cells. The R_{ct} values modelled for x=1.49, x=2.54, and x=0 (Co_3O_4) are 37.8, 92.5, and 218.7 Ω, respectively, indicating x=1.49 has a significantly lower barrier than the x=2.54 and Co_3O_4 electrode for charge transfer past the double layer. These EIS results show that the x=1.49 electrode exhibits faster charge transfer kinetics and better capacitive performance than the x=2.54 and Co_3O_4 electrodes.

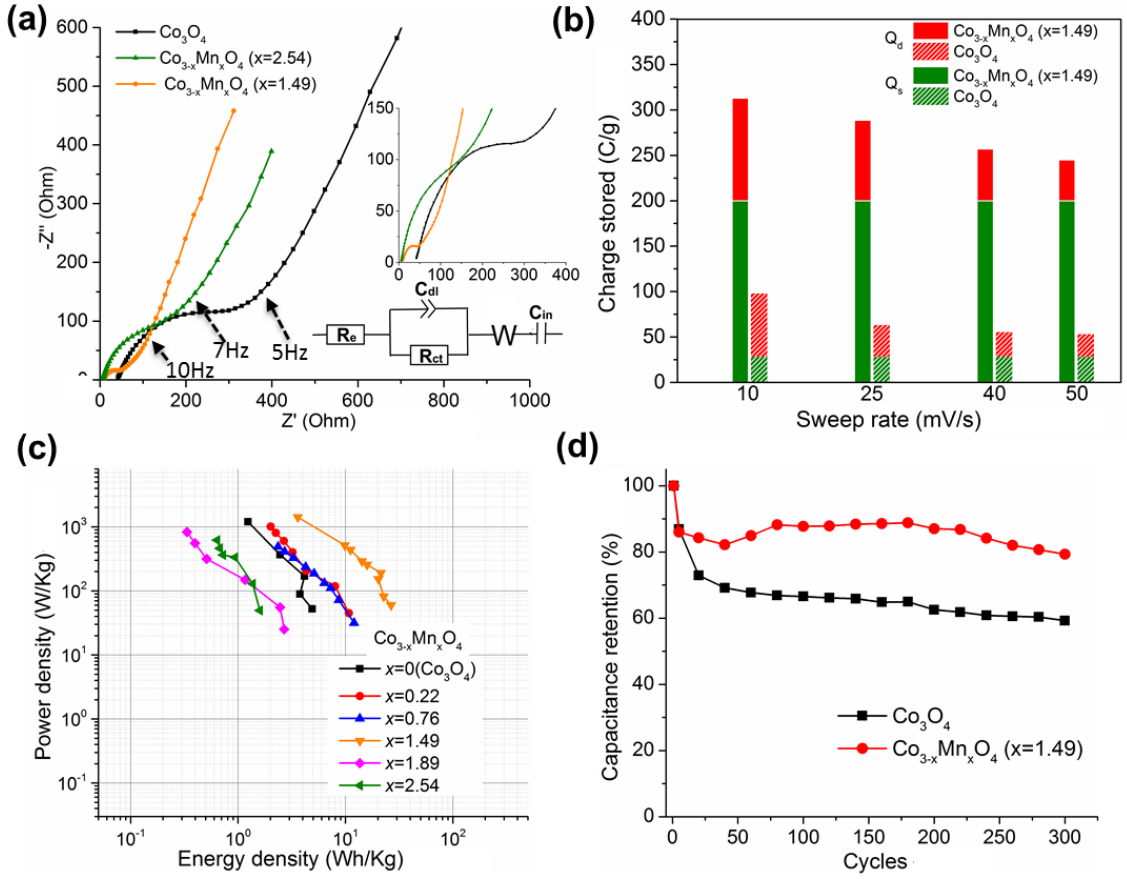

Figure 6.6. *(**a**) Comparison of Nyquist plots of electrodes with $Co_{3-x}Mn_xO_4$ composition x = 0, 1.49, and 2.54. Inset shows the modeled equivalent circuit. (**b**) Illustration of the contributions from the capacitive Q_s (green) and diffusion-controlled Q_d (red) charge to the total charge stored, at different sweep rates, for the x=0 and x=1.49 compositions. (Solid bars are x=1.49 and striped patterns are x=0, Co_3O_4). (**c**) Comparison of Ragone plots for $Co_{3-x}Mn_xO_4$ compositions. (**d**) Retention of capacitance as a function of cycles for the x=0 and x=1.49 electrodes. The cell was dis/charged at 0.25 A/g constant current over 300 cycles.*

To further understand the improved charge transfer kinetics of the *x*=1.49 electrode, the contributions of the capacitive and diffusion effects on the total charge was analyzed based on previous methods.[65,111] The total current response of the electrode as measured with CV depends on the surface capacitive charge (Q_s) and diffusion-controlled charge (Q_d). Q_s and Q_d contribute to the total volumetric charge response (Q_t) of the electrode according to equation (6.8):

$$Q_t = Q_s + Q_d \tag{6.8}$$

The capacitive charge contribution (Q_s) is mainly due to the charge generated at the electrode-electrolyte interface and is not expected to depend on sweep rate. Due to the faster charge transfer kinetics, Q_s can be considered as a combination of both faradaic supercapacitance and electric double layer capacitance,[111] while the diffusion charges Q_d are generated from redox reactions within the bulk and have slower kinetics compared to the capacitive charges. Semi-infinite linear diffusion is assumed for the diffusion processes of Q_d, and thus Q_d varies as the reciprocal square root of sweep rate (ν).[125] The outer charge, Q_s, should not depend on ν.[126] Cyclic voltammetry (CV) can be used to analyze these two charge components by measuring the dependence of the sweep rate and on total charge contribution (Q_t), following equation (6.9):[111]

$$Q_t = Q_s + k\nu^{-1/2} \tag{6.9}$$

where k is a constant. Thus, Q_s can be determined by plotting Q_t against the reciprocal of the square root of potential sweep rate ($\nu^{-1/2}$). The deviation of the linearity at high sweep rates is an indication of polarization effects (cell resistance) and is ignored in this equation.[111,127] The separate contributions from diffusion and capacitive charges to the total charge for four sweep rates are illustrated in **Figure 6.6b**, derived from analysis of the sweep rate dependence on total charge (**Figure 6.s7** and **Table 6.s5**). The solid bars represent the total charge contribution for each sweep

rate of the x=1.49 electrode, while cross-hatched bars represent the Co_3O_4 electrode. The total charge (each full vertical bar) is divided into the independent contribution of the diffusion controlled and capacitive controlled (red and green, respectively) capacities. The charge contribution analysis clearly shows that capacitive charge storage is the significant contribution for total charge storage for x=1.49 electrode in all sweep rates, while the Co_3O_4 electrode is mainly diffusion-charge dominated (**Figure 6.6b** and **Table 6.s5**). The contributions of capacitive processes at 10 mV/s for the x=1.49 electrode and the Co_3O_4 electrode are 63.8 % and 28.8%, respectively. The capacitive process of the x=1.49 electrode at 50 mV/s sweep rate contributes 81.5%, but in the case of Co_3O_4 contributes only 52.9 % (see **Table 6.s5** for details). Diffusion-controlled electrodes are known to exhibit slow charge transfer kinetics with slow movement of the ions in both electrode and electrolytes. Based on the diffusion and surface capacitive charge analysis for both x=1.49 and Co_3O_4, this is likely the cause of the low energy density, power density, and specific capacitance of the Co_3O_4 electrode. A significant contribution of capacitive charges from the x=1.49 particles is mainly due to the faradaic supercapacitance arising due to the Co and Mn mixed oxidation states and low charge transfer resistance.[128] Since it is common to add carbon materials (serving as electronic conduction paths) to nanoparticles in supercapacitor electrodes, it is surprising that, despite the absence of carbon in the x=1.49 electrode, the capacitive contribution of the x=1.49 electrode is high. We have previously shown that enhanced electronic carrier transport performance in NP electronics processed by EPD can be attributed to better inter-particle coupling.[97] It is likely that the enhanced carrier transport is aiding the performance of the electrode, beyond what would be expected in the absence of conductive carbon. We have also observed that EPD can be used to form additive-free high-performing catalyst electrodes[98] and Li-ion battery anode electrodes.[96] Our present observation now indicates that EPD can also be an

effective tool for creating high-performing supercapacitor electrodes with large capacitive contributions without the use of carbon additives.

Analysis of overall energy and power density performance over a range of constant current discharges provides the rate capability of the electrodes. **Figure 6.6c** shows the Ragone plot for $Co_{3-x}Mn_xO_4$ electrodes with different Co and Mn compositions. The plot shows that the x=1.49 cell delivers high energy and high power density while maintaining a much higher overall performance throughout a wide range of constant current discharge conditions. Based on the EIS data and the Ragone plot analysis, the x=1.49 electrode delivers the highest overall performance and further confirms the feasibility of x=1.49 as the ideal composition for a wide range of current densities. To evaluate the cycle performance of the x=1.49 electrode, the capacitance retention was calculated and plotted against the cycle number (**Figure 6.6d**). Compared to Co_3O_4, the x=1.49 material shows excellent stability over 300 charge-discharge cycles at a constant current of 0.25 A/g. The capacitance retention decreases in first 25 cycles for both electrodes. This may be due to the irreversible reactions before establishing the reversible cycling. Over 300 cycles the overall capacitance retention for the x=1.49 electrode was stable at above 80%, while capacitance retention of Co_3O_4 electrode slowly drops. This is a clear evidence for higher reversibility and the stability of x=1.49 material for long term cycling.

A comparison of the capacitive performance of these active materials has also been carried out using a three-electrode setup; these results are shown in **Figure 6.s8**. The results show the absence of well-defined faradaic peaks, and a similar trend of performance based on the Co-Mn ratio is observed (x=1.49 sample shows best performance). The three-electrode experiments show faradaic activities with tilted pseudo-rectangular curves, as opposed to the ideal pseudocapacitor profile of a rectangle (constant capacitance throughout the operating voltage window[72]). We note that the

differences in activities between the active material compositions are considerably reduced when the materials are tested in a three-electrode configuration, and the measured capacity of the electrodes is also reduced compared to the cells in the two-electrode configuration (see **Table 6.s6** in the supporting materials). This implies that there is an influence of the counter electrode in the two-electrode capacitor toward effecting a different electrochemical response. It has been shown, however, that large errors may result from extrapolating the charge storage capacity obtained from three-electrode measurements to working devices.[129] The geometries of the three- and two-electrode cells in this work also differ considerably. It is evident, however, that both three-electrode experiments and two-terminal device performances should be analyzed in order to fully evaluate a material's potential in supercapacitive applications (two-electrode), as well as its basic electrochemical behavior (three-electrode).[48]

To analyze the anomalous increase in supercapacitance performance for the x=1.49 sample, we examined the oxidation states through XPS. The $Co_{3-x}Mn_xO_4$ samples exhibit mixed oxidation states of Co and Mn, meaning the solid-state redox couples of Mn^{3+}/Mn^{2+} and Co^{3+}/Co^{2+} exist within the structure. The presence of these redox couples can generate much higher redox activity and improved electrochemical performance of $Co_{3-x}Mn_xO_4$.[128] **Figure 6.7 a**,**b,** and **c** show the Co 2p, Mn 2p and O 1s core level spectra, respectively of the x=1.49 NPs. The XPS spectrum of Co 2p, Mn 2p and O 1s were de-convoluted by Gaussian–Lorentzian curve fitting. Two distinct peaks at 779.9 eV and 795.1 eV can be attributed to the $2p_{3/2}$ and $2p_{1/2}$ of Co, respectively, and two broad satellite peaks occur at 785.6 and 803.5 eV (**Figure 6.7a**).[130,131] The two main peaks can be deconvoluted into the contributions of 3+ and 2+ ions.[132–134] The presence of both Co^{3+} and Co^{2+} confirms the Co_3O_4 phase in $Co_{3-x}Mn_xO_4$ NPs. The peaks centered at binding energies of 642.1 and 653.5 with the spin-orbit splitting of 11.4 eV correspond to Mn $2p_{3/2}$ and $2p_{1/2}$, respectively

(**Figure 6.7b**).[131] The de-convoluted Mn $2p_{3/2}$ spectrum consists of two small peaks centered at 641.2 eV and 643.2 eV, which correspond to Mn^{3+} and Mn^{2+}, respectively.[117] The XPS spectrum of O 1s core electrons shows two fitted peaks: one centered at 529.6 eV corresponds to oxides from Co and Mn oxides, and a broad peak at 531.5 eV is mainly due to hydroxyl groups of adsorbed water (**Figure 6.7c**).[131] The presence of more Co^{3+} and Mn^{3+} could explain a higher redox activity of the x=1.49 NP electrode; therefore, it is important to understand the relationships between stoichiometry, the oxidation states of the Co and Mn ions, and the resulting effect on electrochemical behavior of the $Co_{3-x}Mn_xO_4$. The ratios of Co^{3+}/Co^{2+} and Mn^{3+}/Mn^{2+} in our samples were obtained by de-convoluting the XPS spectra (**Table 6.2** and **Table 6.s2**).[135,136] Based on the XPS analysis, the x=1.49 sample has a nearly equal value for the Co^{3+}/Co^{2+} ratio and the Mn^{3+}/Mn^{2+} ratio, compared to the other samples. It is possible that these related values could point to some ideal mixing condition whereby a synergistic increase in performance results from a near-identical average valence for Co and Mn. With the large amount of both Co^{3+} and Mn^{3+}, more electrons can contribute in the redox process, thus resulting in higher energy storage capacity. More work is necessary to understand the extent of these effects.

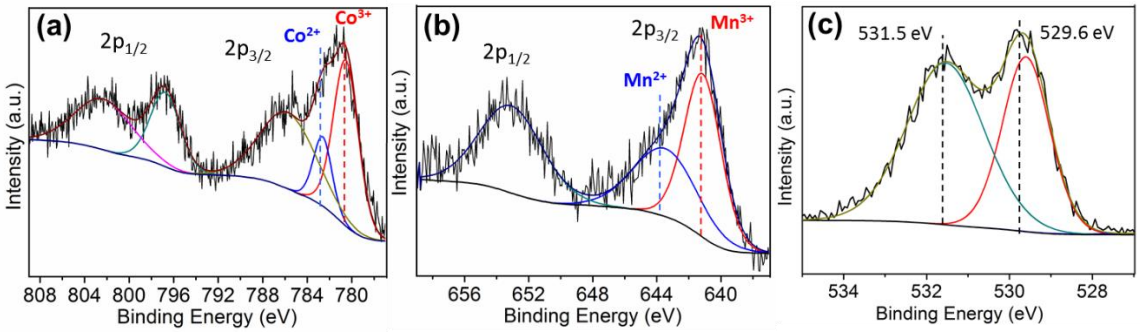

Figure 6.7. *X-ray photoelectron spectroscopy of the x=1.49 $Co_{3-x}Mn_xO_4$ sample: (**a**) Co 2p, (**b**) Mn 2p, and (**c**) O 1s core electrons. These spectra show that both Co and Mn are present in both the 2+ and 3+ oxidation states. The strong peak of O 1s corresponds to oxygen atoms in oxides and the broad peak corresponds to hydroxyl groups of adsorbed water.*

$Co_{3-x}Mn_xO_4$	Oxidation states ratios obtained from XPS	
	Co^{3+}/Co^{2+}	Mn^{3+}/Mn^{2+}
x=0.22	0.23	5.32
x=0.76	0.59	2.19
x=1.49	2.89	3.10
x=1.89	1.06	12.85
x=2.54	1.25	2.93

Table 6.2. *Oxidation state ratios obtained by de-convoluting XPS peaks corresponding to Co 2p and Mn 2p core electrons.*

Another possible contribution to the increased performance in the *x*=1.49 phase is an increased electronic conductivity. The electronic conductivity mechanisms in $Co_{3-x}Mn_xO_4$ have previously been found to be mediated by the hopping of polarons between cations with different oxidation states that sit on equivalent crystallographic sites.[114] These previous studies also found that the highest electronic conductivity occurs in $Co_{3-x}Mn_xO_4$ ($x\approx1.25$).[114] The conductivity greatly decreases with further increased Mn content: the conductivity for the $x\approx1.49$ composition is about 6 times greater than for the $x\approx1.89$ composition,[114] possibly explaining our observed rapid decline in supercapacitor performance with only a small increase in Mn content.

Under the influence of both factors described above, the highest performance sample should possess a high ratio of both Co^{3+}/Co^{2+} and Mn^{3+}/Mn^{2+} to enable the capture of more electrons in the redox activity when the 3+ cation reduces to the 2+ state. At the same time, the samples cannot be dominated by the 3+ cation because the Co^{3+}/Co^{2+} and Mn^{3+}/Mn^{2+} couples are responsible for

creating polaron hopping sites for transporting the electrons generated in the redox reactions. Based on the XPS oxidation states ratios data, the $Co_{3-x}Mn_xO_4$ (x=1.49) samples is the best fit towards these two criteria. This could be an explanation for the anomalous increase in the electrochemical performance of $Co_{3-x}Mn_xO_4$ (x=1.49). It should be noted that our work only presented six different compositions (including Co_3O_4) of $Co_{3-x}Mn_xO_4$. It is possible that even better performance can be achieved by finely tuning the x values in $Co_{3-x}Mn_xO_4$ around the range x=1.49.

6.5 Conclusion

In conclusion, we have developed a scalable hot-injection reaction for the synthesis of colloidal $Co_{3-x}Mn_xO_4$ nanoparticles (NP). The composition of the $Co_{3-x}Mn_xO_4$ NPs was controlled by varying the molar ratios of the Mn and Co carbonyl precursors. Carbon-free and *additive-free* NP electrodes were successfully prepared using electrophoretic deposition (EPD). A peak in supercapacitor performance occurs for the $Co_{3-x}Mn_xO_4$ (x=1.49) NP electrode: this composition displayed the highest specific capacitance of 173.6 F/g, energy density of 26.6 Wh/kg and power density of 3.8 kW/kg compared to all other chemical compositions. Moreover, supercapacitors fabricated at the x=1.49 composition exhibit more than ~80% capacitance retention over 300 charge-discharge cycles, while the capacitance retention of the Co_3O_4 electrodes steadily deteriorates to ~60%. Based on XPS analysis, we find that the highest Co^{3+}/Co^{2+} and Mn^{3+}/Mn^{2+} ratios occur for the x=1.49 composition, and these ratios are nearly equal between the Co and Mn metals. This interesting concurrence between the redox couples, along with previously reported increased conductivity around x=1.25, could be the cause for the increased supercapacitance for the x=1.49 composition. Overall, the reported facile method to synthesize colloidal $Co_{3-x}Mn_xO_4$

NPs and integrate them into *additive-free* electrodes through EPD shows promising potential for supercapacitor and battery applications.

Associated Content

Supporting Information. Further details on microscopy, ICP-MS, XPS, and supercapacitor performance evaluation, including 3-electrode experiments, and calculations. This information is available free of charge via the Internet at http://pubs.acs.org/.

Acknowledgements

This work was supported in part by the National Science Foundation (NSF) under award number CMMI-1344562 and CHE-1507753. R.H. and L.F.K. acknowledge support by the David and Lucile Packard Foundation. This work made use of the Cornell Center for Materials Research Shared Facilities, which are supported through the NSF MRSEC program (DMR-1120296). A.N. acknowledges the assistance of Yizhu Zhu in preparing several of the samples analyzed in the three-electrode experiments.

6.6 Supporting Information

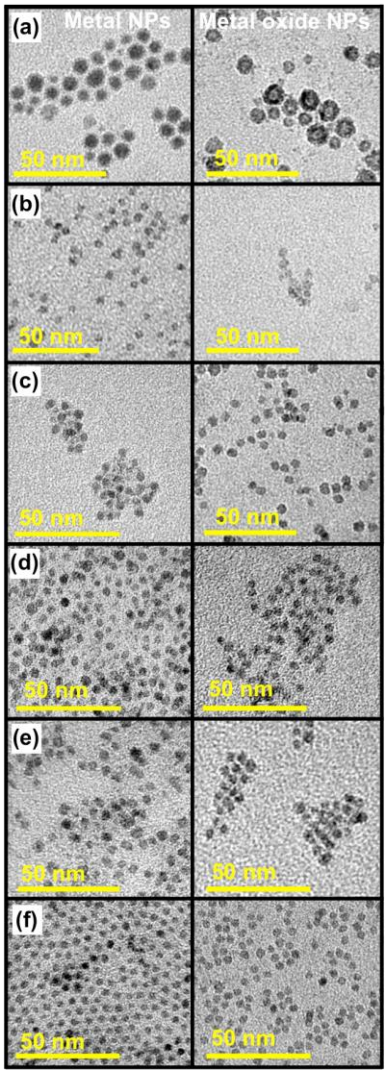

Figure 6.s1. *(a-e) TEM images of Co-Mn metal nanoparticles prepared through thermal decomposition of $Co_2(CO)_8$ and $Mn_2(CO)_{10}$. The Co:Mn precursor is varied to vary the final composition. The precursor molar ratios of a) 1:0 b) 1:0.25, c) 1:0.5, d) 1:1, e) 1:2 and f) 1:4. TEMs are taken after drop casting sample solutions onto TEM grids (metal NPs) and direct annealing of the same grids in air (metal oxide NPs).*

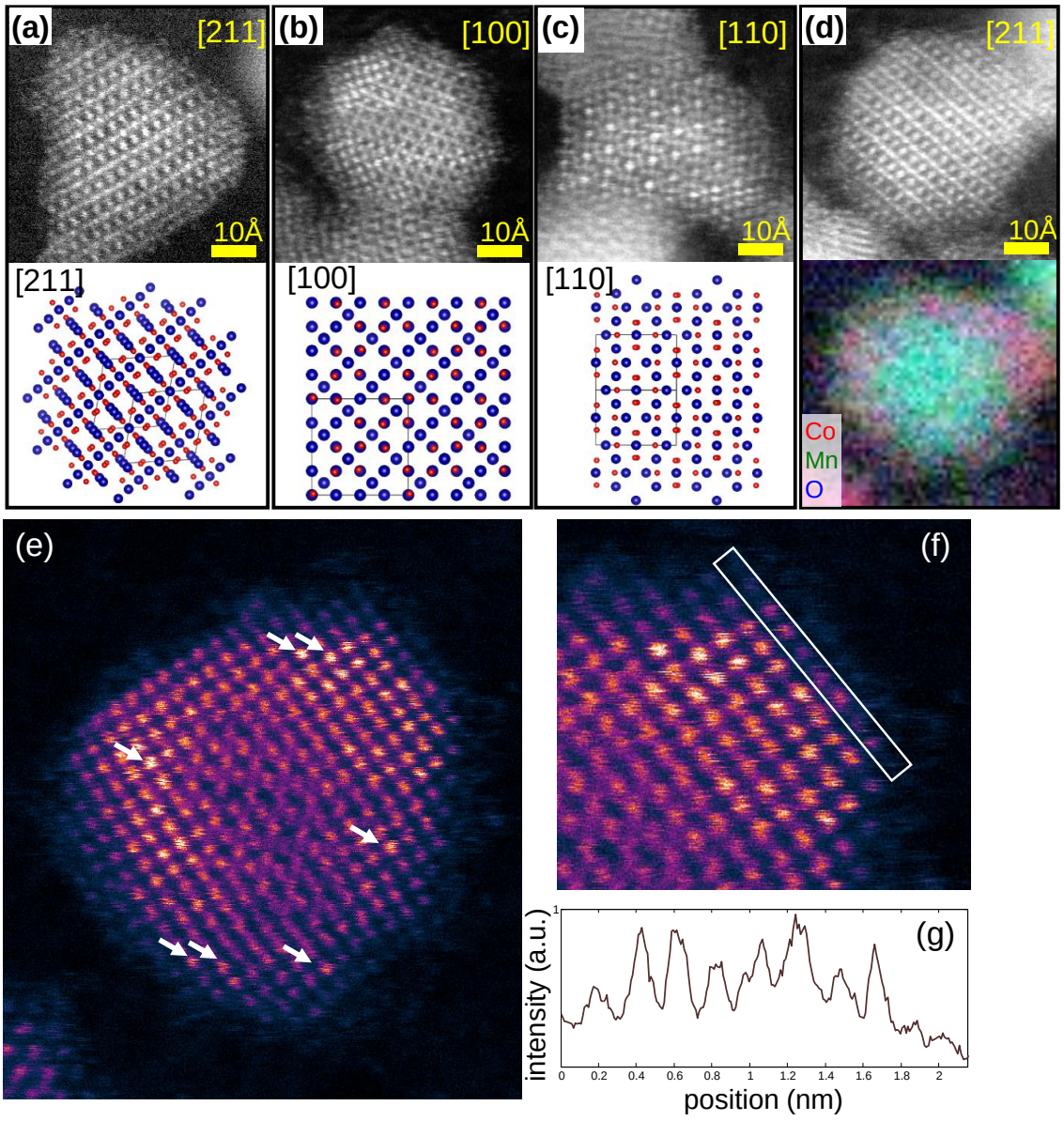

Figure 6.s2. ***(a), (b), (c)*** *HAADF STEM images of* $Co_{3-x}Mn_xO_4$ *(x=1.49) nanoparticles* ***(above)*** *and corresponding direction in the spinel lattice* ***(below). (d)*** *HAADF STEM image* ***(top)*** *and EELS elemental mapping* ***(bottom)*** *of a typical nanoparticle in the* $Co_{3-x}Mn_xO_4$ *(x=1.49) sample. (**e-f**) Annotated HAADF image of main text* ***Figure 6.2c*** *showing intermixing of heavy atoms (Co) in the shell. Some of the brighter atomic columns, representing a higher presence of Co, are marked with arrows (**e**). A line profile (**g**) taken across the surface atoms along a facet (**f**) shows variation in intensity between columns suggesting different amounts of Co present in each atomic column.*

Precursor ratio (Co:Mn)	Mean size and std. dev. of as-synthesized NP (nm)
1:0 (Co)	5.66 ± 2.21
1:0.25	2.79 ± 0.59
1:0.5	4.34 ± 0.71
1:1	3.87 ± 0.80
1:2	3.01 ± 0.49
1:4	3.05 ± 0.44

Table 6.s1. *Precursor ratios and sizes of as-synthesized Co-Mn metal nanoparticles.*

	Precursor ratio (Co:Mn)	ICP-MS analyzed ratio (Co:Mn)	ICP-MS calculated *x* values	Oxidation states ratios obtained from XPS	
				Co^{3+}:Co^{2+}	Mn^{3+}:Mn^{2+}
Co_3O_4	1:0	1:0	*x*=0	0.545	0
$Co_{3-x}Mn_xO_4$	1:0.25	1:0.077	*x*=0.22	0.23	5.32
	1:0.5	1:0.336	*x*=0.76	0.59	2.19
	1:1	1:1.008	*x*=1.49	2.89	3.10
	1:2	1:1.698	*x*=1.89	1.06	12.85
	1:4	1:5.650	*x*=2.54	1.25	2.93

Table 6.s2. *ICP-MS and XPS analysis of $Co_{3-x}Mn_xO_4$ samples. The ratios of oxidation states were obtained using the area under the curve of de-convoluted Co 2p and Mn 2p XPS spectra.*

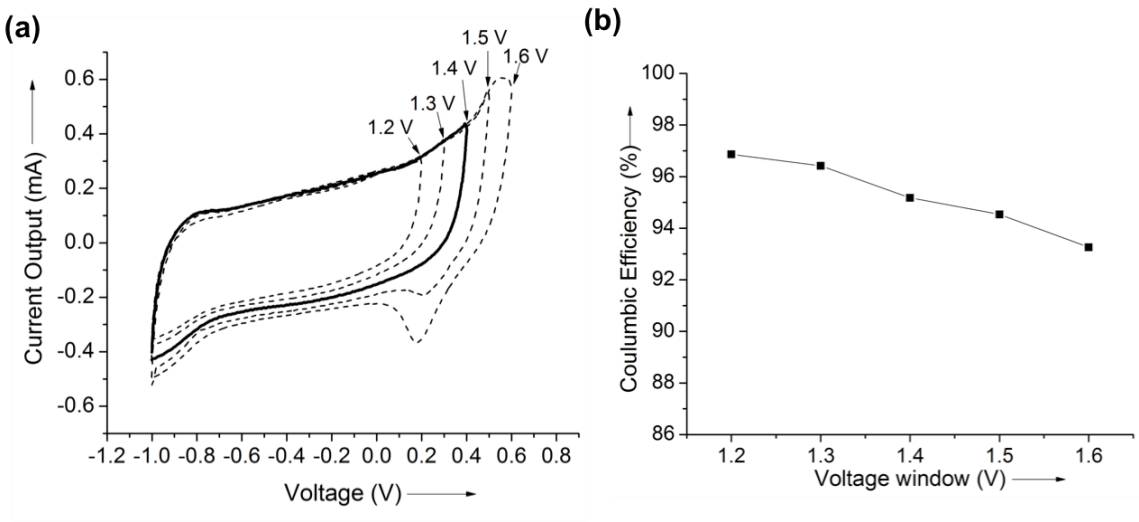

Figure 6.s3. ***a****) Cyclic voltammograms recorded at different voltage windows to optimize the working potential window.* ***b****) Dependence of coulombic efficiency with different voltage windows.*

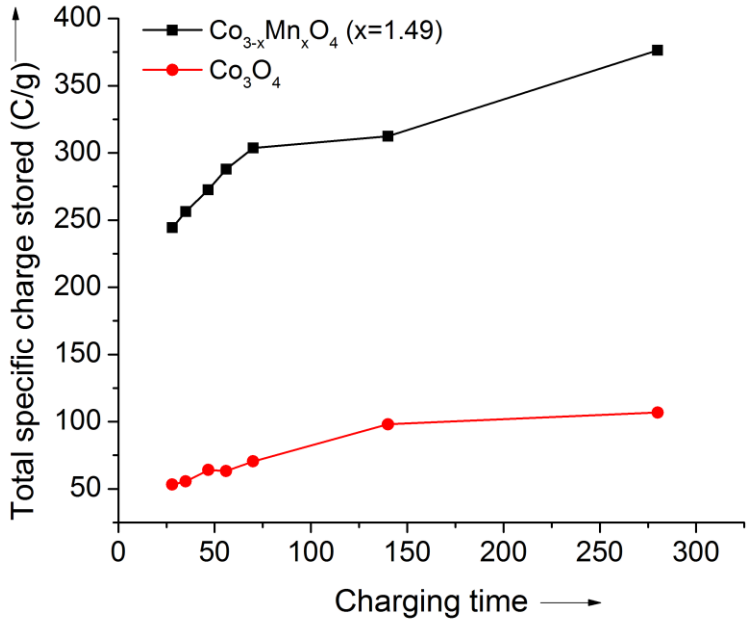

Figure 6.s4. *Kinetic behavior of $Co_{3-x}Mn_xO_4$ x=1.49 and x=0 (Co_3O_4) NP electrodes in -1.0 to 0.4 V voltage window. The charge/discharge time is between 28 and 280 s, which corresponds to the sweep rates from 5 to 50 mV/s.*

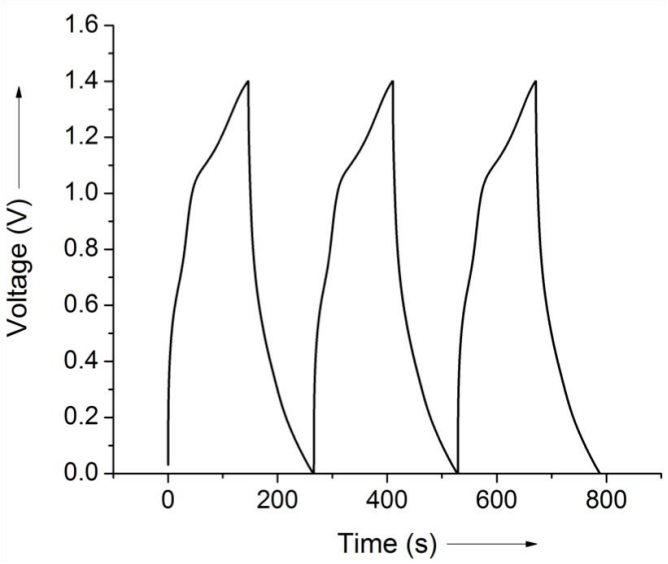

Figure 6.s5. *Cell voltage vs. charge and discharge time of an electrode having the x=1.49 composition, recorded at 1 A/g constant current density.*

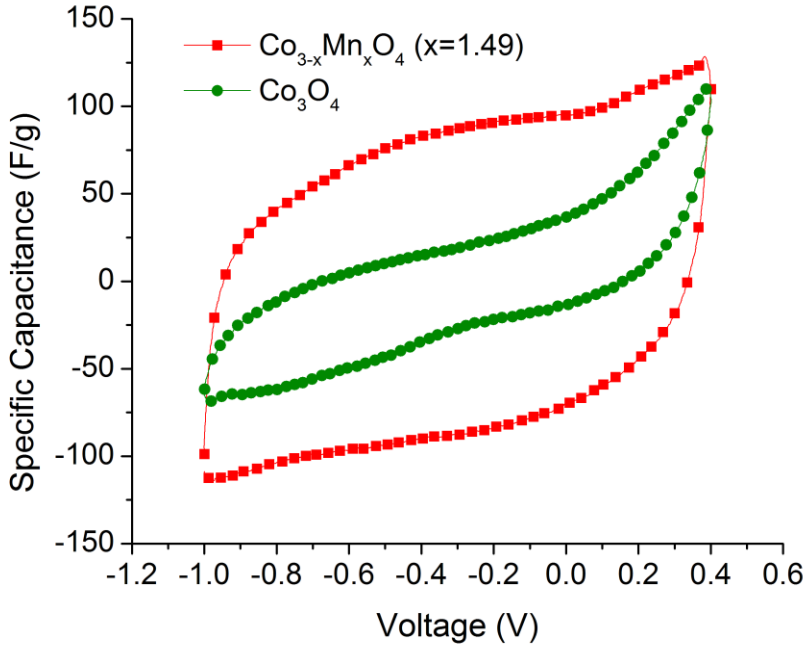

Figure 6.s6. *Specific capacitance response to voltage for $Co_{3-x}Mn_xO_4$, x=0 and x=1.49 electrodes at a scan rate of 25 mV/s.*

	I		II		III	
Sweep rates (mV/s)	Anodic (A/g)	Cathodic (A/g)	Anodic (A/g)	Cathodic (A/g)	Anodic (A/g)	Cathodic (A/g)
10	0.391	-0.362	0.690	-0.942	1.156	-1.151
25	0.790	-0.556	1.512	-2.346	2.698	-2.839
50	1.024	-0.324	2.281	-2.207	4.722	-5.101
	IV		V		VI	
Sweep rates (mV/s)	Anodic (A/g)	Cathodic (A/g)	Anodic (A/g)	Cathodic (A/g)	Anodic (A/g)	Cathodic (A/g)
10	0.948	-1.032	0.141	-0.220	0.143	-0.295
25	1.395	-1.701	0.089	-0.211	0.304	-0.530
50	3.216	-2.679	0.247	-0.255	0.549	-0.851

Table 6.s3. *Average anodic and cathodic current densities for Co_3O_4 and $Co_{3-x}Mn_xO_4$ with different compositions of $Co_{3-x}Mn_xO_4$: (I) x=0.22; (II) x=0.76; (III) x=1.49; (IV) x=1.89; (V) x=2.54, and (VI) x=0 (Co_3O_4) at 10, 25 and 50 mV/s sweep rates.*

	Energy density (Wh/Kg)	Power density (W/Kg)	Specific capacitance (F/g)
Co_3O_4	4.9	1200.0	36.2
$Co_{3-x}Mn_xO_4$ (x=0.22)	10.7	402.2	61.6
$Co_{3-x}Mn_xO_4$ (x=0.76)	12.0	492.3	98.9
$Co_{3-x}Mn_xO_4$ (x=1.49)	26.6	3848.0	173.6
$Co_{3-x}Mn_xO_4$ (x=1.89)	2.7	475.9	27.6
$Co_{3-x}Mn_xO_4$ (x=2.54)	1.6	334.5	8.3

Table 6.s4. *Comparison of energy density, power density and specific capacitance of $Co_{3-x}Mn_xO_4$ (x=0.22), $Co_{3-x}Mn_xO_4$ (x=0.76), $Co_{3-x}Mn_xO_4$ (x=1.49), $Co_{3-x}Mn_xO_4$ (x=1.89), $Co_{3-x}Mn_xO_4$ (x=2.54), which represents Co:Mn ratios of (x=0.22), (x=0.76), (x=1.49), (x=1.89) and (x=2.54) respectively. Energy and power density were calculated at constant current densities ranging from 0.1 A/g to 5.0 A/g. Energy density, power density and specific capacitance were normalized to the weight of the active electrode material, which is the total weight of electrode materials in our study since our active materials are additive-free.*

Sweep rate (mV/s)	Co_3O_4				$Co_{3-x}Mn_xO_4$ (x=1.49)			
	Q_s (C/g)	Q_s (%)	Q_d (C/g)	Q_d (%)	Q_s (C/g)	Q_s (%)	Q_d (C/g)	Q_d (%)
5	28.18	26.39	78.57	73.60	199.21	52.91	172.81	47.08
10	28.18	28.75	69.82	71.24	199.21	63.76	170.45	36.23
20	28.18	40.00	42.26	59.99	199.21	65.58	159.20	34.41
25	28.18	44.55	35.07	55.44	199.21	69.18	154.65	30.81
30	28.18	44.01	35.84	55.98	199.21	73.11	155.19	26.89
40	28.18	50.77	27.32	49.22	199.21	77.71	148.43	22.28
50	28.18	52.91	25.08	47.08	199.21	81.50	146.30	18.49

Table 6.s5. *Calculated values for Q_s and Q_d for Co_3O_4 and $Co_{3-x}Mn_xO_4$ (x=1.49) electrodes for different sweep rates. It is assumed that Q_s behaves linearly with the range of sweep rates.*

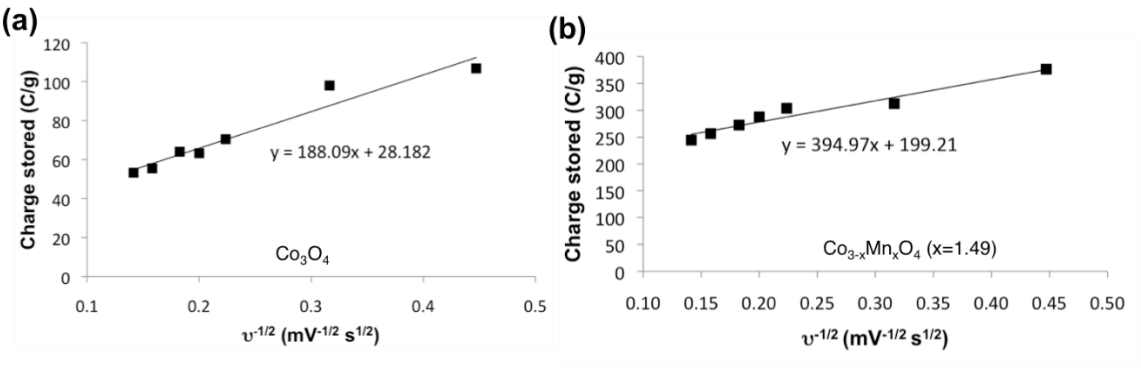

Figure 6.s7. *The plot of total gravimetric charge against the reciprocal of the square root of potential sweep rate for a) Co_3O_4 b) $Co_{3-x}Mn_xO_4$ (x=1.49) electrodes. Inset equations show the relationship between Q_t and Q_s according to equations (6.8) and (6.9).*

Three-electrode experiments

The voltammetric behavior of the $Co_{3-x}Mn_xO_4$ electrodes was also examined using a three-electrode configuration. An oxidized $Co_{3-x}Mn_xO_4$ working electrode was attached to a wire using silver epoxy (EPO-TEK H20E, Ted Pella Inc.) and placed in a hanging meniscus configuration by touching it to the surface of the 1M LiTFSI electrolyte. A piece of Li foil (Sigma-Aldrich) was used as a reference electrode, and a piece of carbon fiber paper served as the counter electrode. The glass cell was filled with electrolyte and assembled in a glove box, and it was isolated from the outside atmosphere during testing by maintaining a positive pressure of dry nitrogen inside the cell. The open-circuit potential of the as-assembled cell was consistently about 3.4 V vs Li/Li+, regardless of the film composition. The reference electrode was allowed to equilibrate by letting the cell stand for about an hour before beginning cycling. The stability window of this electrode was estimated to be about 1.1 V (from 2.4 to 3.5 V vs. Li/Li+) from preliminary cyclic voltammetric tests. This is comparable to the window in the two-electrode asymmetric capacitor. The electrodes were thereafter tested in this window by CVs at scan rates of 5, 10, 25, and 50 mV/s.

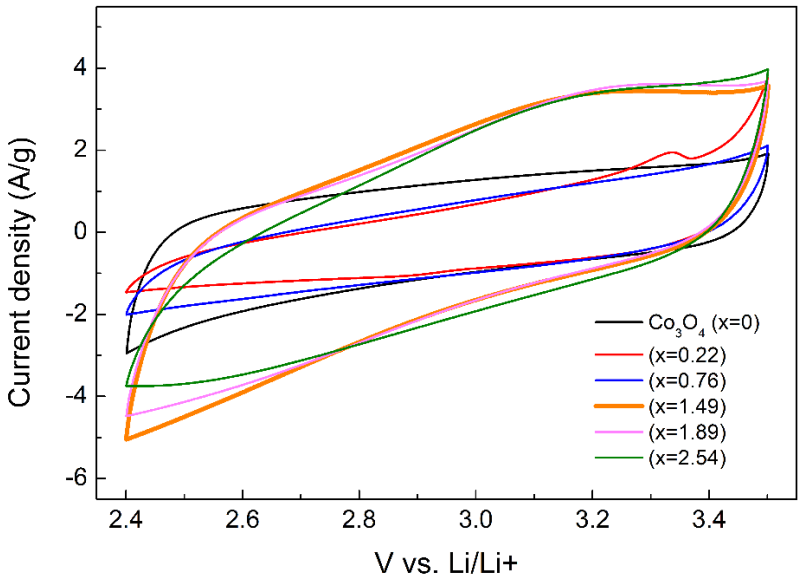

Figure 6.s8. *Cyclic voltammograms recorded in three-electrode experiments using a scan rate of 50 mV/s.*

	Specific capacitance (F/g)
Co_3O_4	43.3
$Co_{3-x}Mn_xO_4$ (x=0.22)	28.2
$Co_{3-x}Mn_xO_4$ (x=0.76)	30.7
$Co_{3-x}Mn_xO_4$ (x=1.49)	77.2
$Co_{3-x}Mn_xO_4$ (x=1.89)	75.2
$Co_{3-x}Mn_xO_4$ (x=2.54)	72.6

Table 6.s6. *Comparison of specific capacitances of $Co_{3-x}Mn_xO_4$ (x=0.22), $Co_{3-x}Mn_xO_4$ (x=0.76), $Co_{3-x}Mn_xO_4$ (x=1.49), $Co_{3-x}Mn_xO_4$ (x=1.89), and $Co_{3-x}Mn_xO_4$ (x=2.54) from three-electrode measurements. Specific capacitance were normalized to the weight of the active electrode material.*

Supporting Materials for Calculations

1) Energy density, power density and specific capacitance

Based on data from a voltage-vs-time (*V-t*) dis/charge curve with known dis/charge current, the formula for calculating energy density E, power density P and specific capacitance C_{sp} are:[45,137,138]

$$E = \int \frac{V \cdot I \cdot dt}{m} = \frac{I}{m} \cdot \int V \cdot dt = (Current\ density) \cdot (Area\ under\ discharge\ curve) \quad (6.s5)$$

$$P = \frac{E}{\Delta t} \quad (6.s6)$$

$$C_{sp} = \frac{I \cdot \Delta t}{\Delta V} \cdot \frac{1}{m} \quad (6.s7)$$

Where *V* is the voltage at time *t* in the dis/charge curve, ΔV and Δt are the voltage window and the time duration of the dis/charge curve, respectively, I is the current applied to the supercapacitor, and *m* is the mass of electrode materials.

When calculating the quantities above, we first measure and collect the dis/charge data as a function of various dis/charge currents. Then the voltage-vs-time information along with "area under discharge curve" can both be analyzed. Since the mass of electrode materials has already been measured, all quantities above can be found.

An example calculation is below:

We have a supercapacitor made from Co-Mn oxides with x=1.49 molar ratio. The mass of electrode materials is $m = 0.10\,\mathrm{mg}$. The current we use for charge-discharge process is $I = 0.015\,\mathrm{mA}$. Thus the current (mass) density is $i = \frac{I}{m} = 0.15\ A/g$. The voltage range is from 0 V to 1.4 V. We usually let the capacitor charge and discharge for 3-4 cycles to let the electrochemical process stabilize. The discharge curve of the 3rd cycle was used for our calculation.

At the beginning of each discharge, there is always a small IR voltage drop due to intrinsic resistance. The IR drop has very little contribution towards the device's capacitance. All data taken for calculation is after the initial IR drop. Discharge voltage window is recorded as 1.38 V. The time duration it takes is 1597.5 seconds. The area below the discharge curve is calculated as 637.2 V·s . Therefore, based on equation (6.5), the energy density is calculated as

$$E = 0.15\frac{A}{g} \cdot 637.2\ V \cdot s = 95.58\ W \cdot \frac{s}{g} = 26.55\ W \cdot h/kg$$

The average power density P from equation (6.6) is $P = \frac{E}{\Delta t} = \frac{95.58\ W \cdot \frac{s}{g}}{1597.5\ s} = 59.83\frac{W}{kg}$.

The specific capacitance C from equation (6.7) is $C = \frac{0.15\frac{A}{g} \cdot 1597.5\ s}{1.38\ V} = 173.64\frac{F}{g}$.

Calculation of energy density, power density and specific capacitance for other devices all follow the same procedure demonstrated above.

2) Surface capacitive charge vs diffusion controlled charge

The total voltametric charge Q_t is composed of two different parts: surface charge *Qs* with fast kinetics, including both electrical double-layer charge and faradaic redox-activity induced charge, as well as diffusion controlled charge Q_d with slow kinetics, typically intercalation of ions into electrode materials layers.

$$Q_t = Q_s + Q_d \qquad \text{(6.s8)}$$

With the assumption of semi-infinite linear diffusion[4], Q_t varies as the inverse of the square root of voltage scan rate:

$$Q_t = Q_s + Const \cdot \frac{1}{\sqrt{v}} \tag{6.s9}$$

In this model, Q_s is assumed to be independent of scan rate, when our scan rate is low. Higher scan rates can deviate the equation from linearity. That is an indication of polarization, which is not considered in this model.[111] With a preset voltage scan rate *v* (V/s), the total capacitive charg e Q_t can be found as:

$$Q_t = \int I \cdot dt = \int I \cdot \frac{dV}{v} = \frac{Area\ under\ CV\ curve}{Voltage\ scan\ rate} \tag{6.s1}$$

Therefore, if we plot different Q_t versus different scan rates *v*, both Q_s and *Const* can be obtained through linear curve fitting and extrapolation. Then Q_d can be found as

$$Q_s(v) = Const \cdot \frac{1}{\sqrt{v}} = Q_t(v) - Q_s \tag{6.s2}$$

An example of calculation is demonstrated below:

A coin-cell type supercapacitor was fabricated using Co-Mn oxides with x=1.49 molar ratio. Current-voltage (CV) curves were taken under different voltage scan rates. At a scan rate of 10 mV/s, the total capacitive charge Q_t calculated from equation (6.s1) is to be 312.39 C/g. At 25 V/s, $Q_t = 287.92\ C/g$. At 50 mV/g, $Q_t = 244.40\ C/g$. Q_t at other sweep rates are also calculated. These results are then plotted against the inverse of $\sqrt{v}$. A linear fitting is then performed, as shown in **Figure 6.s6b**.

The parameters are extrapolated and the *Qs*, which are just the intercept on y-axis, can be obtained as 199.21 C/g. Then the scan-rate-dependent diffusion charge is just $Q_d(v) = Q_t(v) - Q_s$. Final results are shown in **Figure 6.5b**, where the total charges at different scan rates are represented by the overall bars, while the red and green parts represent diffusion controlled charge and surface capacitive charges, respectively.

3) Coulombic Efficiency

We used the charge-discharge curve to calculate the coulombic efficiency. The formula is shown below:

$$Columbic\ Efficiency = \frac{Charge\ released\ during\ discharging}{Charge\ released\ during\ charging} = \frac{I_{discharge} \cdot t_{discharge}}{I_{charge} \cdot t_{charge}} \qquad (6.s2)$$

Where t_{charge} and $t_{discharge}$ are the time duration of charging and discharging; I_{charge} and $I_{discharge}$ are the charging and discharging current, which are equal to each other in our constant-current charge-discharge. Therefore, the coulombic efficiency is:

$$Columbic\ Efficiency = \frac{t_{discharge}}{t_{charge}} \qquad (6.s3)$$

Results for coulombic efficiency are shown in **Figure 6.s2b**.

Supporting Materials for Electrochemical impedance spectroscopy

Analysis of the electrode/electrolyte interface was conducted via electrochemical impedance spectroscopy (EIS) using a Bio-Logic VMP3 multi-potentiostat. EIS was carried out in potentiostatic mode at a fixed bias voltage of 0.45V and kept under equilibrium for 60 minutes before measurement. A small AC current was passed and the AC voltage response was measured. The Nyquist plot shows the imaginary part of impedance vs real impedance, with the Y-axis in negative and each point on the plot represents the impedance at a given frequency.

In the high frequency region, the intercept of semicircle provides the value corresponding to the combination of ionic resistance (R_e) of electrolyte, contact resistance at interface of current collector/active material. The semicircle for both electrodes apparent in the high frequency region (f > 100Hz) is due to the presence of the electric double layer. The double layer acts as a parallel circuit with the ions present at the electrode interface either 1) accumulating and contributing to the double layer capacitance (C_{dl}) or 2) crossing the electrode interface under a charge transfer resistance R_{ct}.[139,140] The charge transfer resistance defines the ease with which charges can cross the double layer barrier and move inside the active material, leading to the passage of faradaic current.

In the mid-frequency region of 100Hz to 20Hz, the Warburg diffusion (W) shows a straight line with a slope of ~ 45˚, representing the resistive and capacitive behavior of ions diffusing inside the pores of the electrode.[141] In the capacitive region the ion transport into the micro-pores of the material is fast and double-layer systems form.[141,142] The "knee frequency" is the maximum frequency for capacitive behavior; capacitive behavior is predominant for frequencies below the knee frequency. This knee frequency is associated with the relaxation time of the cell and indicates the rate at which stored energy can be accessed and how fast the cell can be charged and

discharged.[123] For a capacitive material, the stored energy is not fully available above this frequency, as the higher rate of polarization change does not allow the ions to fully penetrate the pores inside the electrode, hence a high knee frequency is desirable for capacitor applications.[143]

To calculate the model parameters, a least-squares fitting method was applied with the objective of minimizing the deviations between the observed and modeled spectra. The circuit elements (inset of **Figure 6.5a**) can be individually modeled from the experimentally-observed frequency dependent spectra.[124] R_e corresponds to the ohmic resistance, R_{ct} is charge transfer resistance, C_{dl} is the double layer capacitance at the electrode-electrolyte interface, W corresponds to the Warburg impedance, and C_{int} is the intercalation capacitance.

Chapter 7. Future Work

7.1 Oxidation of Fe NPs

Although the report discusses the local structure of the core and shell, further work needs to be done to study the diffusions mechanisms involved. Further, experimental conditions need to be refined so as to prevent complete oxidation of Fe NPs and partially oxidized particles can be analyzed.

7.2 $Co_{3-x}Mn_xO_4$ supercapacitors

Further work needs to be carried out to explain the anomalous increase in performance of 1:1 samples. We have started a comprehensive study of the structure of these materials using synchrotron based x-ray diffraction and x-ray absorption spectroscopy. The site occupation of Co and Mn atoms at octahedral and tetrahedral locations might provide an insight into the performance of these materials in supercapacitors. Besides, understanding of the mechanism of formation of these nanoparticles could be employed for synthesis of tailor-made composition of other transition metals for use in redox active devices.

References

1. Ghasemi, E., Mirhabibi, A. & Edrissi, M. Synthesis and rheological properties of an iron oxide ferrofluid. *J. Magn. Magn. Mater.* **320,** 2635–2639 (2008).

2. Babes, L., Denizot, B., Tanguy, G., Le Jeune, J. J. & Jallet, P. Synthesis of Iron Oxide Nanoparticles Used as MRI Contrast Agents: A Parametric Study. *J. Colloid Interface Sci.* **212,** 474–482 (1999).

3. Koo, B. *et al.* Hollow iron oxide nanoparticles for application in lithium ion batteries. *Nano Lett.* **12,** 2429–2435 (2012).

4. Rolison, D. R. & Nazar, L. F. Electrochemical energy storage to power the 21st century. *MRS Bull.* **36,** 486–493 (2011).

5. Macdonald, J. E. & Veinot, J. G. C. Removal of residual metal catalysts with iron/iron oxide nanoparticles from coordinating environments. *Langmuir* **24,** 7169–7177 (2008).

6. Wu, W., He, Q. & Jiang, C. Magnetic iron oxide nanoparticles: Synthesis and surface functionalization strategies. *Nanoscale Res. Lett.* **3,** 397–415 (2008).

7. Peng, S. & Sun, S. Synthesis and characterization of monodisperse hollow Fe3O 4 nanoparticles. *Angew. Chemie - Int. Ed.* **46,** 4155–4158 (2007).

8. Signorini, L. *et al.* Size-dependent oxidation in iron/iron oxide core-shell nanoparticles. *Phys. Rev. B* **68,** 195423 (2003).

9. Wagner, C. Equations for transport in solid oxides and sulfides of transition metals. *Prog. Solid State Chem.* **10,** 3–16 (1975).

10. Chen, L. X., Liu, T., Thurnauer, M. C., Csencsits, R. & Rajh, T. Fe 2 O 3 Nanoparticle Structures Investigated by X-ray Absorption Near-Edge Structure, Surface Modifications, and Model Calculations. *J. Phys. Chem. B* **106,** 8539–8546 (2002).

11. Powers, L. *et al.* The nature of the copper atoms of cytocrhome c oxidase as studied by optical and X-ray absorption edge spectroscopy. *Biochim. Biophys. Acta* **546,** 520–538 (1979).

12. Filipponi, A., Cicco, A. Di & Madonna, V. the, 52. **52,** 122–134 (1995).

13. Mansour, a. N., Cook, J. W. & Sayers, D. E. Quantitative technique for the determination of the number of unoccupied d-electron states in a platinum catalyst using the L2,3 x-ray absorption edge spectra. *J. Phys. Chem.* **88,** 2330–2334 (1984).

14. Toshima, N., Harada, M., Yonezawa, T., Kushibashi, K. & Asakurat, K. Structural Analysis of Polymer-Protected Pd/Pt Blmetalllc Clusters as Dispersed Catalysts by Using Extended X-ray Absorption Fine Structure Spectroscopy. *J. Phys. Chem.* **95,** 7448–7453 (1991).

15. Kim, C. S., Brown, G. E. & Rytuba, J. J. Characterization and speciation of mercury-bearing mine wastes using X-ray absorption spectroscopy. *Sci. Total Environ.* **261,** 157–168 (2000).

16. Waldo, G. S., Carlson, R. M. K., Moldowan, J. M., Peters, K. E. & Penner-hahn, J. E. Sulfur speciation in heavy petroleums: Information from X-ray absorption near-edge structure. *Geochim. Cosmochim. Acta* **55,** 801–814 (1991).

17. Zhao, M. & Crooks, R. Homogeneous hydrogenation catalysis with monodisperse, dendrimer-

encapsulated Pd and Pt nanoparticles. *Angew. Chem. Int. Ed. Engl.* **38,** 364–366 (1999).

18. Narayanan, R. & El-Sayed, M. a. Catalysis with Transition Metal Nanoparticles of Different Shapes. *MRS Proc.* **900,** 12663–12676 (2005).

19. Adam D. McFarland, R. P. V. D. Single Silver Nanoparticles As Real Time Optical Sensors With Zeptomole Sensitivity. *Nano Lett.* **3,** 1057–1062. (2003).

20. Luo, X., Morrin, A., Killard, A. J. & Smyth, M. R. Application of nanoparticles in electrochemical sensors and biosensors. *Electroanalysis* **18,** 319–326 (2006).

21. Robel, I., Kuno, M. & Kamat, P. V. Size-Dependent Electron Injection from Excited CdSe Quantum Dots into TiO 2 Nanoparticles. *J. Am. Chem. Soc.* **129,** 4136–4137 (2007).

22. Yi, D. K. *et al.* Silica-Coated Nanocomposites of Magnetic Nanoparticles and Quantum Dots Silica-Coated Nanocomposites of Magnetic Nanoparticles and Quantum Dots. 4990–4991 (2005). doi:10.1021/ja0428863

23. Jagadeesh, R. V. *et al.* Nitroarenes to Anilines. *Science (80-.).* **342,** 1073–1076 (2013).

24. Panella, B., Vargas, A. & Baiker, A. Magnetically separable Pt catalyst for asymmetric hydrogenation. *J. Catal.* **261,** 88–93 (2009).

25. Newville, M. Fundamentals of XAFS. *ReVision* 43 (2004). doi:10.2138/rmg.2014.78.2

26. Calvin, S. *XAFS for Everyone*. (CRC press, 2013).

27. Newville, M., Livi??, P., Yacoby, Y., Rehr, J. J. & Stern, E. A. Near-edge x-ray-absorption fine structure of Pb: A comparison of theory and experiment. *Phys. Rev. B* **47,** 14126–14131 (1993).

28. Ravel, B. & Newville, M. ATHENA, ARTEMIS, HEPHAESTUS: Data analysis for X-ray absorption spectroscopy using IFEFFIT. *J. Synchrotron Radiat.* **12,** 537–541 (2005).

29. Zabinsky, S. I., Rehr, J. J., Ankudinov, A., Albers, R. C. & Eller, M. J. Multiple-scattering calculations of x-ray-absorption spectra. *Phys. Rev. B* **52,** 2995–3009 (1995).

30. Ankudinov, a. L., Rehr, J. J. & Conradson, S. D. Real-space multiple-scattering calculation and interpretation of x-ray-absorption near-edge structure. *Phys. Rev. B* **58,** 7565–7576 (1998).

31. Ravel, B. ATOMS: Crystallography for the X-ray absorption spectroscopist. *J. Synchrotron Radiat.* **8,** 314–316 (2001).

32. Cruz, S. S ,. **52,** (1995).

33. Belkly, A., Helderman, M., Karen, V. L. & Ulkch, P. New developments in the Inorganic Crystal Structure Database (ICSD): Accessibility in support of materials research and design. *Acta Crystallogr. Sect. B Struct. Sci.* **58,** 364–369 (2002).

34. Newville, M. The Atoms. inp Archive. (2001). at <http://cars.uchicago.edu/~newville/adb/search.html>

35. Ha, D.-H. *et al.* The structural evolution and diffusion during the chemical transformation from cobalt to cobalt phosphide nanoparticles. *J. Mater. Chem.* **21,** 11498–11510 (2011).

36. Nelson, A. *et al.* Increased activity in hydrogen evolution electrocatalysis for partial anionic

substitution in cobalt oxysul fi de nanoparticles †. *J. Mater. Chem. A Mater. energy Sustain.* **4,** 2842–2848 (2016).

37. Cabrera, N., and N. F. M. Theory of the oxidation of metals. *WORLD Sci. Ser. 20TH CENTURY Phys.* **12,** 185–208 (1995).

38. Wang, C. M. *et al.* Void formation during early stages of passivation: Initial oxidation of iron nanoparticles at room temperature. *J. Appl. Phys.* **98,** (2005).

39. Oxidation of nanometer-sized iron particles V ’ r ’ l ~ ,: *J. Mater.* **311,** 3142–3148 (1995).

40. Fung, K. K., Qin, B. & Zhang, X. X. Passivation of ??-Fe nanoparticle by epitaxial ??-Fe2O3 shell. *Mater. Sci. Eng. A* **286,** 135–138 (2000).

41. Leibbrandt, G. W. R., Hoogers, G. & Habraken, F. H. P. M. Thin Oxide Film Growth on Fe (lOO). **68,** 1947–1950 (1992).

42. Yin, Y. D. *et al.* Formation of Hollow Nanocrystals through the Nanoscale Kirkendall Effect. *Science (80-.).* **304,** 711–714 (2004).

43. Cabot, a. *et al.* Vacancy Coalescence During Oxidation of Iron Nanoparticles - Supporting Information. *J. Am. Chem. Soc* **129,** 10358–10360 (2007).

44. Yao, Y., Hu, Y. & Scott, R. W. J. Watching Iron Nanoparticles Rust: An In Situ X-ray Absorption Spectroscopic Study. *J. Phys. Chem. C* 140828200553009 (2014). doi:10.1021/jp506281d

45. Simon, P. & Gogotsi, Y. Materials for electrochemical capacitors. *Nat. Mater.* **7,** 845–854 (2008).

46. Conway, B. *Electrochemical Supercapacitor. In Scientific Fundamentals and Technological Applications*. (Kluwer Academic/Plenum Publishers: New York, 1999).

47. Miller, J. R. & Simon, P. Electrochemical Capacitors for Energy Management. **321,** 651–652 (2008).

48. Brousse, T., Belanger, D. & Long, J. W. To Be or Not To Be Pseudocapacitive? *J. Electrochem. Soc.* **162,** A5185–A5189 (2015).

49. Perera, S. D. *et al.* Vanadium oxide nanowire-Graphene binder free nanocomposite paper electrodes for supercapacitors: A facile green approach. *J. Power Sources* **230,** 130–137 (2013).

50. Gittleson, F. S., Hwang, J., Sekol, R. C. & Taylor, A. D. Polymer coating of vanadium oxide nanowires to improve cathodic capacity in lithium batteries. *J. Mater. Chem. A* **1,** 7979 (2013).

51. Zheng, J. P. The Limitations of Energy Density for Electrochemical Capacitors. *J. Electrochem. Soc.* **144,** 2026 (1997).

52. Zhang, Y. *et al.* Progress of electrochemical capacitor electrode materials: A review. *Int. J. Hydrogen Energy* **34,** 4889–4899 (2009).

53. Frackowiak, E. Carbon materials for supercapacitor application. *Phys. Chem. Chem. Phys.* **9,** 1774–1785 (2007).

54. Kosmulski, M., Próchniak, P. & Saneluta, C. Quantitative assessment of hysteresis in voltammetric curves of electrochemical capacitors. *Adsorption* **15,** 172–180 (2009).

55. Kalaji, M. & Murphy, P. J. The study of Conducting Polymers for use as Redox Supercapacitors. **102,** 0–1 (1999).

56. Zhou, Y. K. *et al.* Electrochemical capacitance of well-coated single-walled carbon nanotube with polyaniline composites. *Electrochim. Acta* **49,** 257–262 (2004).

57. Gupta, V. & Miura, N. High performance electrochemical supercapacitor from electrochemically synthesized nanostructured polyaniline. *Mater. Lett.* **60,** 1466–1469 (2006).

58. Fan, L. Z. *et al.* High electroactivity of polyaniline in supercapacitors by using a hierarchically porous carbon monolith as a support. *Adv. Funct. Mater.* **17,** 3083–3087 (2007).

59. Talbi, H., Just, P. E. & Dao, L. H. Electropolymerization of aniline on carbonized polyacrylonitrile aerogel electrodes: Applications for supercapacitors. *J. Appl. Electrochem.* **33,** 465–473 (2003).

60. Lee, H., Cho, M. S., Kim, I. H., Nam, J. Do & Lee, Y. RuOx/polypyrrole nanocomposite electrode for electrochemical capacitors. *Synth. Met.* **160,** 1055–1059 (2010).

61. Kim, I.-H. & Kim, K.-B. Electrochemical Characterization of Hydrous Ruthenium Oxide Thin-Film Electrodes for Electrochemical Capacitor Applications. *J. Electrochem. Soc.* **153,** A383 (2006).

62. Pang, S. C., Anderson, M. A. & Chapman, T. W. Novel electrode materials for thin-film ultracapacitors: Comparison of electrochemical properties of sol-gel-derived and electrodeposited manganese dioxide. *J. Electrochem. Soc.* **147,** 444–450 (2000).

63. Zhang, S. W. & Chen, G. Z. Manganese oxide based materials for supercapacitors. *Energy Mater. Mater. Sci. Eng. Energy Syst.* **3,** 186–200 (2008).

64. Donne, S. W., Hollenkamp, A. F. & Jones, B. C. Structure, morphology and electrochemical behaviour of manganese oxides prepared by controlled decomposition of permanganate. *J. Power Sources* **195,** 367–373 (2010).

65. Perera, S. D. *et al.* Manganese oxide nanorod-graphene/vanadium oxide nanowire-graphene binder-free paper electrodes for metal oxide hybrid supercapacitors. *Nano Energy* **2,** 966–975 (2013).

66. Lokhande, C. D., Dubal, D. P. & Joo, O. S. Metal oxide thin film based supercapacitors. *Curr. Appl. Phys.* **11,** 255–270 (2011).

67. Reddy, M. V, Prithvi, G., Loh, K. P. & Chowdari, B. V. R. Li storage and impedance spectroscopy studies on Co3O4, CoO, and CoN for Li-ion batteries. *ACS Appl. Mater. Interfaces* **6,** 680–90 (2014).

68. Gupta, V., Gupta, S. & Miura, N. Al-substituted ??-cobalt hydroxide synthesized by potentiostatic deposition method as an electrode material for redox-supercapacitors. *J. Power Sources* **177,** 685–689 (2008).

69. Zhou, W. J., Xu, M. W., Zhao, D. D., Xu, C. L. & Li, H. L. Electrodeposition and characterization of ordered mesoporous cobalt hydroxide films on different substrates for supercapacitors. *Microporous Mesoporous Mater.* **117,** 55–60 (2009).

70. Inamdar, A. I. *et al.* Chemically grown, porous, nickel oxide thin-film for electrochemical supercapacitors. *J. Power Sources* **196,** 2393–2397 (2011).

71. Zhao, D. D., Bao, S. J., Zhou, W. J. & Li, H. L. Preparation of hexagonal nanoporous nickel hydroxide film and its application for electrochemical capacitor. *Electrochem. commun.* **9,** 869–874 (2007).

72. Perera, S. D. *et al.* Vanadium oxide nanowire-carbon nanotube binder-free flexible electrodes for supercapacitors. *Adv. Energy Mater.* **1,** 936–945 (2011).

73. Dong, W. Electrochemical Properties of High Surface Area Vanadium Oxide Aerogels. *Electrochem. Solid-State Lett.* **3,** 457 (1999).

74. Hwang, S. W. & Hyun, S. H. Synthesis and characterization of tin oxide/carbon aerogel composite electrodes for electrochemical supercapacitors. *J. Power Sources* **172,** 451–459 (2007).

75. Zhao, X., Johnston, C. & Grant, P. S. A novel hybrid supercapacitor with a carbon nanotube cathode and an iron oxide/carbon nanotube composite anode. *J. Mater. Chem.* **19,** 8755 (2009).

76. Kulesza, P. J. *et al.* Spectroelectrochemical characterization of cobalt hexacyanoferrate films in potassium salt electrolyte. *Electrochim. Acta* **43,** 919–923 (1998).

77. Xun, Z., Cai, C., Xing, W. & Lu, T. Electrocatalytic oxidation of dopamine at a cobalt hexacyanoferrate modified glassy carbon electrode prepared by a new method. *J. Electroanal. Chem.* **545,** 19–27 (2003).

78. Srinivasan, V. & Weidner, J. W. Capacitance studies of cobalt oxide films formed via electrochemical precipitation. *J. Power Sources* **108,** 15–20 (2002).

79. Kim, H. K., Seong, T. Y., Lim, J. H., Cho, W. & Soo Yoon, Y. Electrochemical and structural properties of radio frequency sputtered cobalt oxide electrodes for thin-film supercapacitors. *J. Power Sources* **102,** 167–171 (2001).

80. Wu, Z. *et al.* Graphene Anchored with Co 3 O 4 Nanoparticles as Anode of Lithium Ion Capacity and Cyclic Performance. *ACS Nano* **4,** 3187–3194 (2010).

81. Xu, P. *et al.* Facile synthesis of cobalt manganese oxides nanowires on nickel foam with superior electrochemical performance. *J. Power Sources* **268,** 204–211 (2014).

82. Kandalkar, S. G., Dhawale, D. S., Kim, C.-K. & Lokhande, C. D. Chemical synthesis of cobalt oxide thin film electrode for supercapacitor application. *Synth. Met.* **160,** 1299–1302 (2010).

83. Wang, G. *et al.* Hydrothermal Synthesis and Optical, Magnetic, and Supercapacitance Properties of Nanoporous Cobalt Oxide Nanorods. *J. Phys. Chem. C* **113,** 4357–4361 (2009).

84. Lee, H. Y. & Goodenough, J. B. BRIEF COMMUNICATION Supercapacitor Behavior with KCl Electrolyte. *J. Solid State Chem.* **223,** 220–223 (1999).

85. Chang, J. K., Lee, M. T. & Tsai, W. T. In situ Mn K-edge X-ray absorption spectroscopic studies of anodically deposited manganese oxide with relevance to supercapacitor applications. *J. Power Sources* **166,** 590–594 (2007).

86. Toupin, M., Brousse, T., Blanger, D. & Be, D. Charge Storage Mechanism of MnO Electrode Used in Aqueous Electrochemical Capacitor Charge Storage Mechanism of MnO 2 Electrode Used in Aqueous Electrochemical Capacitor. *Chem. Mater.* 3184–3190 (2004). doi:10.1021/cm049649j

87. Hu, C. C. & Tsou, T. W. Capacitive and textural characteristics of hydrous manganese oxide

prepared by anodic deposition. *Electrochim. Acta* **47,** 3523–3532 (2002).

88. Kim, S. H., Kim, Y. Il, Park, J. H. & Ko, J. M. Cobalt-manganese oxide/carbon-nanofiber composite electrodes for supercapacitors. *Int. J. Electrochem. Sci.* **4,** 1489–1496 (2009).

89. Nakayama, M. *et al.* Doping of Cobalt into Multilayered Manganese Oxide for Improved Pseudocapacitive Properties. *J. Electrochem. Soc.* **157,** A1067–A1072 (2010).

90. Kim, B. C. *et al.* Enhanced electrochemical properties of cobalt doped manganese dioxide nanowires. *J. Alloys Compd.* **617,** 491–497 (2014).

91. Xu, Y. *et al.* Facile synthesis route of porous MnCo2O4 and CoMn2O4 nanowires and their excellent electrochemical properties in supercapacitors. *J. Mater. Chem. A* **2,** 16480–16488 (2014).

92. Mondal, A. K. *et al.* Mesoporous MnCo\n 2\n O\n 4\n with a Flake-Like Structure as Advanced Electrode Materials for Lithium-Ion Batteries and Supercapacitors. *Chem. - A Eur. J.* **21,** 1526–1532 (2015).

93. Yin, Y. & Alivisatos, a P. Colloidal nanocrystal synthesis and the organic-inorganic interface. *Nature* **437,** 664–670 (2005).

94. Alivisatos, A. P. Nanocrystals: Building blocks for modern materials design. *Endeavour* **21,** 56–60 (1997).

95. Mostafa a. El-Sayed. Small Is Different: Shape-,Size-, and Composition-Dependent Properties of Some Colloidal Semiconductor Nanocrystals. *Acc. Chem. Res* **37,** 326 (2004).

96. Ha, D. H., Islam, M. A. & Robinson, R. D. Binder-free and carbon-free nanoparticle batteries: A method for nanoparticle electrodes without polymeric binders or carbon black. *Nano Lett.* **12,** 5122–5130 (2012).

97. Otelaja, O. O., Ha, D., Zhang, H. & Robinson, R. D. Highly Conductive Cu 2 −. (2014).

98. Fayette, M., Nelson, a. & Robinson, R. D. Electrophoretic deposition improves catalytic performance of Co\n 3\n O\n 4\n nanoparticles for oxygen reduction/oxygen evolution reactions. *J. Mater. Chem. A* **3,** 4274–4283 (2015).

99. Leatherdale, C. A. *et al.* Photoconductivity in CdSe quantum dot solids. *Phys. Rev. B* **62,** 2669–2680 (2000).

100. Islam, M. A. & Herman, I. P. Electrodeposition of patterned CdSe nanocrystal films using thermally charged nanocrystals. *Appl. Phys. Lett.* **80,** 3823–3825 (2002).

101. Islam, M. A., Xia, Y., Telesca, D. A., Steigerwald, M. L. & Herman, I. P. Controlled Electrophoretic Deposition of Smooth and Robust Films of CdSe Nanocrystals. *Chem. Mater.* **16,** 49–54 (2004).

102. Kim, Y. *et al.* Co3O4 Nanoparticle Li-Ion Battery : The Origins of Irreversible Capacity Loss. *ACS Nano* 6701–6712 (2014).

103. Cueva, P., Hovden, R., Mundy, J. A., Xin, H. L. & Muller, D. A. M icroscopy M icroanalysis Data Processing for Atomic Resolution Electron Energy Loss Spectroscopy. *Microsc. Microanal.* **18,** 667–675 (2012).

104. Murray, C. B., Sun, S., Doyle, H. & Betley, T. Monodisperse 3d Transition-Metal (Co,Ni,Fe)

Nanoparticles and Their Assembly intoNanoparticle Superlattices. *MRS Bull.* **26,** 985–991 (2001).

105. Yin, Y. *et al.* Formation of hollow nanocrystals through the nanoscale Kirkendall effect. *Science* **304,** 711–714 (2004).

106. Liu, X. & Prewitt, C. T. High-temperature X-ray diffraction study of Co3O4: Transition from normal to disordered spinel. *Phys. Chem. Miner.* **17,** 168–172 (1990).

107. Hu, L. *et al.* CoMn(2)O(4) spinel hierarchical microspheres assembled with porous nanosheets as stable anodes for lithium-ion batteries. *Sci. Rep.* **2,** 986 (2012).

108. Yonekura, D. *et al.* Progress of the conversion reaction of Mn3O4 particles as a function of the depth of discharge. *Phys. Chem. Chem. Phys.* **16,** 6027–32 (2014).

109. Bélanger, D., Brousse, T. & Long, J. W. Manganese oxides: Battery materials make the leap to electrochemical capacitors. *Electrochem. Soc. Interface* **17,** 49–52 (2008).

110. Liu, J. *et al.* Co3O4 nanowire@MnO2 ultrathin nanosheet core/shell arrays: A new class of high-performance pseudocapacitive materials. *Adv. Mater.* **23,** 2076–2081 (2011).

111. Al, C. E. T. Pseudocapacitors Based on Hierarchically Porous Nanowire Composites. 4319–4327 (2012).

112. Li, L. *et al.* Spinel manganese-nickel-cobalt ternary oxide nanowire array for high-performance electrochemical capacitor applications. *ACS Appl. Mater. Interfaces* **6,** 18040–18047 (2014).

113. Yang, D. Pulsed laser deposition of cobalt-doped manganese oxide thin films for supercapacitor applications. *J. Power Sources* **198,** 416–422 (2012).

114. Bordeneuve, H. *et al.* Structural variations and cation distributions in Mn3-xCoxO4 ($0 \leq x \leq 3$) dense ceramics using neutron diffraction data. *Solid State Sci.* **12,** 379–386 (2010).

115. Wang, L. *et al.* Facile synthesis and electrochemical properties of CoMn2O4 anodes for high capacity lithium-ion batteries. *J. Mater. Chem. A* **1,** 2139 (2013).

116. Li, M. *et al.* Well-dispersed bi-component-active CoO/CoFe2O4 nanocomposites with tunable performances as anode materials for lithium-ion batteries. *Chem. Commun.* **48,** 410–412 (2012).

117. Li, J., Xiong, S., Li, X. & Qian, Y. A facile route to synthesize multiporous MnCo2O4 and CoMn2O4 spinel quasi-hollow spheres with improved lithium storage properties. *Nanoscale* **5,** 2045–54 (2013).

118. Notarianni, M., Liu, J., Mirri, F., Pasquali, M. & Motta, N. Graphene-based supercapacitor with carbon nanotube film as highly efficient current collector. *Nanotechnology* **25,** 435405 (2014).

119. Wei, Y., Chen, S., Sun, B., Zhu, J. & Wang, G. 3D Mesoporous Hybrid NiCo2O4@graphene Nanoarchitectures as Electrode Materials for Supercapacitors with Enhanced Performances. *J. Mater. Chem. A* **2,** 8103–8109 (2014).

120. Li, W. *et al.* MnO2 ultralong nanowires with better electrical conductivity and enhanced supercapacitor performances. *J. Mater. Chem.* **22,** 14864 (2012).

121. Subramanian, V., Zhu, H., Vajtai, R., Ajayan, P. M. & Wei, B. Hydrothermal synthesis and pseudocapacitance properties of MnO 2 nanostructures. *J. Phys. Chem. B* **109,** 20207–20214 (2005).

122. Burke, A. R&D considerations for the performance and application of electrochemical capacitors. *Electrochim. Acta* **53,** 1083–1091 (2007).

123. Taberna, P. L., Simon, P. & Fauvarque, J. F. Electrochemical Characteristics and Impedance Spectroscopy Studies of Carbon-Carbon Supercapacitors. *J. Electrochem. Soc.* **150,** A292 (2003).

124. Jossen, A. Fundamentals of battery dynamics. *J. Power Sources* **154,** 530–538 (2006).

125. Ardizzone, S., Fregonara, G. & Trasatti, S. 'Inner' and 'outer' active surface of RuO2 electrodes. *Electrochim. Acta* **35,** 263–267 (1990).

126. Pétrissans, X. *et al.* Solution synthesis of nanometric layered cobalt oxides for electrochemical applications. *Electrochim. Acta* **66,** 306–312 (2012).

127. Wang, J., Polleux, J., Lim, J. & Dunn, B. Pseudocapacitive Contributions to Electrochemical Energy Storage in TiO2 (Anatase) Nanoparticles. *J. Phys. Chem. C* **111,** 14925–14931 (2007).

128. Hou, X. *et al.* Hierarchical MnCo2O4 nanosheet arrays/carbon cloths as integrated anodes for lithium-ion batteries with improved performance. *Nanoscale* **6,** 8858–64 (2014).

129. Stoller, M. D. & Ruoff, R. S. Best practice methods for determining an electrode material's performance for ultracapacitors. *Energy Environ. Sci.* **3,** 1294 (2010).

130. Guo, W., E, Y., Gao, L., Fan, L. & Yang, S. A catalytic nanostructured cobalt oxide electrode enables positive potential operation for the cathodic electrogenerated chemiluminescence of Ru(bpy)3(2+) with dramatically enhanced intensity. *Chem. Commun. (Camb).* **46,** 1290–2 (2010).

131. Xia, H. *et al.* Hierarchically structured Co3O4@Pt@MnO2 nanowire arrays for high-performance supercapacitors. *Sci. Rep.* **3,** 2978 (2013).

132. Menezes, P. W. *et al.* High-Performance Oxygen Redox Catalysis with Multifunctional Cobalt Oxide Nanochains: Morphology-Dependent Activity. *ACS Catal.* **5,** 2017–2027 (2015).

133. Li, L., Li, Y., Gao, S. & Koshizaki, N. Ordered Co3O4 hierarchical nanorod arrays: tunable superhydrophilicity without UV irradiation and transition to superhydrophobicity. *J. Mater. Chem.* **19,** 8366 (2009).

134. Wei, W., Chen, W. & Ivey, D. G. Rock Salt - Spinel Structural Transformation in Anodically Electrodeposited Mn - Co - O Nanocrystals. *Chem. Mater.* **20,** 1941–1947 (2008).

135. Chuang, T. J., Brundle, C. R. & Rice, D. W. Interpretation of the x-ray photoemission spectra of cobalt oxides and cobalt oxide surfaces. *Surf. Sci.* **59,** 413–429 (1976).

136. Cheng, K., Yang, F., Wang, G., Yin, J. & Cao, D. Facile synthesis of porous (Co, Mn)3O4 nanowires free-standing on a Ni foam and their catalytic performance for H2O2 electroreduction. *J. Mater. Chem. A* **1,** 1669 (2013).

137. Liu, C., Yu, Z., Neff, D., Zhamu, A. & Jang, B. Z. Graphene-based supercapacitor with an ultrahigh energy density. *Nano Lett.* **10,** 4863–4868 (2010).

138. Wang, G., Zhang, L. & Zhang, J. A review of electrode materials for electrochemical supercapacitors. *Chem. Soc. Rev.* **41,** 797 (2012).

139. Li, J., Murphy, E., Winnick, J. & Kohl, P. a. Studies on the cycle life of commercial lithium ion batteries during rapid charge-discharge cycling. *J. Power Sources* **102,** 294–301 (2001).

140. Ning, G., Haran, B. & Popov, B. N. Capacity fade study of lithium-ion batteries cycled at high discharge rates. *J. Power Sources* **117,** 160–169 (2003).

141. Andre, D. *et al.* Characterization of high-power lithium-ion batteries by electrochemical impedance spectroscopy. I. Experimental investigation. *J. Power Sources* **196,** 5334–5341 (2011).

142. Levi, M. D. & Aurbach, D. Impedance of a single intercalation particle and of non-homogeneous, multilayered porous composite electrodes for Li-ion batteries. *J. Phys. Chem. B* **108,** 11693–11703 (2004).

143. Hughes, M., Chen, G. Z., Shaffer, M. S. P., Fray, D. J. & Windle, a H. Electrochemical Capacitance of Carbon Nanotube - Polypyrrole Composite Films. 10 (2000).